Analysis of free surface flows in formation, coalescence and impact of drops on liquid surfaces

A thesis submitted
in partial fulfillment of the requirements
for the degree of

Doctor of Philosophy

by

Hiranya Deka

Department of Mechanical Engineering
Indian Institute of Technology Guwahati
Guwahati 781039
September 2018

CERTIFICATE

It is certified that the work contained in the thesis entitled **"Analysis of free surface flows in formation, coalescence and impact of drops on liquid surfaces"** by Hiranya Deka (Roll No. 146103027), has been carried out under our supervision and that this work has not been submitted elsewhere for a degree.

(Gautam Biswas)
Professor
Department of Mechanical Engineering
Indian Institute of Technology Guwahati

(Amaresh Dalal)
Associate Professor
Department of Mechanical Engineering
Indian Institute of Technology Guwahati

September 2018

Acknowledgements

I would like to express my sincere gratitude to the people who have directly or indirectly contributed to this doctoral thesis and have supported me during this amazing journey. First and foremost, I would like to express my sincere gratitude to my thesis supervisors, Prof. Gautam Biswas and Dr. Amaresh Dalal, for the continuous support provided by them in my research work. I am deeply thankful to them for the valuable suggestions and guidance during this period. Prof. Gautam Biswas has been a tremendous mentor for me. He has always made himself available to clarify my doubts despite his busy schedule being the Director of the institute. The motivation that I have got from him and the immense knowledge that he shared with me have allowed me to grow as a research scientist. I consider myself fortunate to have carried out my thesis work under his guidance and learn from his research expertise. Dr. Amaresh Dalal is a person with an amicable and positive disposition. This feat has become possible only because of the continuous support provided by him. His advice on both research as well as on my career has been priceless. I could not have imagined having better mentors for my Ph.D. study.

Besides my thesis supervisors, I would like to thank Prof. Pinakeswar Mahanta, Dr. Bhaskar Kumar, Dr. Tapas Kumar Mandal and Dr. Ganesh Natarajan for their insightful comments as doctoral committee members. Their suggestions and encouragement helped me to widen my research from various perspectives.

I would like to express my sincere gratitude to Dr. Bahni Ray of IIT Delhi for many insightful discussions and suggestions at various points of my research programme. I express my gratitude to Prof. An-Bang Wang and Mr. Pei-Hsun Tsai of National Taiwan University, Taiwan for sharing their experimental results during our collaborative works, through which my research work has been immensely benefited. I am also grateful to Prof. Suman Chakraborty of IIT Kharagpur for many useful suggestions. I am thankful to Prof. Kirti Chandra Sahu of IIT Hyderabad for many fruitful discussions. I am also thankful to Prof. Vijay K. Dhir of University of California, Los Angeles, USA for sharing his knowledge during his stay at IIT Guwahati.

I am grateful to the Department of Mechanical Engineering, IIT Guwahati for providing me the required facilities and an excellent working environment. I am

thankful to the faculty members who taught various courses during my coursework at IIT Guwahati. I express my sincere gratitude to Prof. Gautam Biswas, Dr. Arnab Kumar De, Dr. Vinayak Kulkarni, Dr. Hrishikesh Gadgil, Dr. Amaresh Dalal and Dr. Dipankar Narayan Basu for sharing their knowledge. I am thankful to Mr. Vinod Pandey for the assistance provided by him during the whole phase of my Ph.D. work. I am also very much thankful to the Computer & Communication Centre of IIT Guwahati for providing the High-Performance Computing facility through which my research work has been immensely benefited. In addition to research, I appreciate the sport and physical exercise facilities provided by IIT Guwahati to remain fit and healthy. I am thankful to the mess workers for providing me food and the cleaners for maintaining a hygienic environment.

I extend my deep regards to Mrs. Amarabati Biswas and Mrs. Soumita Dalal for their love, care and for the delicious food that they offered on various occasions during my stay at IIT Guwahati. I enjoyed working with Vinod Pandey, Binita Nath, Manash Pratim Borthakur, Srinivas R. Gorthi, Snehasish Panigrahy, Dhrubajyoti Das and Vishal Sethi under the same supervisor. I acknowledge them for maintaining a healthy work environment and cherish the joyful moments that we spent together. I am also thankful to Subrat Kotoky, Saurabh Bhardwaj, Dr. Preetirekha Borgohain, Dr. Jai Manik and Mukul Parmananda for their assistance on various occasions. I acknowledge Deepak Kumar, Wasim Akram and Bhaskar Bhattacharyya for many fruitful discussions during my coursework days and the laughter that we shared together. I am thankful to all the colleagues from Mechanical Engineering Department for keeping me blessed with best wishes.

I am fortunate to have friends who always stood beside me. I thank them all for their continuous encouragement. I acknowledge Ashim Kumar, Nitul Kumar Das, and Gauranga Gogoi for their immense cooperation and for all the fun we have had in the last four years. I extend my gratitude to Dr. Subasit Borah and Dr. Madhuriya Pratim Das for their constructive advice.

Words cannot express the feelings that I have for my parents for the sacrifice that they have made for me. They have been a constant source of inspiration for me. Special thanks to my elder sister Nita Deka for her love, care and unconditional support in pursuing my Ph.D. I acknowledge my brother-in-law Mr. Diganta Choudhury for his encouragement and my five year old, dearest nephew Darsheel Choudhury whose innocence refreshed me during my difficult times. I am also grateful to my relatives for their love and support. At last, I would like to thank myself for carrying out my research work with patience and dedication throughout the whole period.

Hiranya Deka

Abstract

Flows with free moving boundaries or interfaces represent a very important class of problems in fluid dynamics. The fluid across the interface is held together by surface tension force that gives rise to pressure jump across the interface whenever it is curved. The dynamics of free surface flows have been of great interest to researchers for centuries and continue to be an important paradigm because of its applications in a variety of industrial processes and due to the richness of the underlying physics. The present thesis is focused on the study of free surface flows in context with formation and coalescence dynamics of drops. State-of-the-art computational tools have been deployed to develop a new understanding of the fundamental aspects of free surface flows and dynamic interactions between liquid surfaces. Investigations are supported by experiments whenever possible. The numerical simulations have been performed by solving the complete Navier-Stokes equations. The interfaces have been captured using the coupled level set and volume-of-fluid (CLSVOF) method.

A pendant drop remains attached to the orifice as long as the surface tension force can balance the gravitational force acting on it. Because of continuous flow through the orifice, the drop volume increases and the drop finally separates out from the fluid attached to the orifice when the surface tension force can no longer balance the gravitational force pulling the drop down. The shape of the drop at the incipience of pinch-off depends on the internal stress distribution within the drop. A large velocity gradient inside the drop culminates in a strong shear force within the drop resulting in a non-spherical drop during pinch-off. Increased viscosity of the drop fluid damps out the velocity gradient within the drop causing the drop to approach a spherical shape. The drop undergoes prolate-oblate-prolate oscillation while falling through the surrounding medium. The oscillatory motion is generated due to the local capillary pressure that develops across the drop surface because of the deformed shape of the drop after pinch-off. The downward pull generated near the pinching region deforms the drop after pinch-off making it non-spherical and initiates the oscillatory motion of the drop. The oscillation of drops reduces substantially at higher Ohnesorge number.

When a drop impacts a liquid pool, a range of fluid dynamical phenomena can be observed including drop coalescence, drop splashing and bubble entrapment. The

bubble entrapment owing to the impact of a liquid drop on a liquid pool may take place mainly in two ways: firstly, owing to the closure of the mouth of the crater formed on the liquid pool caused by the impacting of the drop, and secondly, due to the rupture of the air film trapped near the bottom surface of the drop. Earlier investigations identified different regimes of bubble entrapment on impact velocity (V)−drop diameter (D) map and on the Froude number (Fr)−Weber number (We) map which suggests that large bubble entrapment occurs over a small region. However, present numerical and experimental investigations demonstrate large bubble entrapment outside the small regime of the traditional map. Present investigation discerns the large bubble entrapment regime on the $V - D$ map and on the $Fr - We$ map revealing that large bubble entrapment may take place over a wide range depending on the shape of the drop during impact. The large bubble may be accompanied by the entrapment of a small bubble and is observed only for prolate shaped drops. Entrapment of a large bubble is a vortex-driven phenomenon. When the vortex penetration is less the vortex ring interacts with the interface and self-destructs early. Prolate shaped drops bring about deeper penetration of the vortex ring into the pool and this vortex later pulls and curls-up the interface to form the roll jet. The roll jet merges at the central axis to entrap a large bubble inside the liquid pool. The emergence of ejecta sheet which leads to lamella prevents the penetration of the vortex ring, and thus prevents the large bubble entrapment. The entrapment of large bubble is always accompanied by an inward jet and an upward jet. The inward jet penetrates through the bubble and deforms the bubble shape.

The study of micrometer sized drops has received more attention recently because of its increasing application in microscale fabrication processes and microscale devices. During the impact of microdrops the capillary effects are much more significant than those due to the impact of millimeter sized drops, and even dominating over gravity. The impact of a train of high-speed microdrops creates a tongue shaped deep cavity inside the liquid pool, whose depth can be more than hundred times the microdrop diameter. Capillary wave emerges from the crater base owing to the impact of drops. As multiple drops impact the crater, multiple waves emerge from the crater base and propagate through the crater wall. The capillary waves converge near the cavity mouth and expedite the necking. The maximum attainable penetration velocity of the cavity is equal to half of the impact velocity of the drops and is achieved when the drops are attached to each other, which forms a continuous liquid jet. The cavity mouth motion can be classified into two stages, one is the expansion stage and the other is collapse stage. The temporal variation of neck radius shows power-law behavior in both expansion and collapse stage. In the pinching region, the cavity collapse phenomenon is self-similar in nature. There exists a critical train length below which cavity pinch-off is inhibited. In the current analysis, it has been observed that pinch-off takes place when the penetration depth of the cavity becomes approximately three times the average diameter of the cavity.

Contrary to intuitive expectations, the coalescence of two drops of unequal sizes does not necessarily result in their complete convergence into a single larger mass

in an effort to minimize the surface energy. Rather, the process often pinches off a smaller daughter droplet, also known as satellite droplet. Capillary waves are produced by the expanding neck, because of the high curvature generated near the contact line. The capillary waves propagate through the periphery of the drops and converge at the tip. The upward capillary pull exerted by the convergence of capillary waves delays the vertical collapse of the mother drop, such that the horizontal collapse reaches completion resulting in pinch-off of daughter drops. The capillary waves propagating along the interface of the father drop converge at its bottom and exert a downward pull. The deformation of the father drop because of this downward pull inhibits the pinch-off process if the capillary waves reach the bottom of the father drop before the pinch-off of the daughter drop. A higher capillary pressure inside the drops increases radial expansion of the neck and delays the retraction of the neck. Because of the larger opening of the neck, the drainage increases and beyond a particular limit, the vertical rate of collapse dominates over the horizontal rate of collapse and inhibits the satellite formation. Local curvature of the neck plays a crucial role in the pinch-off dynamics. A sharper azimuthal curvature of the neck increases the local capillary pressure which tends to expand the neck and restricts the pinch-off. The critical size ratio of the two drops above which a satellite is pinched off during the coalescence may be as low as 1.65 and it grows with increasing relative strength of the viscous force. The process of coalescence of two unequal sized drops may produce much smaller satellite droplets, on account of the successive preferential occurrence of coalescence steps, with or without any intermediate detachment.

Contents

List of Figures

List of Tables

Chapter 1

Introduction

The multiphase flows are encountered in a wide variety of flow problems involving engineering applications and natural phenomena. Due to its universality in applications, a thorough understanding of the multiphase flow is of utmost importance. A multiphase flow may be defined as one in which more than one phase (i.e., gas, solid and liquid) is present. One of the most important classes of multiphase flows is the two-phase flow where the number of phases present is two. Two-phase flows may be gas-liquid flows, gas-solid flows, liquid-liquid flows and liquid-solid flows. Moreover, the flow may undergo a process of phase change or it may be without any change of phase.

1.1 Free surface flows

Free surface flows refer to the special class of multiphase flows where the two-phases are separated by a distinct interface. Such interfaces behave like a stretched membrane. The origin of such tension at the interface is because of the intermolecular attractive forces. The magnitude of this tensile force per unit length of a line on the interface is called surface tension σ, which has the unit N/m. The value of surface tension depends on the properties of the two fluids which are in contact and also on temperature. The two immiscible fluids across the interface are held together by the surface tension force.

Owing to the existence of surface tension, there is high energy density at the surface of the liquid. This is because the molecules on the surface are packed by

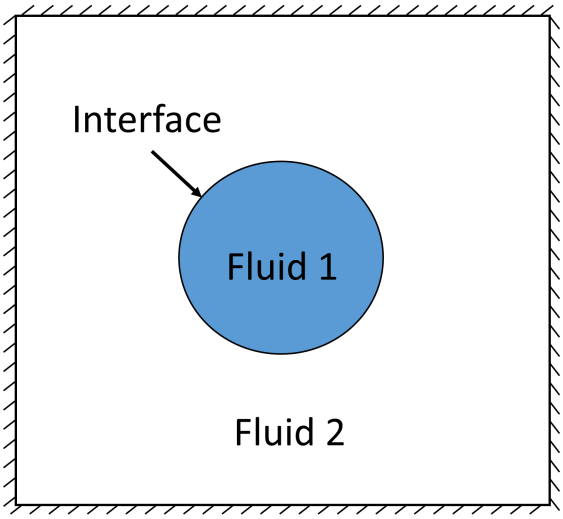

Figure 1.1: Representative diagram showing the interface and the two fluids.

the unbalanced intermolecular forces higher than the rest of the molecules. An important consequence of surface tension is that it gives rise to a pressure jump across the interface whenever it is curved. For a spherical interface having fluid 1 on one side and fluid 2 on the other side (Fig. 1.1) and having the radius of curvature R, the pressure jump across the interface can be found as,

$$p_1 - p_2 = \frac{2\sigma}{R}, \tag{1.1}$$

where p_1 and p_2 are the pressures on fluid 1 and fluid 2 respectively. The pressure on the concave side is always higher. The curvature of a general surface can be specified by the radii of curvature along two orthogonal directions, say, R_a and R_b. Under such a situation the pressure jump across the interface is given by,

$$p_1 - p_2 = \sigma \left(\frac{1}{R_a} + \frac{1}{R_b} \right). \tag{1.2}$$

For a spherical interface $R_a = R_b$, which results in Eq. 1.1.

The study of drops can be placed under the domain of two-phase flows, which has been studied for centuries because of the richness of the underlying physics. Furthermore, because of the increasing applications in a variety of industrial processes, it has received more attention from the researchers. Numerous investigations have been performed on the formation of drops to understand the underlying physics and

to probe deep into the pinch-off dynamics. Investigations have also been performed to understand the instability dynamics during the pinch-off process.

The coalescence/impact of liquid drops on a liquid pool is a very interesting aspect of drop dynamics. It has attracted many researchers to analyze the fascinating aspects of the coalescence dynamics. Worthington [1] first reported different paradigms of drop impact on a liquid pool. He captured the salient features of drop impact using high-speed photography. Later, numerous investigations have been performed to understand the coalescence behavior under different conditions. The advancements of high-speed photography have opened up the kaleidoscopic phenomena to renewed scrutiny.

The development of numerical techniques opened new horizons in understanding the mechanism of drop coalescence/impact. Many intrinsic features of the coalescence dynamics have been unveiled by accurate numerical modeling of the flow dynamics. The first attempt to numerically reproduce the phenomena was made by Harlow and Shannon [2,3] by solving the complete Navier-Stokes equations. Subsequently, many novel features associated with drop impact have been identified and explained by numerous researchers.

There are many features pertaining to formation and coalescence of drops that are still unexplored and require to be comprehensively addressed. Present investigations have revealed many new features leading to formation and coalescence dynamics of drops. Many new and intrinsic features describing the complex dynamics of drop formation and coalescence of falling drops have been analyzed in the investigations of interest.

1.2 Drop formation

The formation of liquid drop is of practical importance in many natural as well as industrial processes. It bears far reaching implications in a variety of engineering processes such as measurement of surface tension by the drop weight method, fuel injection in the combustion chamber of gas turbines, spray in milk drying, separation and extraction processes, to name a few.

Although it is straightforward that drops generically result from the motion of free surfaces, it is not easy to predict the distribution of their sizes or to observe the intricate dynamics involved with it. Because of the complex nature of the phenom-

ena, researchers are studying this subject even after more than 100 years of scientific research. In fact, it has gained significant momentum in the recent decades. The reason for the renewed interest lies in the tremendous technological importance attributed to drop formation in mixing, spraying, and chemical processing. A common way of drop formation is to enable a continuous flow of a liquid in a quiescent immiscible ambient fluid through a nozzle or an orifice from which it emanates into the ambient fluid and breaks into drops. At low flow rates, the liquid emanates from the orifice as discrete drops because of its own weight. At high flow rates, the liquid is ejected from the nozzle as a jet. Subsequently, the jet breaks up into ligaments and small drops owing to well known Rayleigh-Plateau instability. The above two modes of drop formation are commonly referred as *dripping* mode and *jetting* mode respectively. The transition from dripping mode to jetting mode is another enthralling topic that has attracted many researchers to perform experimental, numerical and analytical investigations. The drop, after detachment from the orifice, undergoes oscillation in shape because of the unbalanced capillary pressure within the drop. The shape of the drop is a crucial parameter in the coalescence dynamics of drops such as bubble entrapment. In the present thesis, a comprehensive study has been performed on the shape of a drop during pinch-off as well as on the oscillation of the drops after pinch-off.

1.3 Paradigms of drop coalescence and impact

The coalescence of drops has implications for the dynamics of a variety of systems. One of the most important applications of drop coalescence is the separation of the water phase from the oil phase in an emulsion. Furthermore, it has wide range of applications in many other fields such as agriculture (pesticide distribution, soil erosion), oceanography (gas absorption, noise generation), meteorology (cloud generation and rain formation) etc.

Let us consider an interface of two fluids, viz. fluid 1 and fluid 2, where the lighter fluid 2 is resting above the heavier fluid 1. Let a droplet of liquid 1 falls through a lighter fluid 2 and hits the fluid 1-2 interface. After impacting the interface, the droplet of liquid 1 may completely mix with the pool liquid, which is commonly known as complete coalescence. Complete coalescence is generally connected with the generation of vortex rings that enhance strong mixing. Formation of thick and

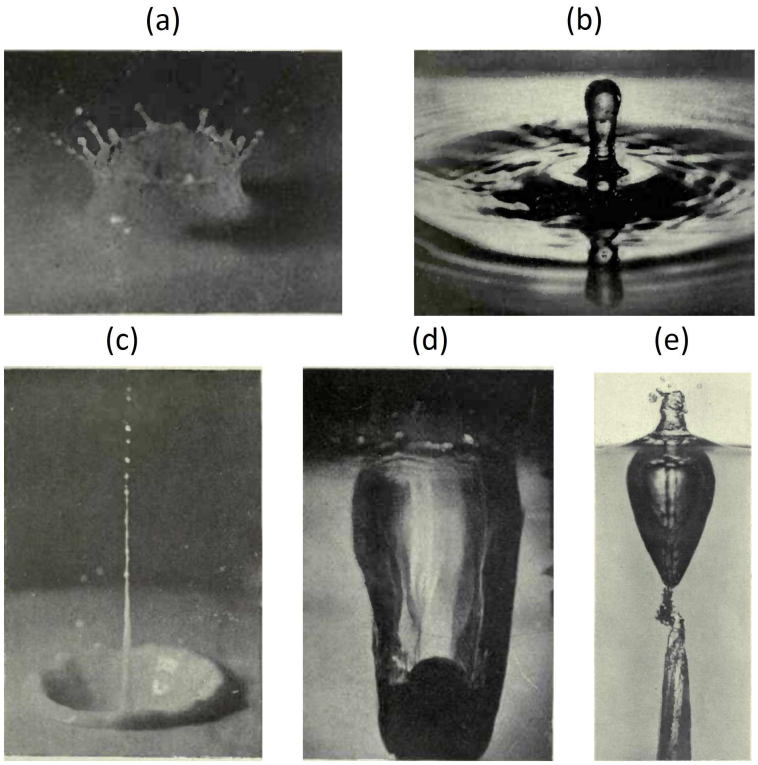

Figure 1.2: Different photographs captured by A. M. Worthington and reported in his book *A Study of Splashes* [1], showing different paradigms of drop impact and solid object impact on a liquid pool. The different paradigms shown in the photographs are: (a) splashing with crown formation, (b) thick jet formation, (c) thin jet formation, (d) deep crater formed during solid object impact and (f) bubble entrapment by cavity pinch-off during solid object impact.

thin jets are also seen depending on the impact condition. On the other hand, the drop may not completely coalesce with the pool, rather producing secondary droplets of smaller size by draining out some amount of fluid to the pool. This phenomenon is called partial coalescence and the secondary droplet is commonly known as the satellite or daughter droplet. Depending on the physical condition of coalescence, a cascade of daughter droplets may be observed where a daughter drop produces another daughter after coalescing with the pool. The satellite formation may also take place during the coalescence of two drops of unequal size. The capillary pressure distribution within the drop is an important parameter to prompt the fate of the final outcome in this situation.

Worthington [1] reported different paradigms of drop impact on a liquid pool, captured using high-speed photography. Depending on the drop size, fluid properties

and flow parameters different regimes were observed such as jet formation, secondary drop formation, crown formation etc. Some of the photographs captured by Worthington are shown in Fig. 1.2, including the impact of a solid object on a deep liquid pool. Ray et al. [4] interpreted these phenomena as the consequences of different crater dynamics. Based on the shape of the crater, expansion and contraction time, the final outcome can be coalescence, jet formation with bubble entrapment or jet formation without bubble entrapment and splashing. Splashing takes place with crown formation and breakup. Moreover, many interesting phenomena such as the formation of vortex rings, large bubble entrapment etc. are related to the intricate dynamics of drop coalescence.

Bubble entrapment during drop impact on a pool is of great importance in natural as well as industrial processes such as underwater acoustics, aquatic life, environmental and chemical processes. The mechanism of bubble formation is governed by the dynamics of the crater formed during drop impact. The crater morphology is mainly governed by the impact velocity and the diameter of the impacting drops. Moreover, the shape of the drop during impact has a crucial role in the resulting crater morphology. Based on the crater morphology, a small bubble may form at the base of the crater during crater collapse or a bubble may form owing to the merger of the liquid tongue which is generated because of the curl-up of the crater interface. The latter yields a bubble of large volume and is commonly known as large bubble entrapment. The bubbles are also formed by the break-up of the sub-micron gas film trapped during the impact of drops. These are very small bubbles of micron size. The study of micro-bubble morphology is important as the microbubbles can greatly enhance the gas transfer through the interface into the pool.

Unlike millimeter sized droplets which have been studied extensively, the focus on the impact of micrometer sized droplets has caught the attention of researchers very recently. This is because of the extensive applications of microdrop impacts in printing, lithography, painting and coating applications. Basaran et al. [5] studied the complex mechanism of inkjet printing through the fundamental viewpoint of fluid mechanics. The fluid mechanical approach has continued to grow in importance as simulations have become equally important as compared to experiments in probing operating principles, improving device performance, and, developing insights into the complex dynamics.

1.4 Numerical approaches for two-phase flows

Experimental investigations of some realistic applications are very difficult, as many of the experimental techniques cannot be extended to two-phase flows because of its inherent complexity. Experimental investigations have limitations to capture the detailed nuances of the flow dynamics. This motivates the researchers to develop accurate and cost-effective numerical methods for modeling the two-phase flows. Numerical methods for computing fluid flows have become very popular in recent decades because of their capability to provide a deep insight into the physical mechanisms. The accurate modeling of fluid flow with material interfaces requires numerical techniques which can efficiently describe the interface topology. However, considering the challenges involved in two-phase flows, constructing such methods is a difficult task. These challenges include modeling discontinuities in physical properties across the interface, handling complex topology and separation of scales, accurate calculation of the surface tension force etc.

There are various numerical methods to model the dynamics of two-phase flows. One of the most popular models is *one-fluid* model, where the Navier-Stokes equations are solved by assuming it as a single fluid. The one-fluid model can be broadly classified into two types, namely, interface tracking method and interface capturing method. An interface tracking method requires meshes that track the interface and are updated as the flow evolves. On the other hand, in interface capturing method the interface is moved through a fixed grid-mesh marked by steep gradient of a scalar function. Here, the computations are based on fixed spatial domain. The most popular interface capturing methods are *Volume-of-Fluid (VOF)* method, *Level Set method (LS)* and *Phase Field method*.

In the VOF method, the volume fraction F is defined for each computational cell based on the initial interface geometry [6, 7]. The volume fraction F is zero or unity in a pure fluid cell. In each two-phase cell its value lies between zero and one $(0 < F < 1)$. The volume fraction is then advected and the interface is reconstructed based on the updated values of the volume fractions. Thus, the *advection* and interface *reconstruction* are the two main features of this method. There exists huge computational challenge in handling problems of strong topological deformations of the interface such as merging and fragmentation. Precise determination of some geometrical quantities such as curvature and tortuosity becomes a challenge in such a situation. A large difference in density or viscosity of the two phases further increases

the difficulty because of the large jump in these properties across the interface. An inconsistent calculation of the surface tension force can result in the well-known phenomenon of generation of "parasitic currents" [8]. A separate surface tension model takes care of the surface tension effects. An important property of the VOF method is the conservation of volume of each fluid which makes the method more applicable to practical problems. The discontinuity of rheological properties at the interface is taken care of by some suitable smoothening technique which facilitates the calculation of interface normal and curvature.

A brief survey of the historical development of the volume-of-fluid formulation by considering the methods for reconstructing the interface are described herein. Two early approaches were the SLIC algorithm (simple line interface calculation) of Noh and Woodward [9] and the volume-of-fluid algorithm of Hirt and Nichols [6], where the interface was represented by a piecewise continuous line in each two-fluid cell, either vertically or horizontally. A significant improvement of the interface representation was accomplished by Youngs [10] by introducing a piecewise-linear method for interface representation called PLIC (piecewise linear interface calculation). Youngs' method is very robust and efficient, but only of first-order accuracy. Later on, many techniques such as LVIRA [11], PROST [12] have been developed in order to get higher order accuracy.

In the LS method, the interface is defined by a signed distance of a level-set function ϕ which is positive on one side and negative on the other side of the interface [13]. The interface itself is represented by zero value of the level set function, i.e., $\phi = 0$. Based on the calculated velocity field, the front evolves as a solution of a transport equation for ϕ. As the level set function ϕ is advected with the flow velocity, it does not remain a distance function at later times. This leads to interface smearing and difficulties in preserving the mass conservation are encountered. Thus, reinitialization of the level set function is required after each time step. An important attribute of the level set method is that the interface is inherently smooth. Because of this particular quality, it can handle very complex topology.

A coupled level set and volume-of-fluid (CLSVOF) method [14] can be incorporated to blend the properties of both the above methods. In CLSVOF method, the level-set function is deployed to calculate the interface normal and curvature whereas advection algorithm of VOF is used for volume flux transfer. The present investigations have been performed using an in-house code based on the CLSVOF methodology, which has been tested rigorously [15]. The advantage of CLSVOF

method is that VOF advection algorithm ensures the compliance of mass conservation and level set function ensures accurate calculation of the geometric properties of the interface.

The surface tension forces at the interface have to be accurately incorporated in the solution algorithm. The coalescence of liquid drops poses a difficult challenge, because the curvature becomes very sharp near the merging region. This may create infinitely large capillary forces. Proper optimization of the interface thickness is essential for capturing the topological change of the interface in such a situation. Accurate curvature estimation and well-balanced surface tension force discretization are required for reducing the numerical artifacts, such as spurious currents. The present method incorporates the continuum surface force model [16] where the surface tension is introduced as the volume force. The determination of surface tension force requires the calculation of curvature and normal of the interface at each two-phase cell. This demands the interface smoothening in a region of finite thickness around the interfacial line. The advantage of CLSVOF method is that it is inherently smooth and allows easy implementation of the discretization schemes. In the current methodology, a smoothed Heaviside function [17] is defined to interpolate the physical properties around the interface.

1.5 Non-dimensional parameters

The physical parameters that govern the formation, coalescence and impact dynamics of drops are surface tension, inertia, gravity, and viscosity. In order to compare the relative effect of these parameters, some non-dimensional parameters are defined based on appropriate length and time scale. Let us assume L is the length scale, t is the time scale, V is the velocity scale, ρ is the reference density, μ is the reference viscosity and σ is the surface tension coefficient. Based on these physical parameters, the non-dimensional numbers relevant to the present study are presented in Table 1.1.

1.6 Objectives

Many investigations have been performed to elucidate the intrinsic dynamics of drop formation and its coalescence. Although various salient features of this complex

Table 1.1: Non-dimensional parameters relevant to study of drop dynamics.

Non-dimensional parameter	Definition
Weber number (We)	$\rho V^2 L/\sigma$
Ohnesorge number(Oh)	$\mu/\sqrt{\rho\sigma L}$
Bond number (Bo)	$\rho g L^2/\sigma$
Reynolds number (Re)	$\rho V L/\mu$
Froude number (Fr)	V^2/gL
Capillary number (Ca)	$\mu V/\sigma$

topological dynamics have been discovered and reported in the literature, there are many unanswered questions due to the inherent complexity of the problem. There are several areas in the field of interest that need rigorous investigations to get the complete insight of the underlying physics. This is the primary motivation behind conducting this study. The investigations performed in the current Ph.D. thesis are based on the following objectives.

1. To study the mechanism of non-spherical drop generation and its oscillations while falling through the surrounding medium.

2. To investigate the mechanism of large bubble formation and redefine the regime of large bubble entrapment on drop diameter (D)−impact velocity (V) plane.

3. To study the impact of a high-speed microdrop train on a deep liquid pool and analyze the cavity dynamics.

4. To study the coalescence dynamics of unequal sized drops.

1.7 Thesis layout

The present thesis focuses on some important paradigms of free surface flows in the context with drop dynamics. Numerical investigations have been performed by applying the CLSVOF method. In this endeavor, a clear understanding of the free surface flow phenomenon and numerical techniques suitable to simulate such flows is essential. The present chapter provides a glimpse of these important features. Chapter 2 describes the numerical methodology used in the present investigations. Chapter 3 covers the study on drop formation through an orifice. The analyses on the shape of the drop at the incipience of pinch-off and its oscillation while falling through a surrounding medium have been reported. Chapter 4 covers the studies on

the mechanism of large bubble formation during the impact of a drop on a deep liquid pool. The regime of large bubble entrapment on drop diameter (D)−impact velocity (V) plane have been identified. The investigations on the dynamics of the tongue shaped cavity formed during the impact of a train of high-speed microdrops on a deep liquid pool have been reported in Chapter 5. Chapter 6 describes the coalescence dynamics of two unequal sized drops with an emphasis on the mechanism, critical parameters and transition to complete coalescence. Finally, in Chapter 7 the thesis concludes with the summary of the main findings and highlights the scope for future research.

Chapter 2

Numerical modeling

2.1 Introduction

Numerical investigations of free surface flows involving interface motion have become a popular choice owing to the deep insight it can provide into the complex physical mechanisms that characterize such flows. Various numerical methods have been developed to simulate the interface motion for such complex flows. The numerical methods can be broadly divided into two groups, viz., Eulerian and Lagrangian methods. In Eulerian approach, the interface is embedded in computational cells of the fixed spatial domain. The interface movement is captured at every time step using a predefined scalar function. Whereas in Lagrangian approach, the interface is treated as a sharp boundary which requires meshes that track the interface and are updated as the flow evolves. The grid-meshes move with the interface or body fitted grid-meshes are generated every time step. Another category is the blend of Eulerian and Lagrangian approach where a front marks the interface but the solution is obtained for a fixed grid which is modified near the front to make the grid line follow the interface.

As mentioned earlier in Chapter 1, present computations are performed using a CLSVOF methodology based in-house code. The two-fluid system considered here consists of two incompressible homogeneous fluids. The interface is considered as a free boundary where the flow variables exhibit discontinuities. Various numerical methods have been developed to simulate the transient nature of free surface flows. The CLSVOF method blends the advantages of both volume-of-fluid method and

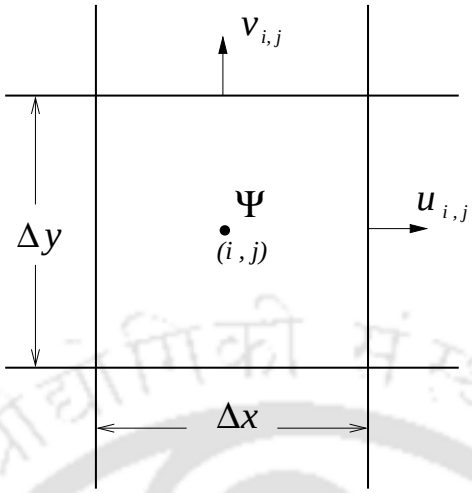

Figure 2.1: Representative diagram showing the staggered grid arrangement.

level set method and is very effective in capturing the complex topology. The numerical methodology used in the present investigations has been described in detail in the forthcoming sections. Present investigations are performed under the isothermal condition.

2.2 Governing equations

For incompressible Newtonian fluids, the mass and momentum conservation equations are given as

$$\nabla \cdot \mathbf{V} = 0, \tag{2.1}$$

$$\rho \left[\frac{\partial \mathbf{V}}{\partial t} + \nabla \cdot (\mathbf{V}\mathbf{V}) \right] = -\nabla p + \rho \mathbf{g} + \nabla \cdot (2\mu \mathbf{D}_v) + \mathbf{f}_{sv}, \tag{2.2}$$

where $\mathbf{V} = (u, v)$ is the velocity vector field having components u and v in the two orthogonal directions, say $x-$direction and $y-$direction; t is time; p is the pressure field; $\mathbf{g}$ is the gravitational acceleration; $\mathbf{D}_v = \frac{1}{2}\left\{(\nabla \mathbf{V}) + (\nabla \mathbf{V})^T\right\}$ is the rate of deformation tensor; ρ and μ are the density and the viscosity, and, $\mathbf{f}_{sv}$ is the surface tension force. The surface tension term $\mathbf{f}_{sv}$ in momentum conservation equation (Eq. 2.2) is defined by the continuum surface force model of Brackbill et al. [16]. The

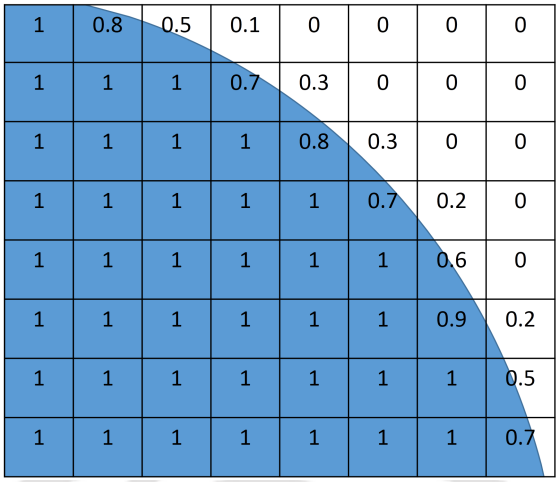

Figure 2.2: Representative diagram showing the distribution of volume fraction around the interface.

surface tension model is discussed in detail in a later section. The marker and cell algorithm (MAC) is employed to solve the single set of governing equations on a staggered grid arrangement of Harlow and Welch [18]. A uniform grid is used where the grid size in both the directions is considered to be the same, i.e., $\Delta x = \Delta y$. The vector quantities such as the velocities are defined at the center of the cell faces to which they are normal and the scalar variables are defined at the cell centers as shown in Fig. 2.1. In Fig. 2.1, Ψ represents the scalar variables such as the density, pressure, temperature, volume fraction and level set function.

2.3 Volume-of-fluid advection algorithm

The two fluids, say fluid 1 and fluid 2, are separated by the interface. The indicator function that identifies the two fluids is defined as,

$$F_{i,j} = \frac{\rho - \rho_2}{\rho_1 - \rho_2}. \tag{2.3}$$

Here, ρ_1 and ρ_2 are the densities of the two fluids and ρ is the density in a given (i, j) cell. In VOF method the indicator function F used to mark the two fluids is called void fraction or volume fraction. A particular fluid is identified by volume

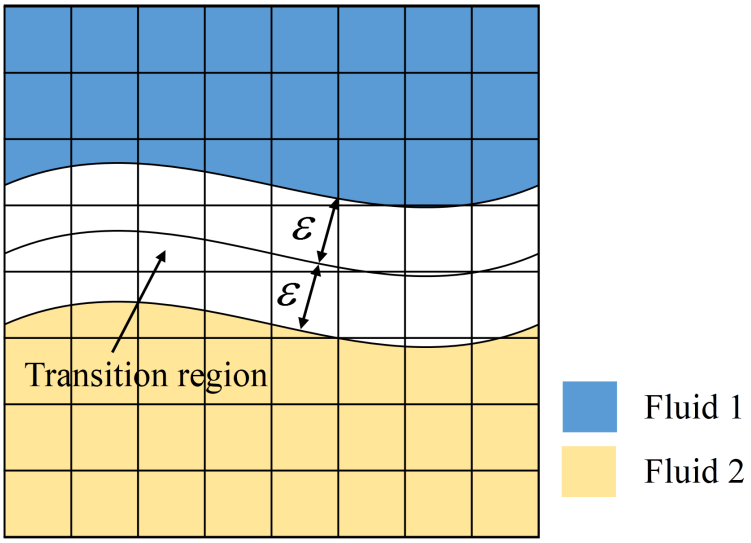

Figure 2.3: Schematic of the transition region around the interface.

fraction $F_{i,j}$ in each cell (i, j) which is defined as

$$F_{i,j} = \begin{cases} 0 & \text{if it is a fluid 2 cell,} \\ 1 & \text{if it is a fluid 1 cell,} \\ 0 < F < 1 & \text{if it is a two-phase cell.} \end{cases} \tag{2.4}$$

Figure 2.2 shows the typical distribution of void fraction field around the interface. When the distribution of void fraction function is sharp, the physical properties undergo sharp jump across the interface. This leads to convergence problem in the solution algorithm. In order to overcome that the physical properties are smoothed over a thin region around the interface as shown in Fig. 2.3. This thin region is the numerical thickness of the interface across which the physical properties are interpolated in order to overcome the issues related to convergence. The transition region has a thickness of 2ε as shown in Fig. 2.3.

The advection equation for volume fraction is solved to capture the motion of the interface. The advection equation for the volume fraction is given as

$$\frac{\partial F}{\partial t} + \mathbf{V} \cdot \nabla F = 0. \tag{2.5}$$

Equation 2.5 is then solved using the operator split advection scheme [11]. In oper-

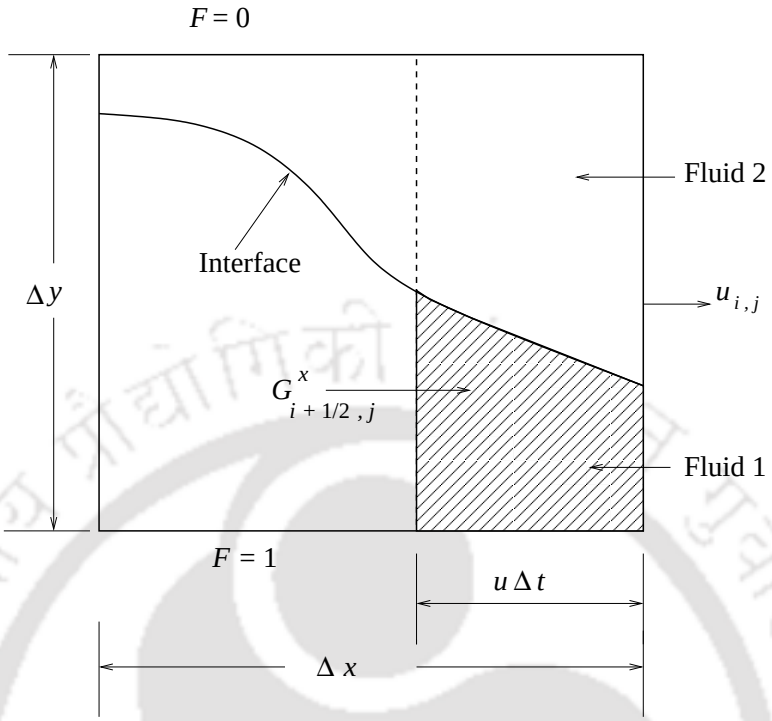

Figure 2.4: A representative diagram showing the advection of volume fraction into the neighboring cell on the right. The fluid to the right of the dotted line is advected to the neighboring right cell.

ator split method, Eq. 2.5 is reformulated as

$$\frac{\partial F}{\partial t} + \nabla \cdot (\mathbf{V}F) = F\nabla \cdot \mathbf{V}. \tag{2.6}$$

Equation 2.6 is then discretized using finite difference scheme and solved using the operator split advection scheme. In operator split algorithm, Eq. 2.6 is first split into two equations in the two orthogonal directions as

$$\frac{\partial F}{\partial t} + \frac{\partial (Fu)}{\partial x} = F\frac{\partial u}{\partial x} \tag{2.7}$$

$$\frac{\partial F}{\partial t} + \frac{\partial (Fv)}{\partial y} = F\frac{\partial v}{\partial y} \tag{2.8}$$

The conservation of F is maintained by employing an implicit scheme in the first sweeping direction and an explicit scheme in the second direction as suggested by Puckett et al. [11]. Equations 2.7 and 2.8 are thus discretized as

$$F^*_{i,j} = F^n_{i,j} + \frac{\Delta t}{\Delta x}(\delta G^x_{i-1/2,j} - \delta G^x_{i+1/2,j}) + \frac{\Delta t}{\Delta x} F^*_{i,j}(u_{i+1/2\,,j} - u_{i-1/2\,,j}), \tag{2.9}$$

$$F^{n+1}_{i,j} = F^*_{i,j} + \frac{\Delta t}{\Delta y}(\delta G^y_{i,j-1/2} - \delta G^y_{i,j+1/2}) + \frac{\Delta t}{\Delta y} F^*_{i,j}(v_{i\,,j+1/2} - u_{i\,,j-1/2}). \tag{2.10}$$

Here, $\delta G^x_{i+1/2,j} = (uF)_{i+1/2,j}$ is the amount of fluid volume fraction fluxed through the right face of (i,j) cell and $\delta G^y_{i,j+1/2} = (vF)_{i,j+1/2}$ denotes the flux across the top edge of the (i,j) cell. The superscripts $n, n+1$ denote time time instances at the current and next iteration levels, and, Δt is the time step. $F^*_{i,j}$ denotes the intermediate volume fraction value in a cell (i,j) after the first sweep.

The volume fluxes in Eqs. 2.9 and 2.10 can be calculated using geometrical interpretation of flux as shown in Fig. 2.4. Suppose $u_{i+1/2,j}$ is positive. The cell (i,j) can be divided into two disjoint rectangles having areas $u_{i+1/2,j}\Delta t\Delta y$ on the right and $\left(\Delta x - u_{i+1/2,j}\Delta t\right)\Delta y$ on the left, as shown in Fig. 2.4. The fluid in the first rectangle will cross the right edge of the cell (i,j) during time Δt. The flux of a particular fluid across this edge is equal to the amount of that particular fluid contained in that rectangle. In VOF method, this can be determined by the location of the reconstructed interface. Thus if $G^x_{i+1/2,j}$ is the volume of fluid 1 in this rectangle then the flux is given by

$$\delta G^x_{i+1/2,j} = \frac{u_{i+1/2,j} G^x_{i+1/2,j}}{u_{i+1/2,j}\Delta t\Delta y} = \frac{G^x_{i+1/2,j}}{\Delta t\Delta y}. \tag{2.11}$$

The value of volume flux given by Eq. 2.11 is used in Eq. 2.9 to calculate the intermediate volume fraction $F^*_{i,j}$ and the interface in reconstructed in all cells using the intermediate values of volume fractions. Next, the vertical fluxes $G^y_{i,j+1/2}$ are determined by a geometric construction analogous to the one described for the horizontal fluxes, and the volume fractions at a new time level $F^{n+1}_{i,j}$ are found by inserting these vertical fluxes in Eq. 2.10. The methodology is made second order accurate by alternating the sweep direction at each step of time advancement. This is commonly known as *Strang splitting* [19].

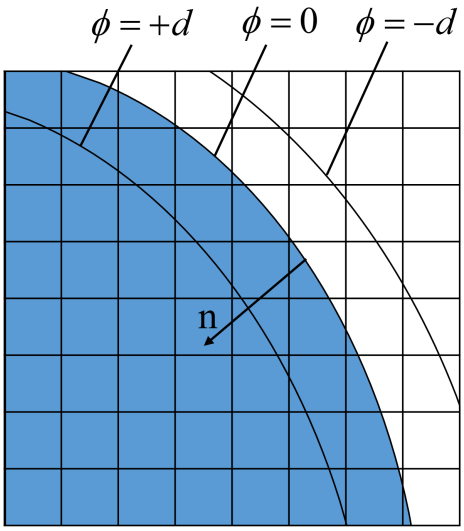

Figure 2.5: A representative diagram showing the distribution of level set function ϕ around the interface.

2.4 Level set algorithm

In Level Set method, a smooth level set function ϕ is used to represent the interface. The level set function $\phi(\mathbf{r}, t)$ at a point with position vector $\mathbf{r}$ and at a time instant t is given as

$$\phi(\mathbf{r},t)\begin{cases} < 0 & \text{in the fluid 2 region,} \\ = 0 & \text{at the interface,} \\ > 0 & \text{in the fluid 1 region.} \end{cases} \tag{2.12}$$

In the present solver, the level set function is maintained as a signed distance from the interface in the neighborhood as shown in Fig. 2.5. Here, the level set function is given as

$$\phi(\mathbf{r},t)\begin{cases} = -d & \text{in the fluid 2 region,} \\ = 0 & \text{at the interface,} \\ = +d & \text{in the fluid 1 region,} \end{cases} \tag{2.13}$$

where $d = d(\mathbf{r})$ is the shortest distance of the interface from the point having position vector $\mathbf{r}$.

In this method using the known initial position of the interface, the advection equation for level set function is solved to capture the interface at next time step

which is given as

$$\frac{\partial \phi}{\partial t} + \mathbf{V} \cdot \nabla \phi = 0. \tag{2.14}$$

The convective term of Eq. 2.14 is discretized using the essentially non-oscillatory (ENO) scheme [20]. The level set function is reinitialized to the exact signed normal distance after each time step. Here, the reinitialization of the level set function is done from the reconstructed interface by coupling level set function with volume fraction. The solution methodology is made second order accurate by alternating the sweep direction at each step of time advancement.

2.5 CLSVOF advection algorithm

The CLSVOF method is an attempt to combine the advantage of the level set approach and volume-of-fluid approach. Here, the VOF algorithm ensures the mass conservation and the level set function is computed additionally because its smoothness allows one to use simple finite difference scheme to calculate the geometric properties of the interface. The CLSVOF approach, the interface advection is achieved in the following steps:

1. The intermediate volume fraction $F^*_{i,j}$ is obtained by solving the Eq. 2.9 in the first sweep direction (say $x-$direction).

2. After $F^*_{i,j}$ is obtained, ϕ is advected in the same sweeping direction by solving the split form of Eq. 2.14. That is, for the sweep in the $x-$direction, we solve

$$\frac{\partial \phi}{\partial t} + u\frac{\partial \phi}{\partial x} = 0. \tag{2.15}$$

   The discretization of the convective term in Eq. 2.15 is done by employing a second order ENO scheme [20].

3. The geometric properties of the interface are calculated based on the smooth level set function ϕ. The interface normal and the curvature are calculated as

$$\hat{\mathbf{n}} = \frac{\nabla \phi}{|\nabla \phi|} \tag{2.16}$$

$$\kappa = -\nabla \cdot \left(\frac{\nabla \phi}{|\nabla \phi|} \right). \tag{2.17}$$

The smoothness of the level set field allows the central finite-difference scheme for discretization in every two-phase cell [21]. The perpendicular distance between cell center and interface, l, is adjusted to match the given volume fraction with that of the reconstructed interface (described in Sec. 2.6).

4. The volume fraction is then advected in the second direction (say $y-$direction) by solving Eq. 2.10 that leads to the final distribution of volume fraction field $F_{i,j}^{n+1}$ in the current time step.

5. The intermediate level set function is advanced in the $y-$ direction by solving the advection equation

$$\frac{\partial \phi}{\partial t} + v \frac{\partial \phi}{\partial y} = 0. \tag{2.18}$$

The discretization scheme is the same as described in step 2.

6. The interface is again reconstructed based on updated values of F and ϕ as described in step 3.

7. The finite-difference scheme for advancing ϕ (steps 2 and 5) does not conserve its distance function attributes. Therefore the level set function is reinitialized in all cells based on the reconstructed interface. The algorithm to reinitialize ϕ is implemented following the method of Sussman et al. [14].

The solutions of the advection equations are be made second order accurate by alternating the sweep direction in each step of time advancement.

2.6 Interface construction and smoothing

In the present solver, the interface construction is accomplished using the PLIC (piecewise linear interface calculation) method as described by Youngs [10]. In the PLIC method, the portion of the interface in each cell is approximated by a straight line. The interface unit normal $\hat{\mathbf{n}}$ is calculated in each cell which specifies the alignment of the interface in each cell. $\hat{\mathbf{n}}$ is a unit normal to the approximated

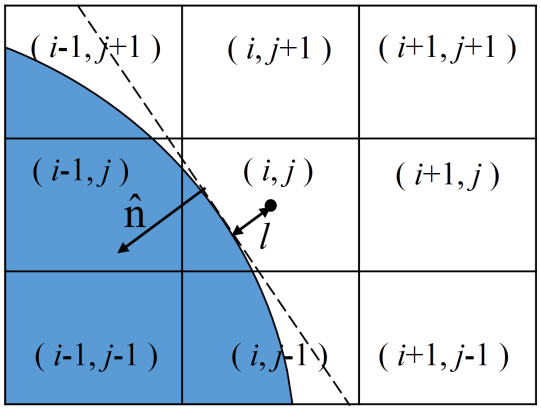

Figure 2.6: Representation of the interface in a cell (i, j) in terms of interface unit normal $\hat{\mathbf{n}}$ and the distance of the interface from the cell center l. The dotted line represents the approximated interface in a cell (i, j).

linear interface in each cell. The initial value of $\hat{\mathbf{n}}$ a two-phase cell (i, j) is calculated from Youngs' [10] method based on the volume fraction in that cell $F_{i,j}$ and volume fractions of its neighbor cells. The initial value of the normal $\mathbf{n} = (n^x, n^y)$, having components n^x and n^y in $x-$ and $y-$directions, is calculated in a cell (i, j) as

$$n^x_{i,j} = \frac{1}{8\Delta x}\left(F_{i+1,j+1} + 2F_{i+1,j} + F_{i+1,j-1} - F_{i-1,j+1} - 2F_{i-1,j} - F_{i-1,j-1}\right), \quad (2.19)$$

$$n^y_{i,j} = \frac{1}{8\Delta y}\left(F_{i+1,j+1} + 2F_{i,j+1} + F_{i-1,j-1} - F_{i+1,j-1} - 2F_{i,j-1} - F_{i-1,j-1}\right). \quad (2.20)$$

The value of $\hat{\mathbf{n}}$ can be found as

$$\hat{\mathbf{n}} = \frac{\mathbf{n}}{|\mathbf{n}|}. \quad (2.21)$$

The position of the interface is adjusted in such a way that it divides the cell into two areas that match the two volume fractions. In order to implement, the distance of the interface from the cell center (l) is calculated in each cell. Figure 2.6 shows the representation of the interface (dotted line) in a cell (i, j) in terms of the unit normal $\hat{\mathbf{n}}$ and the distance of the interface from the cell center l.

From a macroscopic perspective, the interface has zero thickness. However, the sharp jump of physical properties across the interface may bring about inaccuracy in the solution and also creates convergence problem. In order to avoid the mathematical discontinuity, a finite thickness of the interface has to be considered while

capturing it numerically. Therefore the properties are smoothed in a thin region near the interface. This thin region is the numerical thickness of the interface on which the physical properties are interpolated. The code has been tested rigorously for different conditions to optimize this parameter. In our simulations, we have considered the interface numerical thickness in the range $0.5\Delta x - 1.5\Delta x$, where Δx is the size of each grid cell. In CLSVOF approach, the smoothening is performed using a smoothed Heaviside function which is defined based on the level set function. The Heaviside function is defined as

$$H(\phi) = \begin{cases} 0 & \text{if } \phi < -\varepsilon, \\ \frac{1}{2} + \frac{\phi}{2\varepsilon} + \frac{1}{2\pi}\left[\sin\left(\frac{\pi\phi}{\varepsilon}\right)\right] & \text{if } |\phi| \leq \varepsilon, \\ 1 & \text{if } \phi > +\varepsilon, \end{cases} \tag{2.22}$$

where ε is the numerical thickness of the interface on each side as shown in Fig. 2.3. The total numerical thickness of the interface would be 2ε. The density and the viscosity are calculated in each cell based on this smoothed Heaviside function as

$$\rho(\phi) = \rho_1 H(\phi) + \rho_2(1 - H(\phi)) \tag{2.23}$$

and

$$\mu\left(\phi\right) = \mu_1 H(\phi) + \mu_2\left(1 - H(\phi)\right). \tag{2.24}$$

Here, μ_1 and μ_2 are the viscosities of fluid 1 and fluid 2, respectively. The smoothed density and viscosity are used to solve the Navier-Stokes equations using the single fluid model to get the updated flow field.

2.7 Surface tension model

Efficient modelling of surface tension effect is very important for accurate numerical modelling of free surface flows. One such efficient model was formulated by Brackbill et al. [16] called as continuum surface force (CSF) model which has been widely used to model the surface tension effect. The present solver is also developed using the CSF model of Brackbill et al. [16]. In CSF model, the surface tension force per unit

volume can be defined as

$$\mathbf{f}_{sv} = \mathbf{f}_{sa}\delta_s \tag{2.25}$$

where δ_s is the Dirac delta function which is zero everywhere except at the interface. $\mathbf{f}_{sa}$ is the surface tension force per unit interfacial area. It has two components, one normal component $\mathbf{f}_{sa}^{\text{normal}}$ and one tangential component $\mathbf{f}_{sa}^{\text{tangential}}$. Thus,

$$\mathbf{f}_{sa} = \mathbf{f}_{sa}^{\text{normal}} + \mathbf{f}_{sa}^{\text{tangential}}. \tag{2.26}$$

The normal component and the tangential component can be represented as $\mathbf{f}_{sa}^{\text{normal}} = \sigma\kappa\hat{\mathbf{n}}$ and $\mathbf{f}_{sa}^{\text{tangential}} = \nabla_s\sigma$, where σ is the surface tension coefficient, κ is the mean curvature of the interface, $\hat{\mathbf{n}}$ is the unit normal vector of the interface and ∇_s is the surface gradient. Hence, the surface tension force term can be represented as

$$\mathbf{f}_{sa} = \sigma\kappa\hat{\mathbf{n}} + \nabla_s\sigma. \tag{2.27}$$

Present investigations are performed under isothermal condition and the concentration gradient along the interface is neglected. Hence, the surface tension coefficient σ is assumed constant and $\nabla_s\sigma$ is neglected. Thus, we get,

$$\mathbf{f}_{sv} = \sigma\kappa\hat{\mathbf{n}}\delta_s. \tag{2.28}$$

Using the model of Brackbill et al. [16] the Dirac delta function can be simplified as

$$\delta_s = |\mathbf{n}|. \tag{2.29}$$

Therefore, the surface tension term incorporated in the momentum equation (Eq. 2.2) takes the form

$$\mathbf{f}_{sv} = \sigma\kappa|\mathbf{n}|\hat{\mathbf{n}} = \sigma\kappa\mathbf{n}. \tag{2.30}$$

Therefore, a critical component of surface tension calculation method is the accuracy of calculating the normal vector $\mathbf{n}$ and curvature κ. In the present numerical model, the CLSVOF approach is used to calculate $\mathbf{n}$ and κ as suggested by Sussman et

al. [14]. Interface normal vector is calculated from the Heaviside function as

$$\mathbf{n} = \nabla\phi. \tag{2.31}$$

The curvature κ is then calculated form the smooth level set function as

$$\kappa = -\nabla \cdot \hat{\mathbf{n}} = -\nabla \cdot \frac{\nabla\phi}{|\nabla\phi|}. \tag{2.32}$$

2.8 Numerical solution of momentum equations

In the present numerical methodology, the one-fluid model has been deployed for solving the momentum equations in the entire domain. The density ρ and the viscosity μ are calculated based on a smoothed Heaviside function for the treatment of discontinuity across the interface as described in Sec. 2.6. The surface tension effect is modeled using the CSF model as described in Sec. 2.7. Therefore, using the smoothed density $\rho(\phi)$ and the smoothed viscosity $\mu(\phi)$, the momentum equation (Eq. 2.2) can be written as

$$\rho(\phi)\left[\frac{\partial \mathbf{V}}{\partial t} + \nabla \cdot (\mathbf{V}\mathbf{V})\right] = -\nabla p + \rho(\phi)\mathbf{g} + \nabla \cdot (2\mu(\phi)\mathbf{D}_v) + \sigma\kappa(\phi)\mathbf{n}(\phi). \tag{2.33}$$

The discretization of momentum equation is performed using finite difference scheme as

$$\begin{aligned}\mathbf{V}^{n+1} = \mathbf{V}^n &- \left(\nabla \cdot (\mathbf{V}^n\mathbf{V}^n)\right)\Delta t + \mathbf{g}\Delta t \\ &+ \left(\frac{-\nabla p^{n+1} + \nabla \cdot 2\mu\left(\phi^n\right)\mathbf{D}_v^n + \sigma\kappa\left(\phi^n\right)\mathbf{n}\left(\phi^n\right)}{\rho\left(\phi^n\right)}\right)\Delta t.\end{aligned} \tag{2.34}$$

The convective terms in the momentum equations are discretized using the higher order essentially non-oscillatory (ENO) scheme as described by Chang et al. [20] and the remaining space derivatives are discretized using central difference scheme. The discretized form of the momentum equation is solved explicitly for the known volume fraction field F^n at a time level n, which gives rise to a provisional velocity field for the next time level. Such a velocity field may not be divergence free since it does

not satisfy continuity equation in each cell. The compliance of continuity equation is achieved by solving the corresponding pressure correction equations using the HYPRE multi-grid solver [22]. Thus, after having achieved a divergence free velocity field, the converged solution is obtained at a new time level $n+1$. Using this new velocity field, the advection equations of volume fraction and level set function are solved to obtain the new volume fraction field F^{n+1} and the level set function ϕ^{n+1} which are essential for interface reconstruction.

The solution scheme followed for solving velocity field is thus second order accurate in space and first order accurate in time. The advection algorithm and the explicit treatment of convective terms lead to the time constraints in the numerical treatment of the problem. In the advection algorithm, the sum of the volume fluxed over the cell faces must be smaller than the total cell volume. This leads to the limiting condition

$$\Delta t \leq \left(\frac{\Delta x}{|u|_{max}} + \frac{\Delta y}{|v|_{max}} \right). \tag{2.35}$$

Furthermore, the explicit treatment of surface tension term also results in a restriction as given in Brackbill et al. [16] as

$$\frac{C_\phi \Delta t}{\Delta x} < \frac{1}{2}. \tag{2.36}$$

Here, C_ϕ is the capillary wave phase velocity and is given by,

$$C_\phi = \left[\frac{\sigma \pi}{\Delta x(\rho_1 + \rho_2)} \right]^{1/2}. \tag{2.37}$$

Therefore, the capillary time step limit can be specified as

$$\Delta t < \left[\frac{(\rho_1 + \rho_2)\Delta x^3}{4\pi\sigma} \right]^{1/2}. \tag{2.38}$$

2.9 Summary

A detailed description of the numerical methodology used in the present investigations has been presented in the present Chapter. The interface construction tech-

nique and the surface tension model have been described. The numerical methodology used in the investigations can be summarized in the following steps:

1. The interface is defined in terms of the unit normal $\hat{\mathbf{n}}$ and the distance of the interface l from the cell center by using Youngs' method as described in Sec. 2.6.

2. The velocity at a new time level is provisionally predicted by solving the momentum Eq. 2.34. The surface tension term is handled using the continuum surface force model as described in Sec. 2.7

3. The pressure equation is solved to get the correct pressure and correspondingly the correct velocity field at the new time level as explained in Sec. 2.8.

4. Based on the new velocity field, the advection equations of volume fraction (F) and level set function (ϕ) are solved to get the updated values at the new time step and the interface is reconstructed using the updated values of F and ϕ as described in Sec. 2.5. After finding the updated ϕ and F, the level set function is reinitialized to the exact signed normal distance from the reconstructed interface by coupling the level set function ϕ with the volume fraction F.

Steps 2-4 are repeated in each step of time advancement.

Chapter 3

Dynamics of formation and oscillation of non-spherical drops

3.1 Introduction

Drop formation is a ubiquitous natural phenomenon having a wide variety of application in science and technology. It bears far-reaching implications in a variety of engineering processes such as measurement of surface tension by the drop weight method [23, 24], separation and extraction processes [25], coarsening of emulsions [26], functioning of sprays [27, 28], inkjet printing [29], cell and organ printing [30], to name a few. In addition, the study of drop formation has been a topic of scientific research for more than a century due to the richness of underlying physics [23, 31, 32].

Drop formation can be broadly classified into two categories, namely dripping and jetting. At low flow rate, the drops form periodically one after another, which is commonly known as the dripping regime. With the increase of flow rates, the system transitions into the jetting mode where the inertia force becomes a dominating factor and drops break up from the end of a long jet of liquid, which is inherently unstable. Many investigations have been performed experimentally, theoretically and numerically to uncover the fascinating aspects of dripping [33–40] and jetting mode [41–46] of drop formation as well as transition from dripping to jetting mode [47–51].

The shape of the drop at the time of pinch-off is a very important parameter

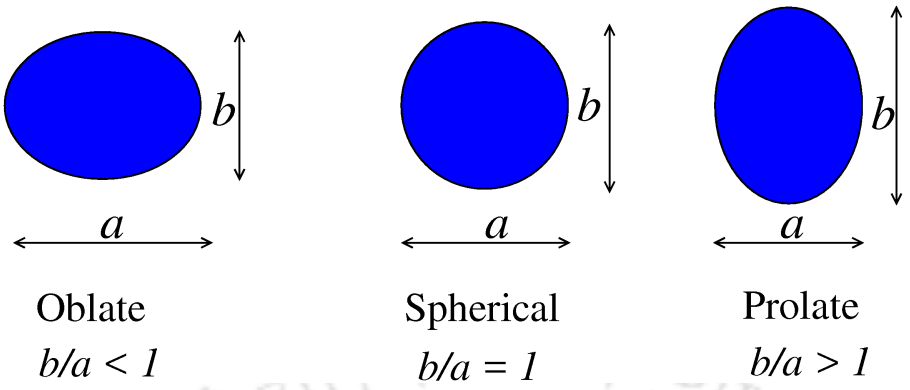

Figure 3.1: Different shapes of a liquid drop. Here, a and b represent the axis length of the drop along the radial and axial directions. The aspect ratio ($AR = b/a$) is greater than unity for a prolate shaped drop ($AR > 1$), equal to unity for a spherical drop ($AR = 1$) and is less than unity for an oblate shaped drop ($AR < 1$).

in its consequent dynamics. For example, recent investigations [52, 53] reported that large bubble formation during the impact of a drop on a liquid pool takes place only for prolate shaped drops. A prolate shaped drop is the one in which the aspect ratio is greater than unity ($AR > 1$). The aspect ratio AR is defined as $AR = b/a$, where a and b are the radial (r) and axial (z) axis lengths of the drop. Based on aspect ratio we may get two other shapes of drops, namely oblate ($AR < 1$) and spherical ($AR = 1$) as shown in Fig. 3.1. For a non-spherical drop, its shape oscillates between the prolate and oblate shapes while translating through a surrounding medium. Although numerous investigations are performed on drop formation and on the associated instability dynamics, the spatio-temporal events concerning the dynamical evolution of the shape of the drop remain far from being comprehensively addressed, which motivated us to study these complex phenomena again.

The motion of a liquid drop translating under the action of gravity, through an unbounded quiescent fluid is a fundamental problem with a very long history in the field of fluid mechanics. A solution in the creeping flow regime was obtained over hundred years ago, attributed to Hadamard (1911) and Rybczynski (1911), with the assumption that the drop remains exactly spherical and neglecting the inertial term. Nearly fifty years later, Taylor and Acrivos [54] investigated it considering the inertia effect and showed that the drop deforms into an oblate spheroid for small values of Weber number ($\equiv \rho V_t^2 R_d/\sigma$), and the shape approaches a spherical cap with further increase in Weber number. They defined Weber number based on the

equivalent radius of a spherical drop R_d and σ, ρ and V_t are surface tension coefficient, density of the surrounding fluid and terminal velocity of the drop, respectively. The stability of a drop moving under the action of gravity was studied by Kojima et al. [55] and Koh and Leal [56], and they concluded that the instability was predicted to appear at the rear end of the drop as a growing tail for an initially prolate shape, and as a growing indentation or cavity for an initially oblate shaped drop. The deformation of the drop depends on the viscosity ratio between the drop fluid and the translating medium. In the case of an initially prolate shaped drop, viscosity increases its stability. However, the contrary is true in the case of an initially oblate shaped drop. The non-modal stability analysis of Gallino et al. [57] predicts that when the viscosity of the surrounding fluid is more than the drop fluid, the external viscous effect overcomes the internal one and the rear side of the drop is stretched outward to form a protrusion. On the contrary, when the drop viscosity is more than the surrounding fluid, it is prone to be sucked inward to form an indentation.

Koh and Leal [58], from their experimental investigation, reported that the stability behavior of a drop depends on its initial deformation. They observed that a drop reverts back to a spherical shape when the degree of deformation is small. However, when the degree of deformation is large, it deforms continuously. If the amplitude of oscillations becomes more than 10% the drop radius, the nonlinear effects such as dependence of oscillation frequency on amplitude, the asymmetry of oscillation amplitude are observed [59]. Within that limit, the oscillation of a drop is well predicted by the linear theory. The shape of a fluid particle is not invariant and it deforms according to the local stresses imparted by the surrounding environment [60–62]. The surface tension forces always drive a free particle toward a spherical shape, whereas initial conditions and/or fluid-dynamic forces are the primary sources of non-sphericity [63]. Whenever the fluid dynamic stress overcomes the surface tension force, the drop undergoes continuous deformation and finally breaks up. Based on the magnitude of the fluid dynamic forces different modes of break-up are observed, as reported in Han and Tryggvason [64]. Stone and Leal [65] studied the effect of surfactants on the deformation of drops, and observed that the presence of surfactants decreases the interfacial tension which increases the deformation of the drop. Investigations are also performed on the shape of a non-Newtonian drop translating through a Newtonian or non-Newtonian surrounding medium [66–68].

A falling drop does not show path instabilities, unlike the rising bubbles, irrespective of the shape of the drop [69]. Earlier investigations [52, 69, 70] suggest that

a non-spherical drop oscillates periodically between the prolate and oblate shapes. Therefore the initial shape of the drop at the time of pinch-off is a prime parameter governing its oscillatory motion during translation through another fluid. The current work is a comprehensive study on the generation of non-spherical drops. The effects of inertial, capillary, viscous, and gravitational forces are all accounted for, in order to investigate different formation dynamics and to elucidate the fate of the resulting drop's shape during pinch-off. Moreover, a question that arises then is can a drop be generated which does not oscillate after pinch-off. The present study aims at answering the above question emphasizing the pinch-off dynamics which make a drop to oscillate after pinch-off. Furthermore, the oscillating behavior of a drop while falling through a surrounding medium has been investigated in this study.

3.2 Formulation

3.2.1 Computational domain

The simulations are performed using CLSVOF method in axisymmetric coordinates (r, z) as shown in Fig. 5.2. The drop liquid (Fluid 1) is injected through an orifice of radius R on a horizontal wall at a constant flow rate $\dot{Q}_d$, into a quiescent surrounding medium (Fluid 2). The computational domain used in the simulations has width $W \approx 5R$ and height $H \approx 200R$. The larger height is taken to capture the movement of the drop after pinch-off. The origin is chosen at the center of the orifice and gravity acts along the direction of $z-$axis, as shown in Fig. 5.2. The three-phase contact circle where the drop base, outer surrounding medium, and the orifice rim meet, remains pinned to the sharp edge of the orifice.

3.2.2 Boundary conditions

A parabolic velocity profile is imposed at the orifice inlet satisfying the conditions of desired liquid injection rate. This can be expressed in terms of the velocity components (u, v) along the $r-$ and $z-$directions as

$$u = 0 \quad ; \quad v = 2v_{avg}\left[1 - \left(\frac{r}{R}\right)^2\right]. \tag{3.1}$$

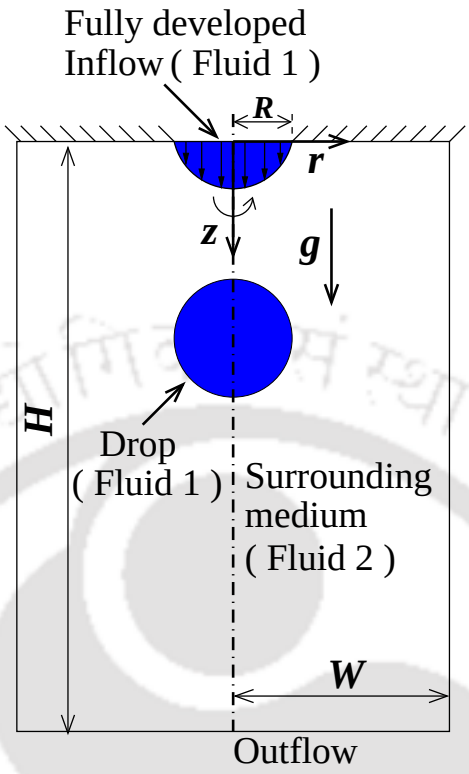

Figure 3.2: Schematic of the computational domain used in the numerical simulations. Here R is the radius of the orifice. The computational domain has a width $W = 5R$ and a height of $H = 200R$. Gravity acts along the direction of $z-$axis.

Here, v_{avg} is the average flow velocity through the orifice inlet calculated as $v_{avg} = \dot{Q}_d/\pi R^2$. At the other points across the top boundary i.e. across the wall, no-slip and impermeability condition is deployed.

$$u = v = 0 \quad ; \quad \text{for} \quad R \leq r \leq W \tag{3.2}$$

At the bottom boundary, outflow boundary condition is deployed having Neumann boundary condition for both the velocity components.

$$\frac{\partial u}{\partial z} = \frac{\partial v}{\partial z} = 0 \tag{3.3}$$

In our computational domain we are performing axisymmetric simulations and the axis of symmetry lies on the left boundary. At the axis of symmetry, no fluid exits

or enters the domain. This can be mathematically expressed as

$$u = 0, \quad \frac{\partial v}{\partial r} = 0. \tag{3.4}$$

The same boundary conditions can be applied on the right boundary as the right boundary is considered to be frictionless. The Neumann pressure boundary condition is applied in all the boundaries, except at the bottom boundary where the pressure is equal to the atmospheric pressure P_{atm}.

3.2.3 Initial condition

Initially, the drop is assumed to be a hemisphere having radius equal to that of the orifice radius. The initial state of the static drop can be defined as

$$r^2 + z^2 = R^2. \tag{3.5}$$

Both the drop and the surrounding medium is assumed to be initially quiescent having a constant pressure equal to the atmospheric pressure.

$$u = v = 0, \quad p = P_{atm} \quad \text{at } t = 0. \tag{3.6}$$

3.2.4 Non-dimensional parameters

The dynamics of dripping is governed by three dimensionless parameters [37, 39], namely Bond number $Bo\,(\equiv \rho_1 g R^2/\sigma)$, Weber number $We\,\left(\equiv \rho_1 v_{avg}^2 R/\sigma\right)$ and Ohnesorge number $Oh\,\left(\equiv \mu_1/\sqrt{\rho_1 \sigma R}\right)$. Bond number measures the relative importance of the gravity force over surface tension force, Weber number expresses relative importance of the inertia force over surface tension force, and Ohnesorge number measures relative importance of the viscous force over surface tension force. In addition, two other pertinent non-dimensional parameters pertinent for our study are density ratio $\rho_r\,(\equiv \rho_2/\rho_1)$ and viscosity ratio $\mu_r\,(\equiv \mu_2/\mu_1)$ which accounts the dynamic effect of surrounding medium. Here, the orifice radius (R) is used as the characteristic length scale and the capillary time $t_c\,\left(\equiv \sqrt{\rho_1 R^3/\sigma}\right)$ is used as the characteristic time scale.

3.3 Validation and grid-independent test

In order to check the validity of the numerical results, we compared the results obtained from the simulations with that obtained from the experiments. Figure 3.3 illustrates the comparison of the drop shape at the incipience of pinch-off, predicted by the present computed result (red line) superimposed on the experimental result of Subramani et al. [39]. The dimensionless parameters are $We = 0.119$, $Bo = 0.33$, $Oh = 0.13$, $\rho_r = 0.00105$ and $\mu_r = 0.0006$. An excellent agreement has been observed between the present numerical result and the experimental result of Subramani et al. [39], as depicted in Fig. 3.3.

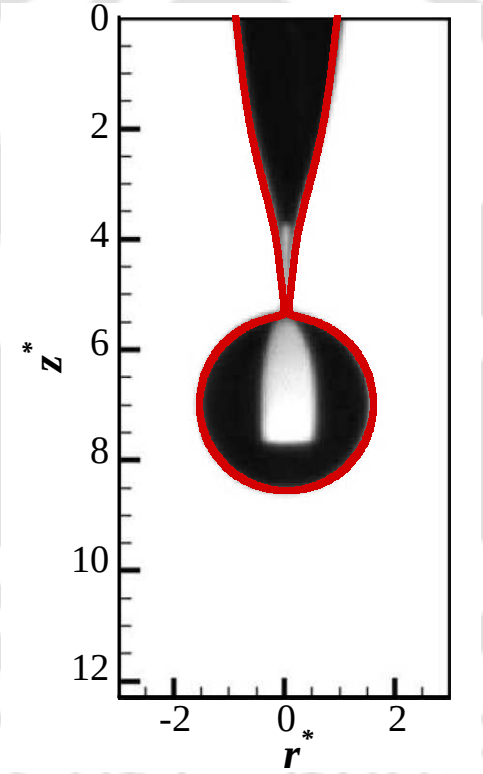

Figure 3.3: Comparison between the numerical results (red line) and the experimental results of Subramani et al. [39] at the incipience of drop pinch-off during the formation of a drop from an orifice. The corresponding dimensionless parameters are $We = 0.119$, $Bo = 0.33$, $Oh = 0.13$, $\rho_r = 0.00105$ and $\mu_r = 0.0006$.

In order to make a quantitative comparison, the values of dimensionless limiting length ($L_d^* = L_d/R$) and dimensionless detached primary drop volume ($V_d^* = V_d/R^3$) of Fig. 3.3 are calculated and presented in Table 3.1, along with the experimental results of Subramani et al. [39]. Here, the dimensional limiting drop length, denoted

Table 3.1: Comparison between the numerical results of present investigation and the experimental results of Subramani et al. [39]. The dimensionless parameters are $We = 0.119$, $Bo = 0.33$, $Oh = 0.13$, $\rho_r = 0.00105$ and $\mu_r = 0.0006$.

Parameters	Experimental	Present computation
Limiting length, L_d^*	8.6 ± 0.1	8.7
Drop Volume, V_d^*	17.4 ± 0.3	17.68

Table 3.2: Comparison between the numerical results obtained from different mesh resolution. The non-dimensional parameters are $We = 0.119$, $Bo = 0.33$, $Oh = 0.13$, $\rho_r = 0.00105$ and $\mu_r = 0.0006$.

Grid mesh	V_d^*	Percentage change (%)
50×2000	17.16	–
75×3000	17.43	1.57
100×4000	17.48	0.28
150×6000	17.50	0.11

by L_d, is the length measured from the orifice to the drop tip at the moment of pinch-off. Similarly, V_d is the volume of the primary drop after pinch-off. Table 3.1 shows that the values obtained from numerical simulations are in excellent agreement with that obtained from experiments.

In order to reveal grid independence, a sample grid independence study has been performed using different mesh resolution. We considered four different grid meshes and calculated the dimensionless detached primary drop volume (V_d^*) for each grid mesh, which is presented in Table 6.1. The non-dimensional parameters considered here are $We = 0.119$, $Bo = 0.33$, $Oh = 0.13$, $\rho_r = 0.00105$ and $\mu_r = 0.0006$. The percentage difference for the grid meshes of size 50×2000 and 75×3000 is approximately 1.57%; for the grid meshes of 75×3000 and 100×4000, it is approximately 0.28%. The percentage difference between the results for the grid meshes of 100×4000 and 150×6000 is approximately 0.11%, which is very small. Therefore, a mesh size of 100×5000 has been chosen for performing the present simulations to optimize the simulation time without compromising the accuracy of the results.

3.4 Results and discussion

When a liquid is continuously injected through an orifice, the volume of the pendant drop increases with time and finally detaches under the action of gravity. In the dripping regime, the flow rate is low and the drops periodically form one after another. With the increase in flow rate, the formation rate increases and finally a transition from dripping to jetting mode is observed. In the present investigation, we are interested in the dynamics of a single drop and we limit our study to dripping mode only.

3.4.1 Effect of inertia

During the formation of a drop from an orifice, initially the volume of the drop protruding out of the orifice is sufficiently small and the surface tension holds the drop pendant from the orifice without allowing it to fall. Because of continuous flow through the orifice, the volume of the pendant drop increases continuously. Once the drop grows larger than a certain size, the surface tension force can no longer balance the gravitational force that pulls the drop down [71]. Thereafter, the drop rapidly elongates and the diameter reduces initiating the necking. The slender neck finally merges at the central axis and a drop separates from the fluid attached to the orifice. Figure 3.4 demonstrates the necking phenomenon of a pendant drop at different instants of time leading to pinch-off. The temporal variation of the neck radius is

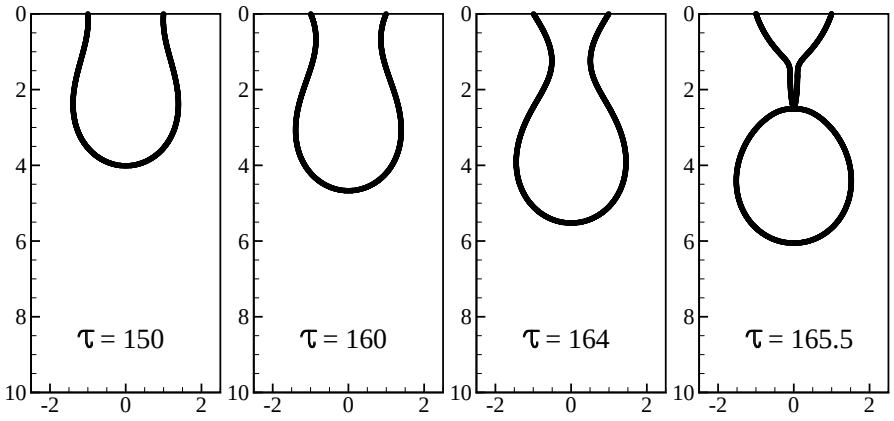

Figure 3.4: Interface profiles at different instants of time showing the growth of the neck in a pendant drop. The dimensionless parameters are $We = 0.00098$, $Bo = 0.2741$, $Oh = 0.0032$, $\rho_r = 0.00118$ and $\mu_r = 0.02$.

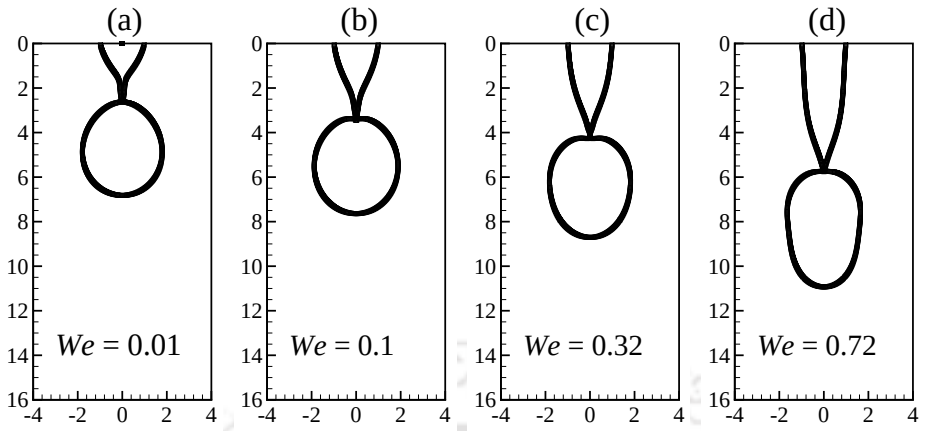

Figure 3.5: Interface profiles of the drop at the incipience of pinch-off for different flow rates. The corresponding We values for (a), (b), (c) and (d) are 0.01, 0.1, 0.32 and 0.72 respectively. The aspect ratio of the drop at the incipience of pinch-off increases with the increase in We. The other dimensionless parameters are Bo = 0.18, Oh = 0.0035, ρ_r = 0.00118 and μ_r = 0.02.

widely studied [38,51,72] and reported that the decrease in neck radius with time can be characterized by a power-law expression $r^*_{neck} \sim \tau^\alpha$ having power-law exponent $\alpha = 2/3$ in the inertia dominated regime and $\alpha = 1$ in the inertia-viscous regime. Here, $r^*_{neck}(= r_{neck}/R)$ is the non-dimensional neck radius and $\tau\,(= (t_p - t)/t_c)$ is the time leading to drop pinch-off. The pinch-off time t_p is the total time required for the pinch-off of the drop. The symbol t is the instantaneous time and t_c is the capillary time as defined earlier. With increased flow rate, the pendant drop grows rapidly and the neck forms at a greater height from the tip of the pendant drop.

Figure 3.5 shows a qualitative comparison of the shape of the drop at the time of pinch-off for different values on We. The other dimensionless parameters are Oh = 0.0035, Bo = 0.18, ρ_r = 0.0018 and μ_r = 0.02. The profiles (a), (b), (c) and (d) in Fig. 3.5 correspond to Weber numbers 0.01, 0.1, 0.32 and 0.72, respectively. Qualitative comparison of the interface profiles at different Weber numbers shows that with increasing values of We the drop shape at the incipience of pinch-off becomes more prolate. With the increase in flow rate $\dot{Q}_d$ the inertial force on the liquid column increases. The liquid inertia acts in the vertical direction and tends to elongate the liquid column, because of which the axial length of the drop, at the time of pinch-off, continuously increases. The limiting length of the drop also increases with the increase in We. This effect of liquid inertia is evident in Fig. 3.6, where the AR of the drop at the incipience of pinch-off is plotted for different values of We.

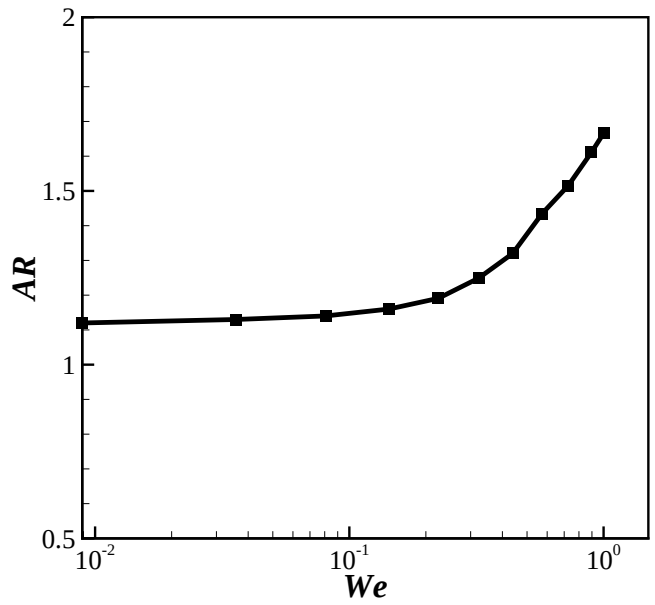

Figure 3.6: The aspect ratio (AR) of the drop at the incipience of pinch-off is plotted at different values of We. The aspect ratio continuously increases with the increase in We. The other dimensionless parameters are same as in Fig. 3.5.

The aspect ratio of the drop at the incipience of pinch-off continuously increases with the increase in We as depicted in Fig. 3.6.

The deformed shape of the drops at larger Weber number is because of the presence of higher shear force arising out of large velocity gradient inside the pendant drop across the radial direction. The velocity contours inside the drop along with the velocity vector plot are shown in Fig. 3.7 (a) and (b) for $We = 1.0$ and 0.0089 respectively. In Fig. 3.7 (a), the $v-$velocity contours are shown on the right side of the symmetry axis and the left side of the symmetry axis shows the velocity vectors for $We = 1.0$. Similarly, Fig. 3.7 (b) show the $v-$velocity contours and the velocity vectors respectively for $We = 0.0089$. It can be seen in Fig. 3.7 (a) that a high gradient of $v-$velocity exists inside the pendant drop across the radial direction. However, at $We = 0.0089$ this gradient is less as seen in Fig. 3.7 (b). The $v-$velocity variation along the radial direction at a particular location (marked by the dashed lines on Fig. 3.7 (a) and (b)) for $We = 1.0$ and $We = 0.0089$ are shown in Fig. 3.7 (c). At higher values of We, the variation of velocity within the pendant drop is large with velocity decreasing progressively towards the outer periphery, as shown in Figure 3.7(c). Because of the existence of large velocity gradient, a strong shear force exists inside the drop which deforms the drop from spherical shape by

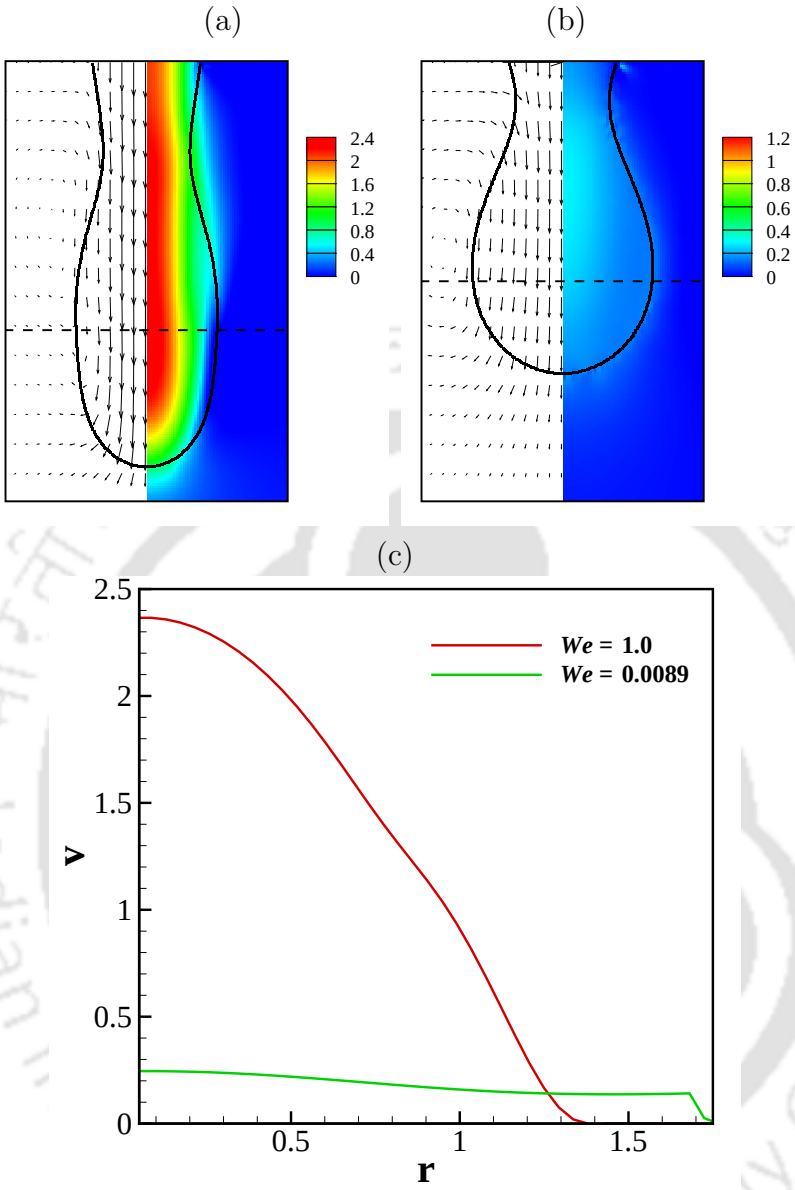

Figure 3.7: The velocity vector plot in the left side of the axis of symmetry and the $v-$velocity contour on the right side of the symmetry axis at a time instant just after the initiation of necking. The corresponding Weber number values in (a) and (b) are $We = 1.0$ and $We = 0.0089$, respectively. (c) Variation $v-$velocity along the radial direction at the locations indicated by the dashed lines in (a) and (b). The other dimensionless parameters in both the cases are same as in Fig. 3.5.

increasing the axial length of the drop. Thus, because of the increase in shear force with the increase in We, the drop assumes a more prolate shape as seen in Fig. 3.6.

3.4.2 Effect of viscosity

The deformation of a pendant drop is brought about by the shear force arising out of the velocity gradient present inside the drop. Increased viscosity damps out the velocity gradient inside the drop and makes it difficult for shear stress to deform the drop. For a drop with low viscosity, the dissipation of the shear stress arising out of rapid fluid movement near the axis of symmetry is substantially weak. This results in a large velocity gradient across the drop with the fluid velocity decreasing progressively towards the outer periphery. Figure 3.8 shows the shape of a drop at the incipience of pinch-off for different values of Ohnesorge number. As depicted in Fig. 3.8, the drop assumes near spherical shape at higher values of Ohnesorge number. This is because with increased values of Oh, the internal velocity field inside the drop is damped out. As a result, the deformation of the drop continuously decreases with increased viscosity. For a highly viscous drop, the velocity profile resembles that of a plug flow with an almost negligible velocity gradient across the drop and the drop assumes a spherical shape at pinch-off. This variation of drop shape with increased viscosity can be observed in Fig. 3.9, which shows that the aspect ratio of the drop continuously decreases with increasing Oh and approaches one at higher values of Oh.

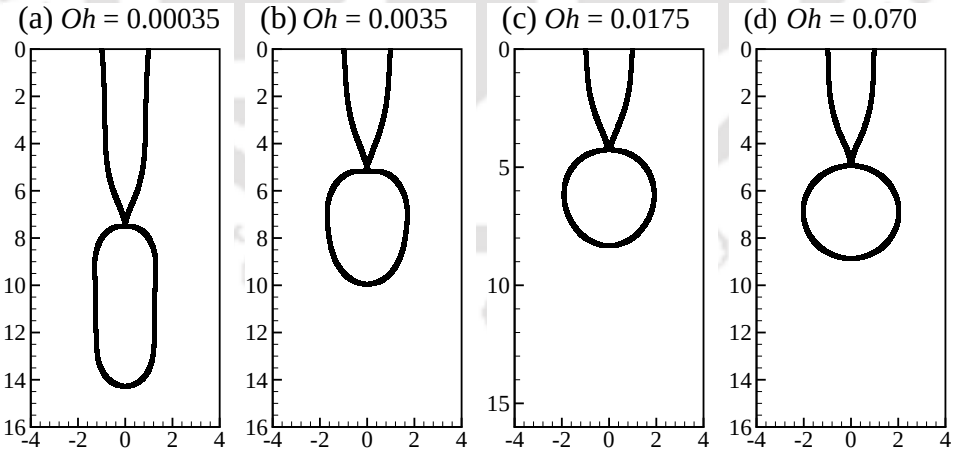

Figure 3.8: Interface profiles of the drop at the incipience of pinch-off for different values of Oh. The profiles in (a), (b), (c) and (d) corresponds to Oh = 0.00035, 0.0035 and 0.0175 and 0.070 respectively. The aspect ratio continuously decreases with the increase in Oh. The other dimensionless parameters are $We = 0.57$, $Bo = 0.18$, $\rho_r = 0.00118$ and $\mu_r = 1.85 \times 10^{-1} - 9.25 \times 10^{-4}$.

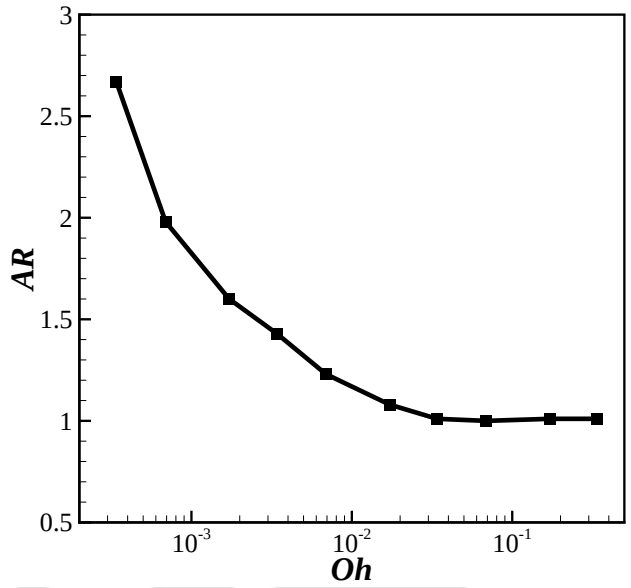

Figure 3.9: The aspect ratio (AR) of the drop at the incipience of pinch-off is plotted at different values of Oh. The aspect ratio continuously decreases with the increase in Oh. The other dimensionless parameters are same as in Fig. 3.8.

3.4.3 Effect of surrounding fluid

The dripping dynamics of a drop depends on the properties of the surrounding medium. For example, the net force acting on the drop because of gravity ($(\rho_1 - \rho_2)gV_d$) depends on the density contrast between the drop and the surrounding fluid. Figure 3.10 shows the variation of aspect ratio of the drop at the incipience of pinch-off for different values of density ratio ρ_r. It can be seen in Fig. 3.10 that the aspect ratio of the drop at the incipience of pinch-off remains nearly constant over a wide range for lower values of ρ_r (when $\rho_r < 0.2$). This is because, the shear stress distribution inside the drop is affected very little by the density of the surrounding fluid. However, with increase in ρ_r the buoyant force acting on the drop surface in the upward direction becomes significant which affects the stress distribution inside the drop. As a result the aspect ratio of the drop at the time of pinch-off increases as evident in Fig. 3.10. The volume of the resulting drop increases with the increase in density ratio, because the apparent weight of the drop decreases with increased values of the density ratio, and in accordance with Tate's law [31], the drop volume increases to balance the gravity force with the surface tension force.

Figure 3.11 shows the aspect ratio variation of the drop at the incipience of

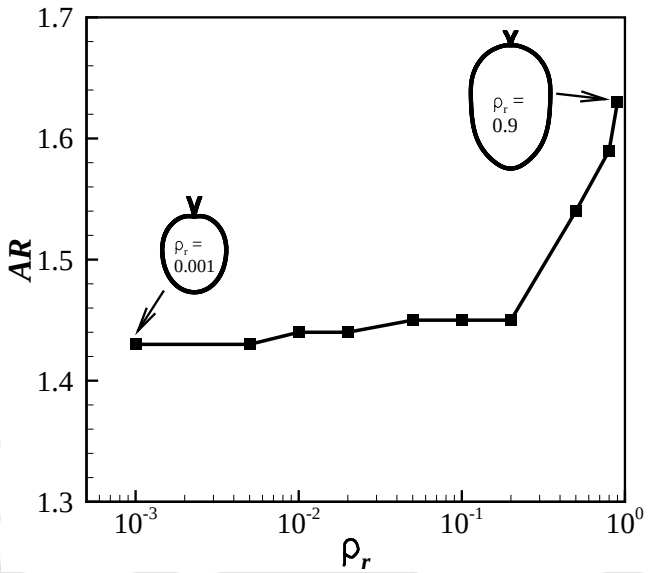

Figure 3.10: The aspect ratio (AR) of the drop at the incipience of pinch-off is plotted at different values of ρ_r. The other dimensionless parameters are $We = 0.57$, $Bo = 0.18$, $Oh = 0.0035$ and $\mu_r = 0.02$.

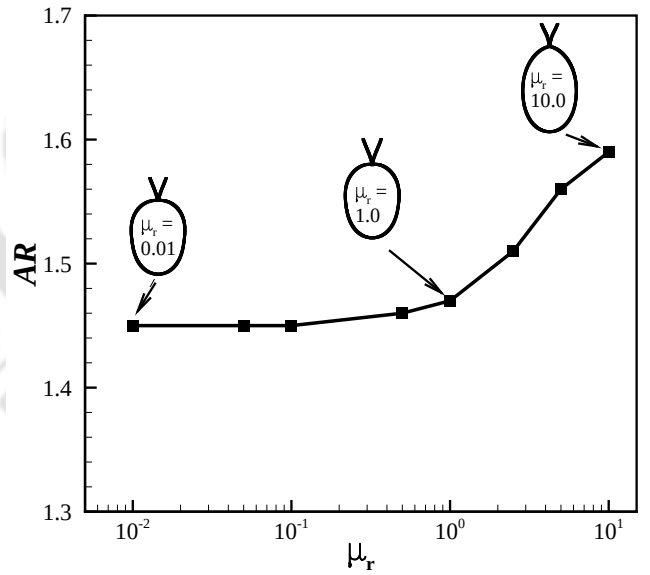

Figure 3.11: The aspect ratio (AR) of the drop at the incipience of pinch-off is plotted at different values of μ_r. The other dimensionless parameters are $We = 0.57$, $Bo = 0.18$, $Oh = 0.0035$ and $\rho_r = 0.00118$.

pinch-off for different values of viscosity ratio. It has been observed that the aspect ratio variation is very small when $\mu_r < 1$, even for two order of magnitude variation

of μ_r. This is because, when the surrounding fluid viscosity is much smaller than the drop fluid the stress distribution inside the drop is governed by the viscosity of the drop fluid. The effect of the surrounding fluid viscosity becomes negligible in such a situation. However, when the value of μ_r becomes close to unity or higher, the effect of surrounding fluid viscosity becomes significant in the shear stress distribution inside the drop. Although the We value is considerably small for transition to jetting, the interaction with the surrounding medium can no longer be neglected, owing to the predominant effects of aerodynamic drag and friction. As a result, the drop undergoes more deformation and assumes a more prolate shape. It has the reverse effect as that of increased viscosity of the drop fluid (effect of Oh discussed above), as increased viscosity ratio makes the drop more deformed with the increase in AR during pinch-off as evident in Fig. 3.11.

3.4.4 Oscillation of drop after pinch-off

After pinch-off, a drop falls through the surrounding medium under the action of gravity. During the translation of the drop through the surrounding fluid, the drag force exerted by the boundary layer developed around the drop and the vortex shedding may deform its shape depending on the strength of the surface tension force. When the shape of the drop is not spherical, local capillary pressure develops across the interface of the drop. The drop tries to minimize its surface energy and balance this capillary pressure by assuming a spherical shape. However, the fluid inertia does not allow it to attain the spherical shape directly. While a prolate shaped drop tends to become spherical to minimize its surface energy, the fluid inertia converts it into an oblate shape. The drop then again tends to become spherical, and the inertia converts it into prolate. Thus a prolate-oblate-prolate oscillation is initiated. The variation of the shape of a drop while falling through a surrounding medium is shown in Fig. 3.12. The instantaneous shapes of a water drop at different time instants after pinch-off are shown in Fig. 3.12(a). The surrounding medium is air and the dimensionless parameters are $We = 6.15 \times 10^{-7}$, $Bo = 0.0895$, $Oh = 0.00423$, $\rho_r = 0.00118$ and $\mu_r = 0.02$. It can be seen in Fig. 3.12(a) that the shape of the drop continuously varies with time between the prolate and oblate shapes. The variation of aspect ratio of the drop with time is presented in Fig. 3.12(b). The oscillatory motion of the drop is damped by viscosity.

Agrawal et al. [69] reported that an initially non-spherical drop undergoes prolate-

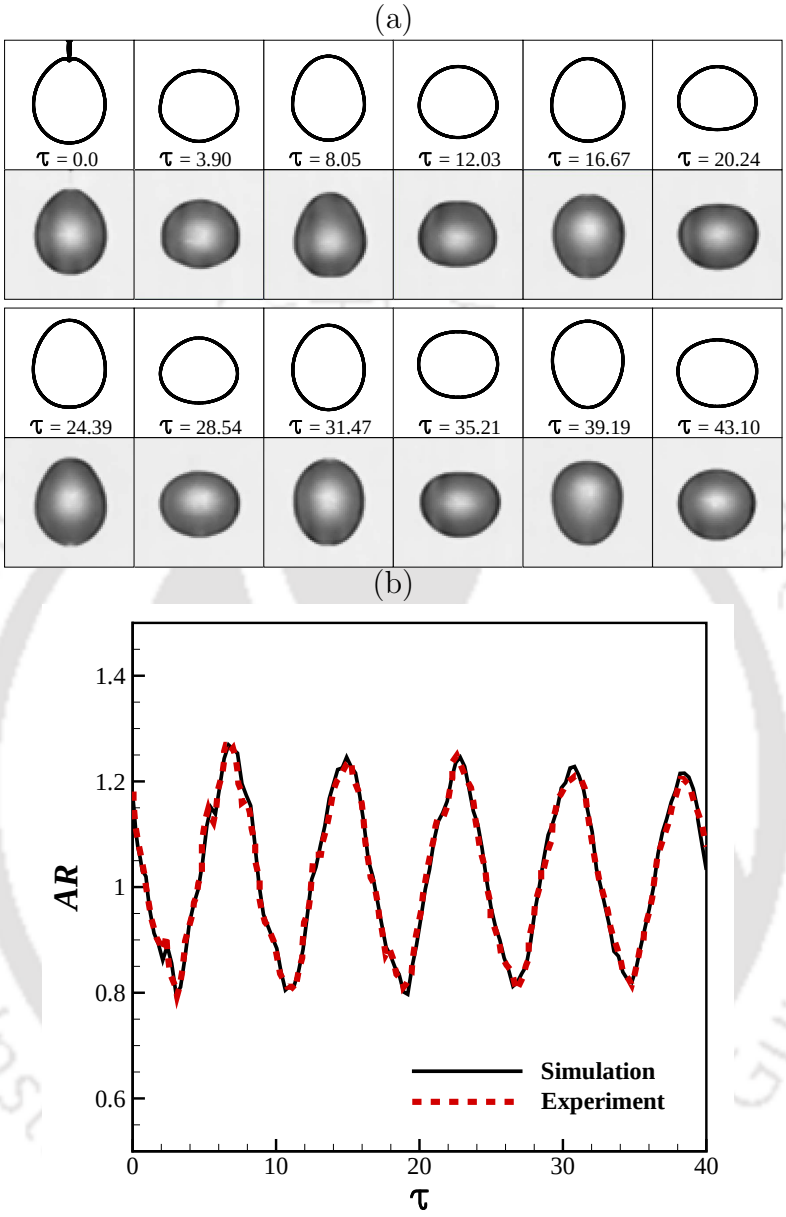

Figure 3.12: (a) Instantaneous shapes of a water drop at different time instants after pinch-off. The numerical results are presented in the first and third row. The experimental photographs of Tsai and Wang [73] at the same time instants are presented in the second and fourth row. The drop oscillates between the prolate and oblate shapes while falling through the surrounding medium. (b) The temporal variation of aspect ratio of the water drop while falling through the surrounding medium. The black solid line represent the results obtained from simulations and the dashed red line represent the experimental results [73]. The dimensionless parameters are $We = 6.15 \times 10^{-7}$, $Bo = 0.0895$, $Oh = 0.00423$, $\rho_r = 0.00118$ and $\mu_r = 0.02$.

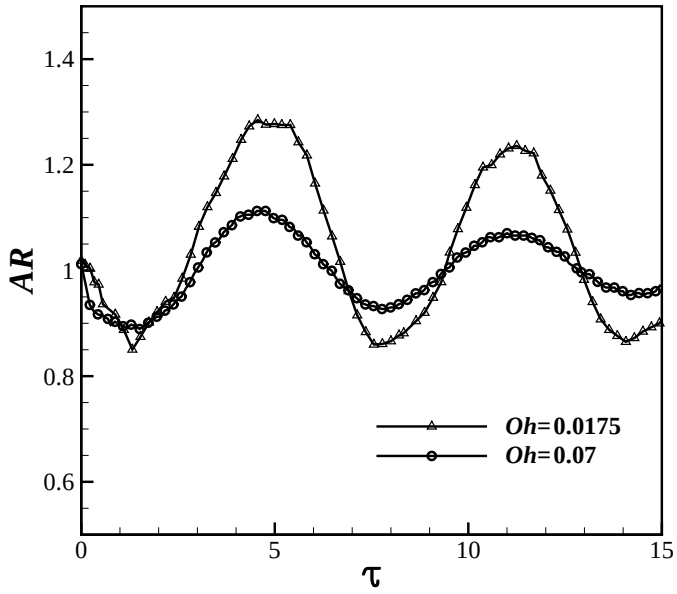

Figure 3.13: The temporal variation of aspect ratio of drops that are almost spherical ($AR \approx 1.0$) at the incipience of pinch-off. The dimensionless parameters are $We = 0.1$, $Bo = 0.18$, $\rho_r = 0.00118$ and $\mu_r = 9.25 \times 10^{-4}$ and 4×10^{-3}.

oblate-prolate oscillation while falling through a surrounding medium. They observed no such oscillation when they initialized the drop with spherical shape in their numerical simulations. Therefore, the question is "Does a drop which is spherical at the time of pinch-off show the same oscillating behavior ?" It is expected that a drop that is spherical (or almost spherical) does not undergo such oscillations. However, contrary to intuitive expectations our investigation reveals that a drop which is spherical at the incipience of pinch-off does undergo prolate-oblate-prolate oscillations. It can be seen in Fig. 3.13 which shows the oscillation of two drops which are almost spherical at the incipience of pinch-off. It has been observed that the vertical pull generated near the pinching region at the time of pinch-off deforms the drop after pinch-off and initiates the oscillation. During necking, the neck moves in the radially inward direction and merges at the axis of symmetry leading to pinch-off. The neck retraction is a fast process. The neck region rapidly elongates and becomes thin which finally leads to pinch-off. The rapid movement of the neck can be seen in the $u-$velocity contour and the $v-$velocity contour demonstrated in Fig. 3.14. As depicted in Fig. 3.14, a strong inward horizontal momentum and a downward vertical momentum act on the fluid near the pinching region at the time of pinch-off identified by the fast movement of the neck. After pinch-off,

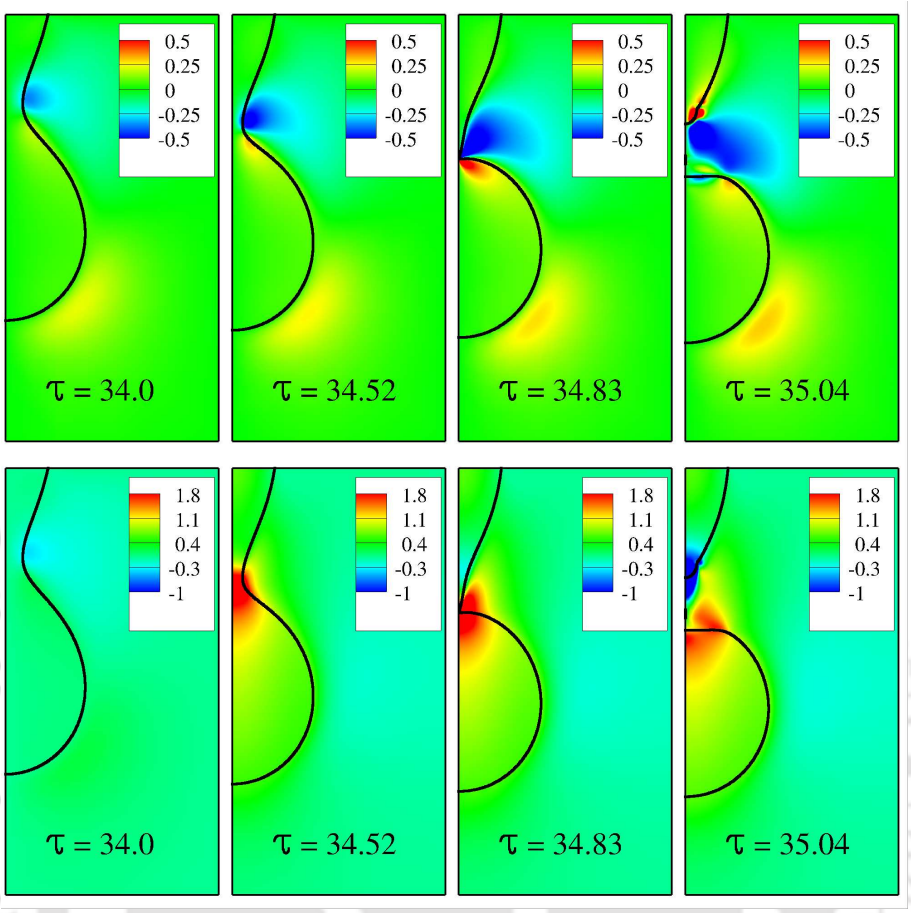

Figure 3.14: The interface profiles along with the velocity contour at shown at different instants of time before and after pinch-off. The $u-$velocity contours at different time instants along with the interface profiles are presented in the first row. The second row shows the $v-$velocity contour along with the interface profiles at the same time instants. The other dimensionless parameters are $We = 0.1$, $Bo = 0.18$, $Oh = 0.0175$, $\rho_r = 0.00118$ and $\mu_r = 0.004$.

the vertical momentum is transferred to the detached drop which acts on the fluid near the pinching region. Moreover, the horizontal momentum which acts on the neck during its inward movement also converts into vertical momentum during the merger of the neck at the axis of symmetry. Because of the induced vertical momentum, the drop fluid near the pinching region moves in the downward direction and deforms the drop leading to an oblate shape. The phenomenon is similar to the merging of the liquid tongue during large bubble entrapment where the horizontal momentum of the liquid tongue is converted into vertical momentum during pinch-off and initiates the inward and outward jets [53]. It can be seen in Fig. 3.14 that

the drop, during pinch-off, is almost spherical and becomes oblate after pinch-off because of the imparted vertical momentum during pinch-off. The deformed drop then tries to become spherical to minimize its surface energy and thus undergoes prolate-oblate-prolate oscillation.

The deformation of the drop after pinch-off depends on the magnitude of the vertical momentum generated during the pinch-off. For a highly viscous drop, viscosity damps the inward movement of the neck. As a result, the vertical momentum generated during pinch-off is also less. The viscosity also damps out the induced vertical momentum and resists deformation. Because of that the oscillation amplitude is less for a highly viscous drop as seen in Fig. 3.13 (for $Oh = 0.07$). For a low viscosity drop the pinch-off is fast and the vertical pull is higher. This causes higher deformation after pinch-off and a high amplitude prolate-oblate-prolate oscillation is observed as shown in Fig. 3.13 (for $Oh = 0.0175$).

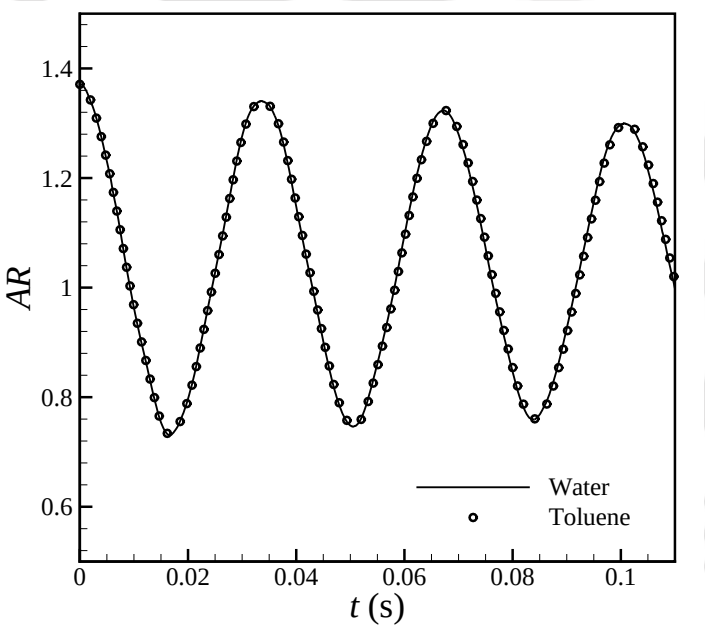

Figure 3.15: Comparison of temporal variation of aspect ratio of two ideal drops of water ($\rho = 998$ kg/m^3, $\mu = 1$ cP) and toluene ($\rho = 862$ kg/m^3, $\mu = 0.62$ cP) formed through a orifice of 1.2 mm radius. The drop volumes are calculated based on Tate's law and are initialized with $AR = 1.37$. The surrounding fluid is air ($\sigma = 70.0 \times 10^{-3}$ N/m for water and $\sigma = 28.5 \times 10^{-3}$ N/m for toluene).

A theoretical explanation of the oscillating behavior of drops can be drawn from Rayleigh's theory. The frequency of oscillation was derived by Lord Rayleigh [74] for

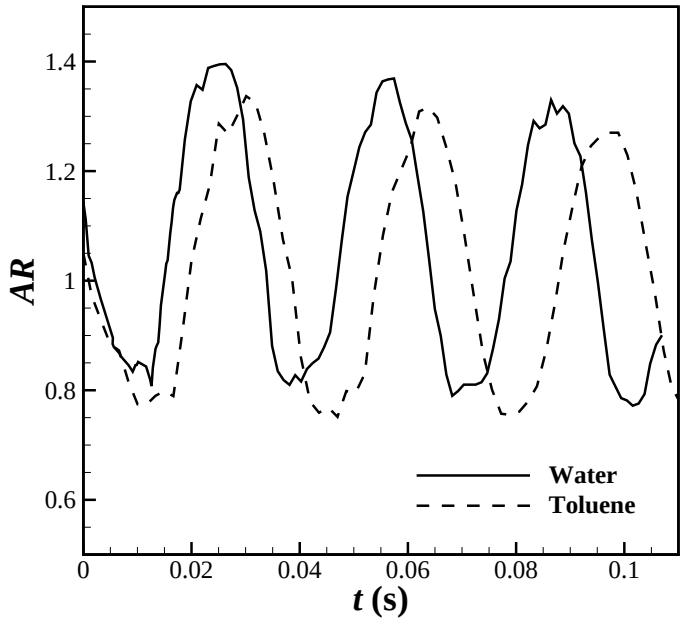

Figure 3.16: Comparison of temporal variation of aspect ratio water and toluene drops formed through a orifice of 1.2 mm radius. The surrounding fluid is air. The corresponding dimensionless parameter for water are $We = 0.2$, $Bo = 0.2$, $Oh = 0.003455$, $\rho_r = 0.00118$ and $\mu_r = 0.02$ and for toluene are $We = 0.2$, $Bo = 0.43$, $Oh = 0.0038$, $\rho_r = 0.00115$ and $\mu_r = 0.032$ respectively.

different modes of vibration using the linear theory in the inviscid limit. Following his derivation, the frequency of oscillations for this mode can be represented as [69] $f = \sqrt{2\sigma/\pi^2\rho_1 R_d^3}$, where R_d is the radius of the drop. Following Tate's law, R_d may be replaced by orifice radius R using the relation

$$V_i = \frac{4\pi R_d^3}{3} = \frac{2\pi R\sigma}{\rho g}. \tag{3.7}$$

Here, V_i is the ideal drop volume predicted by Tate's law. Replacing the value of R_d, the frequency of the oscillations can be represented as, $f = \sqrt{4g/3\pi^2 R}$. Thus, Rayleigh's analysis reveals that the frequency of oscillation of the drops depends on the orifice radius only, not on the fluid properties. In order to verify the oscillating behavior of ideal drops we considered two ideal drops of water ($\rho = 998$ kg/m^3, $\mu =$ 1 cP) and toluene ($\rho = 862$ kg/m^3, $\mu = 0.62$ cP) whose volumes are calculated based on Tate's law (Eq. 3.7). The drops are initialized with $AR = 1.37$. The oscillating behavior of the two ideal drops is shown in Fig. 3.15. The frequency of oscillation

of the two drops is the same, thus verifying the theoretical prediction of Rayleigh that the oscillating frequency of drops of different fluids formed through an orifice remains the same. However, the actual volume of the drop formed through an orifice is always less than the ideal volume predicted by Tate' law and can be determined from the experimental master curve given by Harkins and Brown [23]. The master curve is a plot of the fraction of the ideal drop volume, $\psi \equiv V_a/V_i$, as a function of the dimensionless orifice radius, $\phi \equiv R/V_a^{1/3}$, which is popularly known as HB curve. Here, V_a is the actual drop volume. As a result, the frequency of oscillation of a real drop formed through a nozzle differs from that of an ideal drop based on the correction factor of HB curve. This can be seen in Fig. 3.16 which shows the oscillation of two different drops of water and toluene formed through an orifice of 1.2 mm radius.

3.5 Summary

In this study, drop formation process from an orifice in the dripping regime has been investigated with an emphasis on the shape of the drop during pinch-off. The relative effects of inertial, capillary, viscous, and gravitational forces on the shape of the resulting drop during pinch-off have been investigated in detail. The shape of a drop at the incipience of pinch-off depends on the shear stress distribution within the drop. A non-spherical drop undergoes prolate-oblate-prolate oscillation while falling through a surrounding medium. The vertical pull generated near the pinching region at the time of pinch-off deforms the shape of the drop after pinch-off and initiates the oscillation.

Chapter 4

The regime of large bubble entrapment during a single drop impact on a liquid pool

4.1 Introduction

The aeration process is studied for centuries because of its importance in a wide variety of industrial applications and natural phenomena. The complex nature of the phenomena has made the researchers enthusiastic to explore the exact physics of the bubble entrapment process. The literature reveals that the bubble entrapment owing to the impact of a liquid drop onto a liquid pool may take place mainly in two ways, firstly owing to the closure of the mouth of the crater formed on the liquid pool caused by the impacting of drop, and secondly due to the rupture of the air film trapped near the bottom surface of the drop. During the regular bubble entrainment, the bubble pinches off at the bottom of the crater during the crater collapse. Pumphrey and Elmore [75] identified different regimes of bubble entrapment in the drop diameter(D)-impact velocity(V) plane as showed in Fig. 4.1(a). They also showed that bubble entrapment had an upper limit and a lower limit on the Weber number ($We = \rho V^2 D/\sigma$)-Froude number ($Fr = V^2/gD$) plane (Fig. 4.1(b)). The

The contents of this chapter have been published as an article entitled "The regime of large bubble entrapment during a single drop impact on a liquid pool", *Physics of Fluids*, 2017, vol. **29**(9), p. 092101.

upper bound and the lower bound of this region was determined by Oguz and Prosperetti [76] as $We_u = 48.3Fr^{0.247}$ and $We_l = 41.3Fr^{0.179}$ respectively. Rien et al. [77] reported that the regular bubble entrapment is always accompanied by the formation of a narrow high rising liquid jet. The bubble entrapment can be suppressed by the disturbances. Leng [78] reported that the regular bubble entrapment regime was a subset of high-speed jet formation regime, where he determined the upper limit for high-speed jet formation as $We = 54Fr^{0.25}$, beyond which thick jet was formed. Later the jet characteristics were widely studied [4, 79] and it was observed that the capillary wave motion and the pressure difference across the crater wall drive the phenomena. Such high-speed jets are observed in many other hydrodynamic situations like surface wave collapse [80], collapse of surface voids [81, 82], and bubble bursting at free surface [83] including inward jet formation [53, 82]. Deng et al. [84] investigated the effect of viscosity and surface tension on bubble entrapment owing to the drop impact. They observed that the entrapped bubble size decreased with the increase in capillary number ($Ca = \mu V/\sigma$), and estimated the cut-off limit of capillary number for bubble entrapment to be around 0.6. The bubble entrapment takes place due to capillary pinch-off before the crater reversal. Surface tension is the main driving force of the capillary ripples and increased viscosity dampens the capillary ripples. However, the increased viscosity also increases the damping effect on crater cusp reversal leading to an increase in the upper limit of regular bubble entrapment region [84, 85].

On the traditional classification map, the large bubble entrapment occurs over a small region as shown in Fig. 4.1(a). In this process, the crater produced by the drop impact expands radially and closes at the top to entrap a large bubble. Zou et al. [70] studied the effect of surrounding wall on large bubble entrapment and observed that the bubble entrapment on drop impact depended on drop shape and the distance of the impact point from the surrounding wall, in addition to drop diameter and impact velocity. The observations also include that the large bubble entrapment can be enhanced by impacting a liquid drop on a constricted liquid pool. The region of large bubble entrapment was not continuous, rather scattered over some discrete range. The appearance of large bubble entrapment was periodical with respect to the falling time. The periodic appearance of large bubble entrapment was attributed to the shape oscillation of the falling drop. As described in Sec. 3.1, the drop shape is defined in terms of aspect ratio (AR) which is the ratio of axial and radial axis lengths of the drop. Based on AR, we may get three different shapes

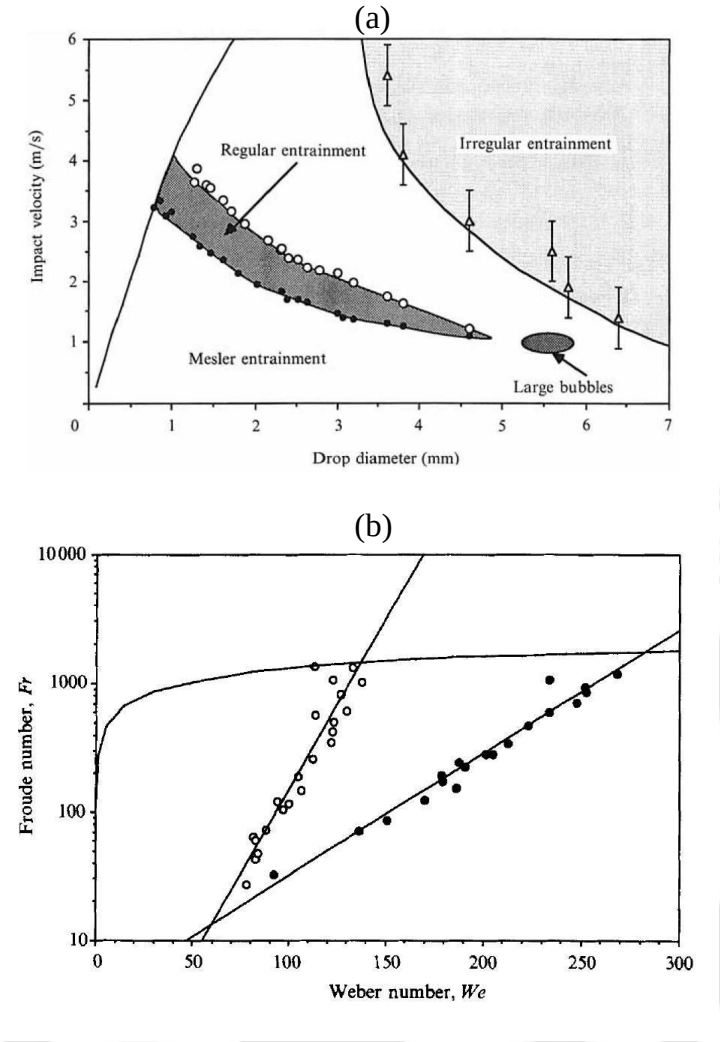

Figure 4.1: Bubble entrapment regimes on the traditional classification map [75] in (a) Drop diameter (D)-Impact velocity (V) plane, (b) Weber number (We)-Froude number (Fr) plane. In the We-Fr plot the vertical axis is in logarithmic scale while the horizontal axis is linear.

of the drop, namely prolate (AR >1), spherical ($AR = 1$) and oblate (AR <1). The shape oscillation of drop is periodical with the falling time [52]. The large bubble entrapment takes place only when the prolate shaped drop impacts onto a liquid pool. The volume of the entrapped bubble can be much larger than the drop itself.

Wang et al. [52] investigated the different bubble entrapment process during drop impact on a liquid pool. Form their experimental observations they reported that large bubble entrapment also takes place outside the small region of the traditional V-D map (Fig. 4.1(a)). This new finding raised two questions in the mind of the

researchers. The first question is, "How does the large bubble entrapment take place?", and the second question is, "What is the exact boundary of large bubble entrapment regime?". Later, Thoraval et al. [53] reported that the entrapment of large bubble is a vortex driven phenomena. The vortex ring produced during the drop impact controls the crater deformation and the pinch-off. For a flatter oblate drop, on impact to the pool surface, the neck shape forms a sharper cusp than for a spherical or prolate drop. Sharper curvature produces stronger vorticity. The strong vortex starts to pull on the interface before it fully enters the pool. This results in a thin and more vertical liquid protrusion, which is rapidly pulled back by surface tension. Whereas for a prolate drop, vortex pulls on the interface below the pool surface, on the side of the cavity created by the impacting drop. This makes the thicker and more horizontal liquid protrusion, which then collapses on the central axis to entrap the large bubble. However, the boundary of large bubble entrapment regime is still unexplored, which motivated us to study these complex phenomena again.

The present study mainly focuses on the mechanism of large bubble entrapment and determination of the boundary for the large bubble entrapment regime. The factors responsible for large bubble entrapment have been explored. The morphology of the entrapped large bubble has been discussed. Further, how the change of impact condition changes the crater morphology within the large bubble entrapment regime has been discussed. Two basic dimensionless numbers are used, Weber number ($We = \rho V^2 D/\sigma$) and Froude number ($Fr = V^2/gD$). Our results represent an air-water system with constant temperature.

4.2 Formulation

4.2.1 Computational domain

A representative diagram of the computational domain is shown in Fig. 4.2. An axisymmetric coordinate system (r, z) is used to model the flow dynamics, where r and z represent the radial and axial coordinates, respectively. The drop is initialized just above the liquid pool ($\approx$ 0.1D) with its impact velocity V along the negative $z-$direction. The drop and the pool are of same liquid (Fluid 1). Considering the axisymmetric assumption, the equivalent diameter of the drop is calculated as $D = (a^2 b)^{1/3}$, where a and b are the horizontal and vertical diameters (axis lengths) of the

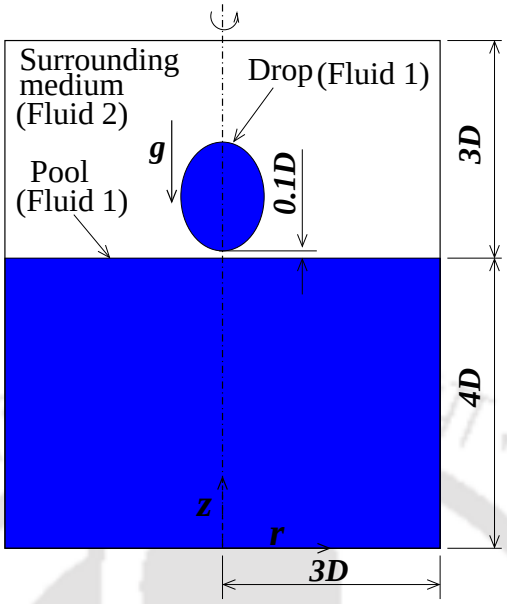

Figure 4.2: Computational domain for impact of a liquid drop on a liquid pool. A drop of equivalent diameter D is initialized just above the liquid pool ($\approx$ 0.1D) with its impact velocity V along the negative $z-$direction. The computational domain has a width of $3D$ and a height of $7D$ having pool depth $4D$.

drop. The relation between a and b can be found out from volume conservation [53] as $\tilde{b} = 1/\tilde{a}^2$, where $\tilde{a} = a/D$ and $\tilde{b} = b/D$, respectively. The domain has a width $3D$ and height $7D$ with pool depth $4D$ as shown in Fig. 4.2.

4.2.2 Boundary conditions

In the computational domain we have performed axisymmetric simulations and the axis of symmetry lies on the left boundary. At the axis of symmetry no fluid exits or enters the domain. This can be mathematically expressed in terms of the velocity components (u, v) along the $r-$ and $z-$directions as

$$u = 0, \frac{\partial v}{\partial r} = 0. \tag{4.1}$$

The same boundary conditions can be applied on the right boundary as the right boundary is considered to be frictionless. On the bottom wall we deploy the no-slip boundary condition and the impermeability condition,

$$u = v = 0. \tag{4.2}$$

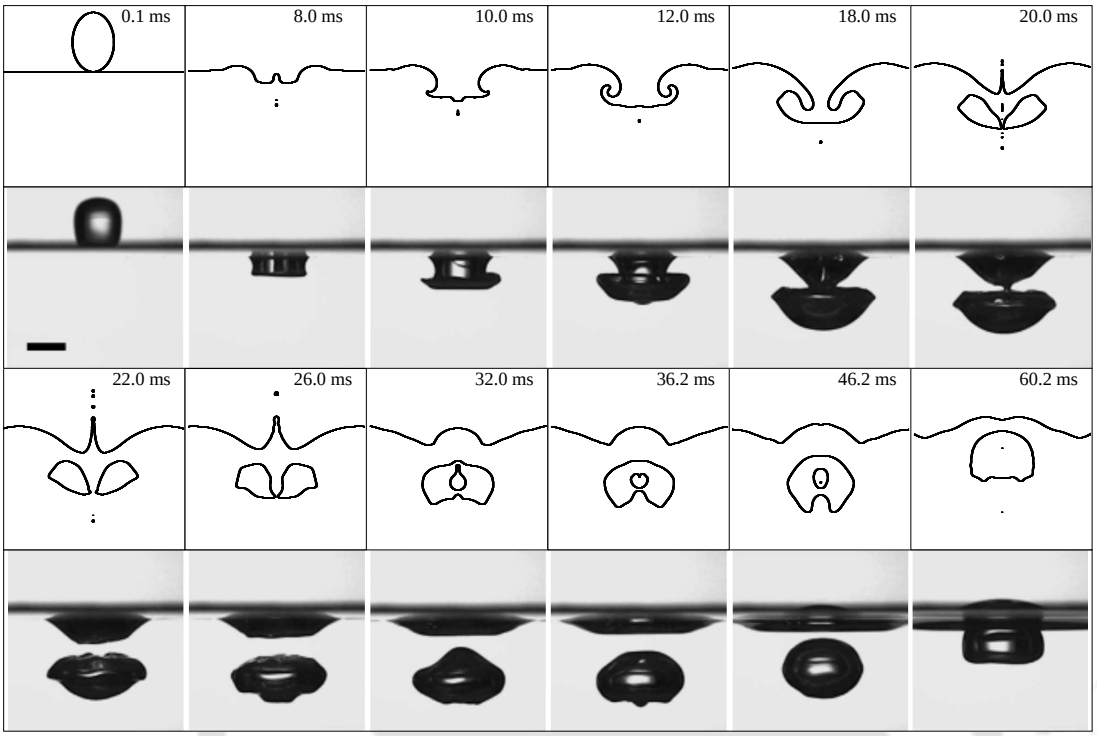

Figure 4.3: Comparison between the numerical results of present investigation and the experimental results of Wang et al. [52] for an impact of a 5.65 mm equivalent diameter drop at an impact velocity of 0.953 m/s. The drop and pool liquid is water and the surrounding is air. The contours at different time instants show the coalescence of the drop and the evolution of the large bubble. The other non-dimensional parameters are $We = 75$ and $Fr = 16$.

At the top boundary, the natural Neumann boundary condition is applicable given as

$$\frac{\partial u}{\partial z} = \frac{\partial v}{\partial z} = 0. \tag{4.3}$$

The Neumann pressure boundary condition is applied at all the boundaries except at the top boundary where pressure is equal to the atmospheric pressure P_{atm}.

4.3 Validation of numerical approach

The present simulations are validated with the experimental results of Wang et al. [52]. We have got good agreement with the experimental results as evident in

Fig. 4.3 and Fig. 4.4. Figure 4.3 is a typical case of large bubble entrapment (L regime). A new finding in the work of Wang et al. [52] is the generation of a bubble pair, i.e., generation of sequential large and small bubbles. In Fig. 4.4, our simulations support the case of large bubble together with a small bubble entrapment (L+S regime).

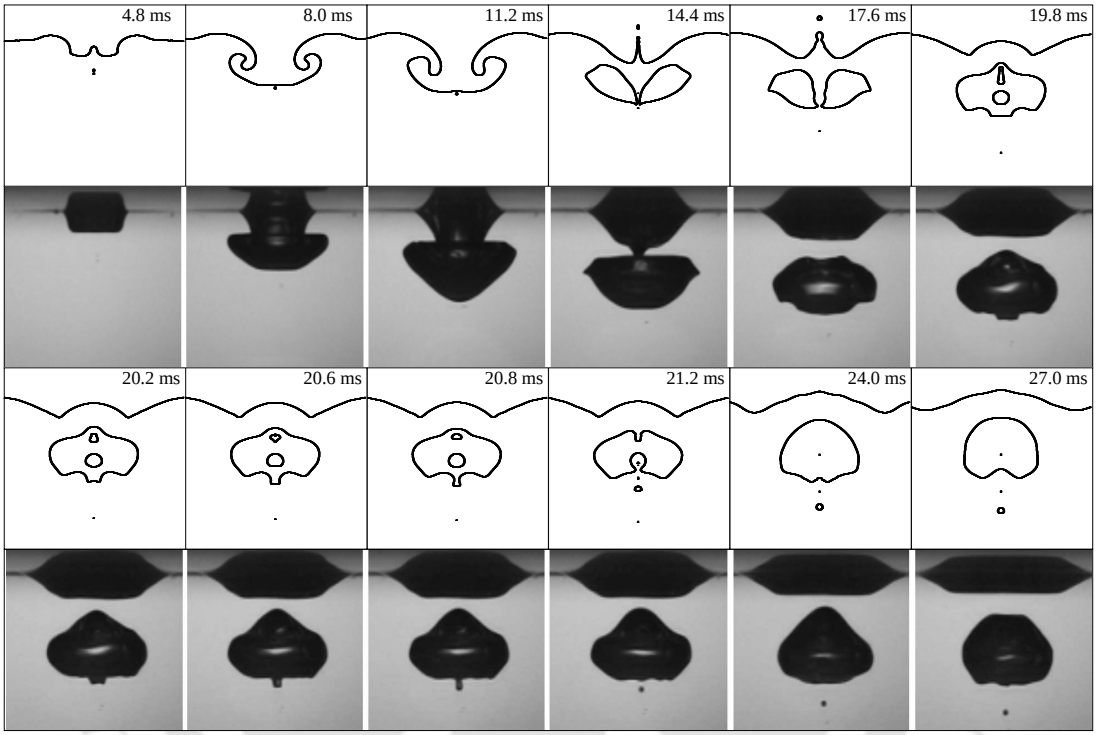

Figure 4.4: Comparison between the numerical results of present investigation and the experimental results of Wang et al. [52] for an impact of a 4.42 mm equivalent diameter drop at an impact velocity of 1.136 m/s. The drop liquid is water and the surrounding is air. The contours at different time instants show the coalescence of the drop and the evolution of the large bubble along with a small bubble. The other non-dimensional parameters are $We = 83$ and $Fr = 30$.

In order to undertake quantitative comparisons, we compared the experimental results and the numerical results for pinch-off time (τ_p) of the large bubble for different velocity (V) of the impacting drop. The non dimensional pinch-off time τ_p is defined as $\tau_p = t_p V/D$, where t_p is the actual pinch-off time. The pinch-off time t_p is the time taken from the instant the drop impacts on the pool interface to the instant pinch-off of the large bubble occurs. The equivalent diameter (D) of the impacting drop is 5.65 mm. The numerical and experimental results show an excellent match as depicted in Fig. 4.5. The pinch-off time decreases with the

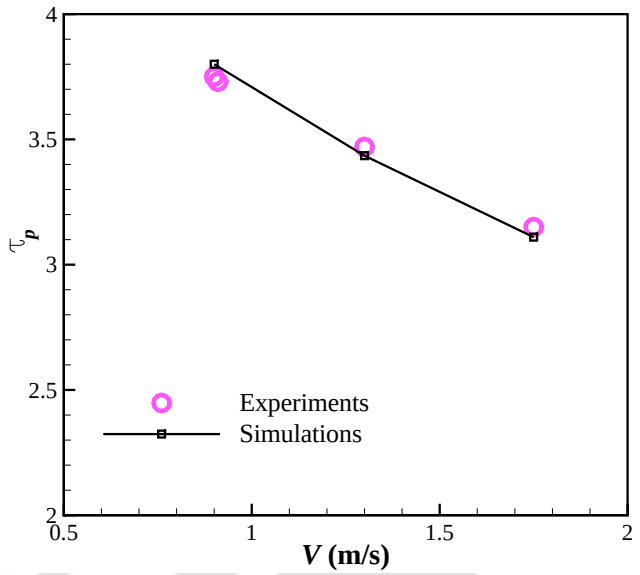

Figure 4.5: Comparison between the experimental results and the numerical results for the pinch-off time (τ_p) of the large bubble for different impact velocity (V). The equivalent diameter of the impacting drop is $D = 5.65$ mm. The drop liquid is water and the surrounding is air.

increase in impact velocity, which is consistent in both numerical and experimental observations.

Present simulations have been performed using a very refined grid. The computational domain has been divided into $2.5 \times 10^6 - 3.5 \times 10^6$ grid cells depending on the size of the drop. It was observed that a coarse grid could not capture the physics of the phenomena well. It can be seen in Fig. 4.6 that large bubble entrapment was not observed for 0.21 million grid cells for a drop of diameter 5.65 mm and impacting at a velocity of 0.953 m/s. However, when the grid is refined (3×10^6 grid cells) it is able to capture the large bubble entrapment well. The refined grid shows an excellent match with the experimental results as shown in Fig. 4.3.

4.4 Results and discussion

The entrapment of a large bubble on drop impact depends on three basic parameters, namely, impact velocity, drop diameter and the shape of the drop at the time of impact. The shape oscillation of the drop produces internal circulation within the drop. But these circulatory motions inside the drop are not a significant factor

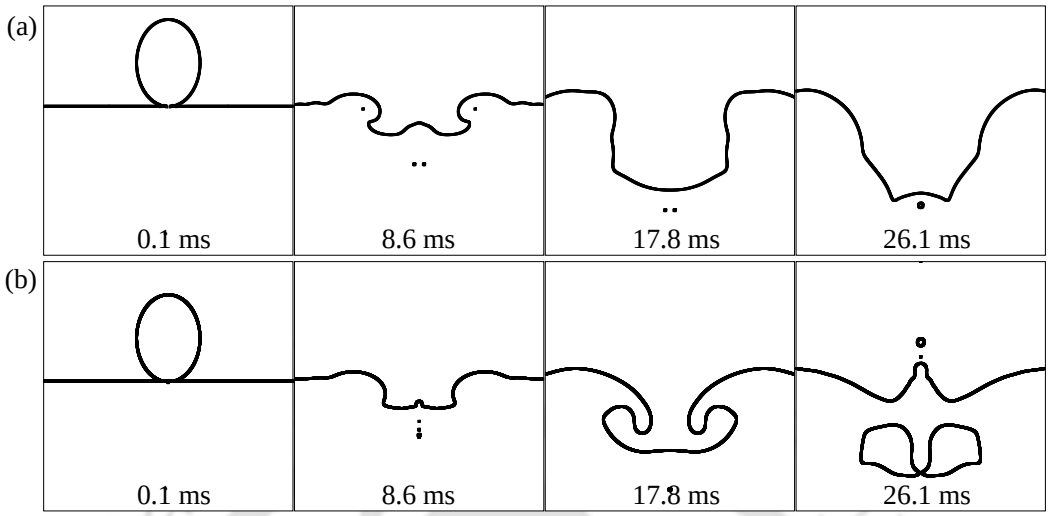

Figure 4.6: Comparison between the numerical results for two computational domain having (a) 0.21 million grid cells and (b) 3 million grid cells. The drop has an equivalent diameter of 5.65 mm and impact velocity of 0.953 m/s. The other non-dimensional parameters are $We = 75$ and $Fr = 16$.

during rapid impact motions [53]. The internal circulation serves the purpose of changing the shape of the drop. The shape of the drop at the time of impact is an important parameter in the subsequent dynamics.

4.4.1 Large bubble entrapment regime

According to traditional considerations two parameters control the bubble entrapment on drop impact onto a liquid pool, namely drop diameter (D) and impact velocity (V). On the traditional V-D map, the large bubble entrapment regime occupies a very small zone as shown in Fig. 4.1. The parameter that was missed on the traditional V-D map was the shape of the drop at the time of impact [52]. The shape of the drop at the time of impact has utmost importance in the process of entrapment of a large bubble. The different range of shapes, diameters, and velocities is difficult to obtain experimentally as the shape of the impacting drop cannot be controlled. A falling drop oscillates periodically in between prolate and oblate shapes, as it falls through the surrounding medium. To get a particular shape one needs to change the needle height from the pool surface, through which the drop forms. But this in turn also changes the impact velocity.

In our numerical simulations, we have tested for all the three shapes of the drop

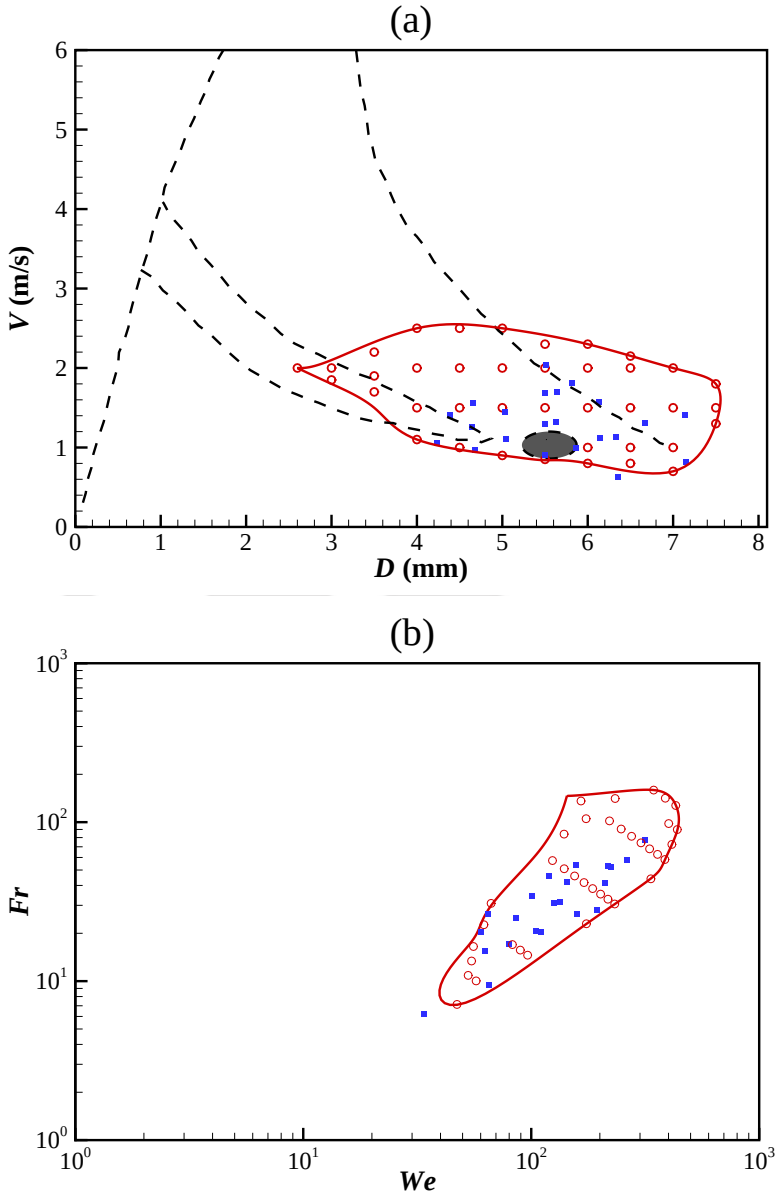

Figure 4.7: (a)The regime on the V-D map where the large bubble entrapment is observed (area bounded by the red line) is overlapped with the traditional V-D map (dashed lines), (b) the regime of large bubble entrapment on the We-Fr map. Outside this regime the large bubble entrapment has not been observed. The red circles represent the points of large bubble entrapment. The filled blue squares are the points where large bubble entrapment was observed experimentally by Wang et al. [52]. The filled gray region is the Large bubble entrapment region (L-regime) on the traditional V-D map as shown in Fig. 4.1.

i.e. prolate, oblate and spherical with the aspect ratio ranging from 0.7 to 1.4. The range of aspect ratio is selected based on experimental observations [52, 53], which suggest that the aspect ratio variation lies within this range. The large bubble entrapment has been observed only for the prolate shaped drops over a wider region on the V-D map as shown in Fig. 4.7(a). This is in contradiction to the small range that was identified earlier on the traditional V-D map. Outside this region no large bubble entrapment takes place. The same large bubble entrapment regime is plotted in We-Fr plane in Fig. 4.7(b).

In Fig. 4.7, the red circles represent the points where large bubble entrapment takes place. We performed nearly 200 simulations. All the points are not shown on the map in order to maintain clarity. The blue squares are the points where large bubble entrapment was observed experimentally by Wang et al. [52]. These squares lie inside the large bubble entrapment boundary found by our numerical simulations. The area bounded by the red lines is the region where large bubble entrapment was observed for the different diameters, impact velocities, and shapes of the drops. As seen in Fig. 4.7 this boundary is even well inside the irregular entrapment regime of the traditional V-D map. The large bubble is sometimes accompanied by the entrapment of a small bubble. The generation of sequential large and small bubbles depends on the characteristics of the crater formed by drop impact. Once the large bubble is formed, the bubble shape oscillates. In the case of a sequential bubble pair, a small bubble detaches from the bottom of the large bubble along the centerline. This small bubble is different from the regular small bubble entrapment and is also observed outside the regular entrapment regime of traditional V-D map.

4.4.2 Vortex ring and roll jet

The large bubble entrapment process is controlled by the vorticity generated during the impact of the drop onto the pool. The vorticity is generated at the free surface as it cannot be produced spontaneously within the pool by the impact [53]. The strength of the vorticity for a stationary two dimensional free surface was given by Batchelor [86] as

$$\Delta\omega = \frac{2q}{R_c}, \tag{4.4}$$

where $\Delta\omega$ is the vorticity produced by flow q having local radius of curvature R_c. The shape of the drop changes the strength and the dynamics of the vortex ring and

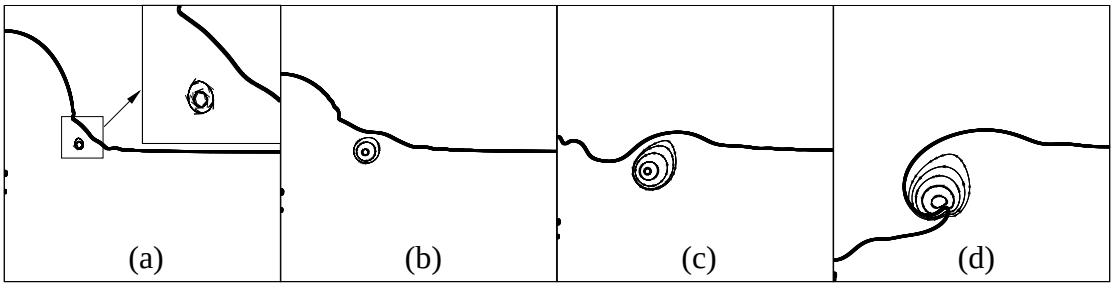

Figure 4.8: The coalescence of a drop of 4.42 mm diameter into a liquid pool at impact velocity of 1.136 m/s, showing the evolution of roll jet. The other dimensionless parameters are $We = 83$ and $Fr = 30$. The profiles (a), (b), (c) and (d) are at 1.69 ms, 2.73 ms, 4.3 ms and 6.86 ms respectively. The streamlines show the formation of the vortex ring. The vortex ring forms near the contact point of the drop and pool as seen in (a) with an enlarged view of the vortex in the corner. The ring then moves in the horizontal direction beneath the pool surface (b), which curl-up the liquid near the surface of the pool as evident in (c) to form the roll jet as seen in (d).

its interaction with the interface. Flatter drops produce stronger vortex ring and self-destruct early. For the prolate shaped drops, the vortex is weaker but moves deeper into the pool before pulling on the interface. This induces a stronger vortical flow away from the interface. The vortical flow then pulls the interface below the pool surface on the side of the cavity, generating a thicker liquid tongue, which merges to entrap the large bubble.

The pool liquid can rise along the side of the drop shedding vortices along its way [87, 88]. The vortex either remains attached or separates from the interface depending on the chosen physical parameters. The vortices originate at the corner, detach in the downward direction in the pool and then travel horizontally below the pool level [89]. The vortex ring curls-up the pool liquid near the surface and resurfaces it to form the roll jet. The roll jet then curves toward the center of the crater in the form of a liquid tongue. Figures 4.8, 4.9 and 4.10 show the formation and propagation of vortex ring at different time instants. The vortex is formed near the interface (Fig. 4.8(a)), which later separates out from the interface and moves into the pool creating a vortex ring. The vortex ring may be defined as a region of highly concentrated vorticity which lies along an internal azimuth of the ring forming a toroidal vortex tube [90]. The drop fluid pushes the vortex ring into the pool and the vortex ring moves downward and outward (Fig. 4.8(b)). The vortex ring produces circulation inside the pool. Due to the crater opening, when

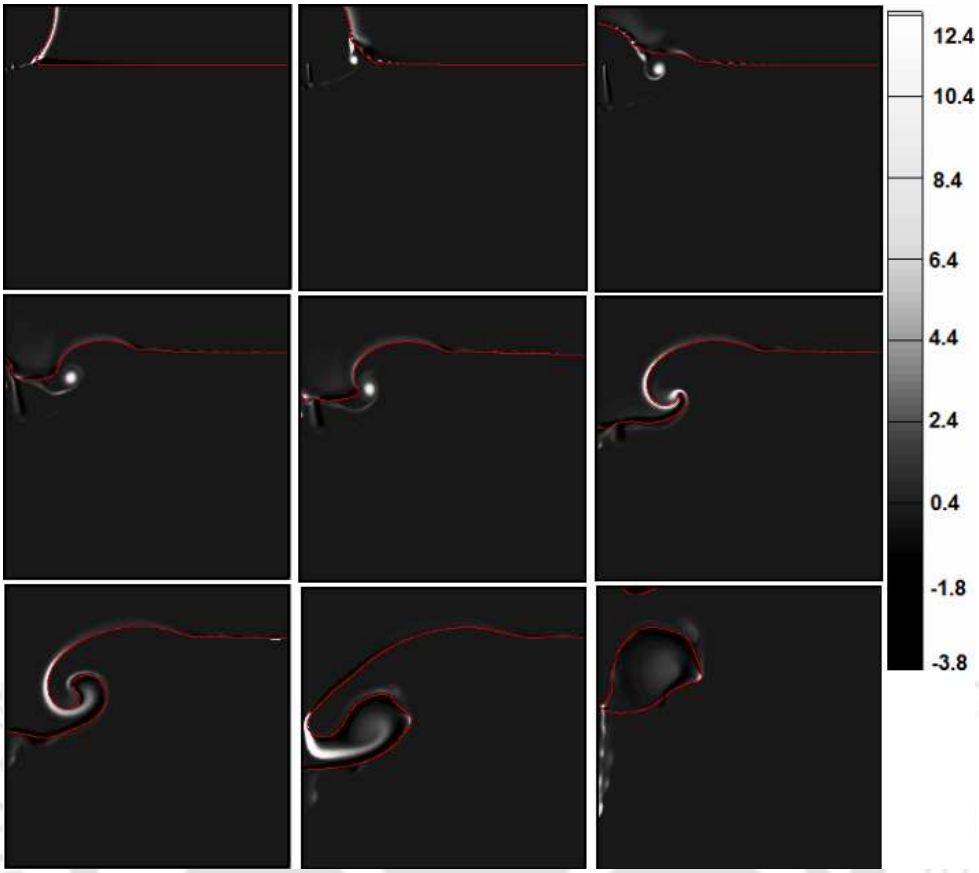

Figure 4.9: Vorticity contour showing the formation and propagation of vortex ring during large bubble formation due to the impact of a 5.65 mm equivalent diameter drop at an impact velocity of 0.953 m/s. The contour legends indicate vorticity values scaled down by a multiple of 10^{-3} from its values in SI unit. The profiles from left to right in first row: 0.5 ms, 2.43, and 4.79 ms; in second row: 7.6 ms, 8.83 ms, and10.6 ms; and third row: 13.6 ms, 18.8 ms, and 24.2 ms respectively. The other dimensionless parameters are $We = 75$ and $Fr = 16$. The last sub-figure is enlarged to show the vorticity contour below the bubble.

this vortex ring comes near the interface, the interface is pulled by the circulation produced within the pool (Fig. 4.8(c)). The circulation produced by the vortex ring thus curls-up the fluid near the interface to form a roll jet (Fig.4.8(d)). The vortex pulling also restricts the crater opening and crater penetration into the pool as it continuously pulls the interface sideways. It is seen that the vorticity in the necking region is strong during pinch-off. Comparing Fig. 4.9 and Fig. 4.10, it is seen that once the bubble is pinched off, a vortex roll up along the centerline stretching below the bubble.

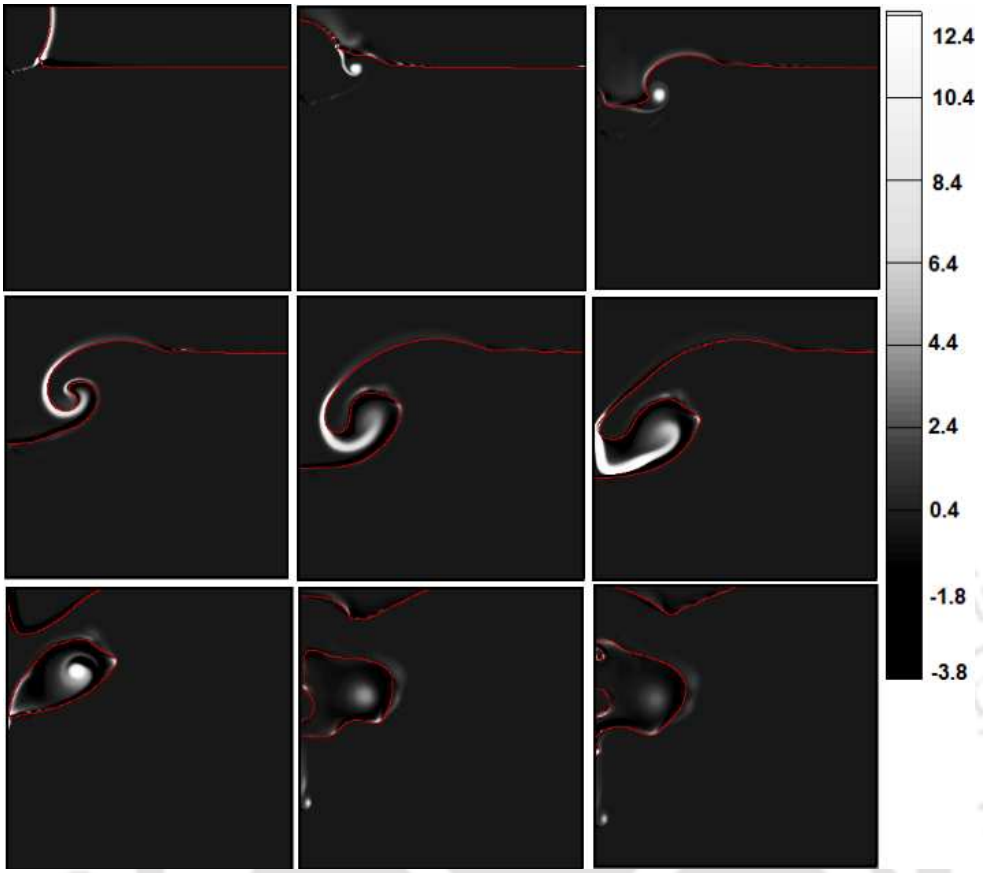

Figure 4.10: Vorticity contour showing the formation and propagation of vortex ring during sequential large and small bubble formation during the impact of a 4.42 mm equivalent diameter drop at an impact velocity of 1.136 m/s. The contour legends indicate vorticity values scaled down by a multiple of 10^{-3} from its values in SI unit. The profiles from left to right in first row: 0.5 ms, 2.84 ms, and 5.68 ms; in second row: 8.65 ms, 12.7 ms, and13.2 ms; and third row: 15.65 ms, 21.2 ms, and 24.5 ms respectively. The other non-dimensional parameters are $We = 83$ and $Fr = 30$. The last row sub-figures is enlarged to show the vorticity contour during the small bubble pinch-off.

4.4.3 Ejecta sheet and crater dynamics

Two separate liquid sheets, namely ejecta and lamella sheets are observed during the impact of a drop onto a liquid pool [91]. The ejecta is the inertia induced thin liquid sheet and the lamella is the capillary induced thick liquid sheet generated during the drop impact onto a liquid pool. The ejecta, if merged with the lamella, suppresses the vortex ring formation [92]. Under this condition, the vortex remains attached to the interface all the time and becomes progressively weaker.

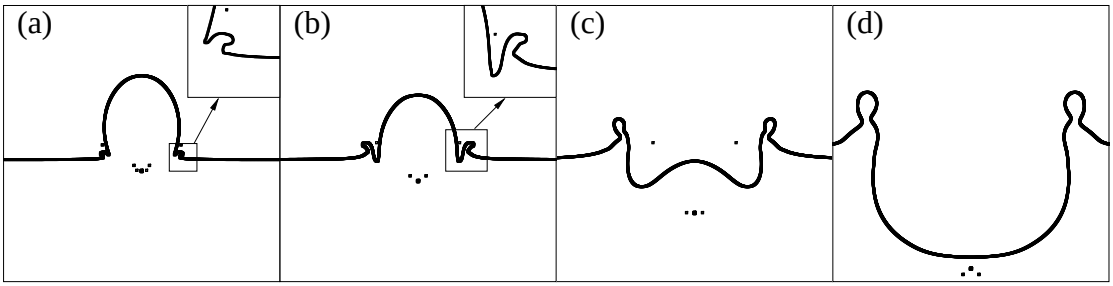

Figure 4.11: The evolution of the inertia induced ejecta sheet which leads to lamella due to the impact of a drop of 3 mm diameter into a liquid pool at an impact velocity of 2.8 m/s. The initial shape of the drop just before impact is prolate having aspect ratio $AR = 1.37$. The other non-dimensional parameters are $We = 324$ and $Fr = 266$. The liquid tongue curves away from the center line and no entrapment takes place. The profiles (a), (b), (c), (d) are at 0.25 ms, 0.61 ms, 1.378 ms and 3.4 ms, respectively.

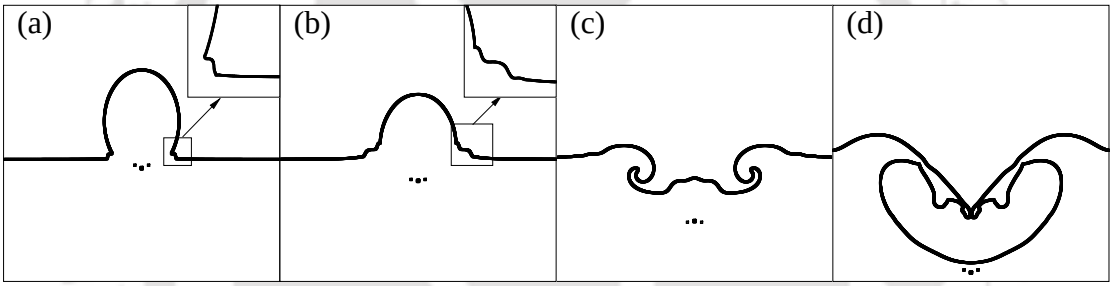

Figure 4.12: The coalescence of a drop of 3 mm diameter into a liquid pool at impact velocity 2 m/s without the evolution of ejecta sheet. The initial shape of the drop just before impact is prolate having aspect ratio $AR = 1.37$. The other non-dimensional parameters are $We = 165$ and $Fr = 140$. The liquid tongue curves towards the center to entrap bubble on merging. The profiles (a), (b), (c), (d) are at 0.25 ms, 0.685 ms, 2.22 ms and 4.54 ms, respectively.

The entrapment of a large bubble is restricted by the emergence of the ejecta sheet which leads to lamella. The emergence of the ejecta sheet depends on the impact velocity of the drop. The emergence of the ejecta sheet which merges with lamella pushes the liquid outward near the crater mouth resulting in a wider opening of the crater mouth. The pool liquid is forced outward resulting in a deeper and wider crater as shown in Fig. 4.11. Figure 4.12 shows the coalescence of a liquid drop onto a pool without the emergence of ejecta sheet. The non-emergence of ejecta sheet prevents the crater widening and contributes to the formation of roll jet.

It is clear from the simulation that the entrapment of the large bubble takes

place due to the merger of the liquid tongue formed by the roll jet. The roll jet is formed owing to the curled-up pool liquid induced by the vortex ring movement. If the vortex ring remains attached to the interface, the roll jet is not formed. Hence, large bubble entrapment is not observed when the vortex ring remains attached to the interface. In our numerical simulations, it is observed that vortex ring formation inside the liquid pool is prevented when the ejecta sheet merged with the lamella sheet emerges on drop impact. This makes the crater to move deeper and wider without the formation of roll jet.

The non-emergence of the ejecta sheet does not always imply consequential entrapment of the large bubble. Sometimes, the entrapment does not take place even if the ejecta sheet does not emerge on drop impact. The entrapment of the large bubble may be attributed to the merger of the liquid tongue, that is formed by the vortex ring. The strength of the vortex must be strong enough, so that it overcomes the surface tension driven pull and forms an elongated roll jet that merges at the center line, for the entrapment of large bubble. If the vortex strength is not sufficiently strong, the roll jet, although emerges, is unable to meet at the centerline and hence large bubble entrapment is not brought about. This is illustrated in Fig. 4.13 ((b_1)-(b_4)). Here for a spherical drop of 5 mm diameter with an impact velocity of 1 m/s, albeit the emergence of a roll jet, it is not sufficiently elongated and is pulled back by the surface tension without having merged at the central axis.

For an oblate shaped drop, the vortex remains attached to the interface and continuously pulls the interface which decreases its strength as shown in Fig. 4.14. The vortex ring does not separate out from the interface to form the roll jet. Although a strong vorticity is produced owing to the sharper cusp in the neck for the oblate shaped drop, it is not able to move deeper into the pool to form the roll jet. As depicted in Fig. 4.13, for the oblate shaped drop the pool liquid is not able to move along the side of the drop, unlike the prolate shaped drops, where the pool liquid rises along the side of the drop pushing the vortex ring into the pool. For the prolate shaped drop, the vortex ring thus moves deep into the pool away from the interface. Chapman and Critchlow [93] reported that a spherical drop about to become prolate, on impact correlates deeper penetration of the vortex ring. However, their observations were in disagreement with the observations of Kutter [94]. Later on, with the advancement of high-speed photography, it was observed that most penetrating vortex ring was produced by a prolate shaped drop [95]. Current investigation also confirms that a prolate shaped drop upon impact culminates in

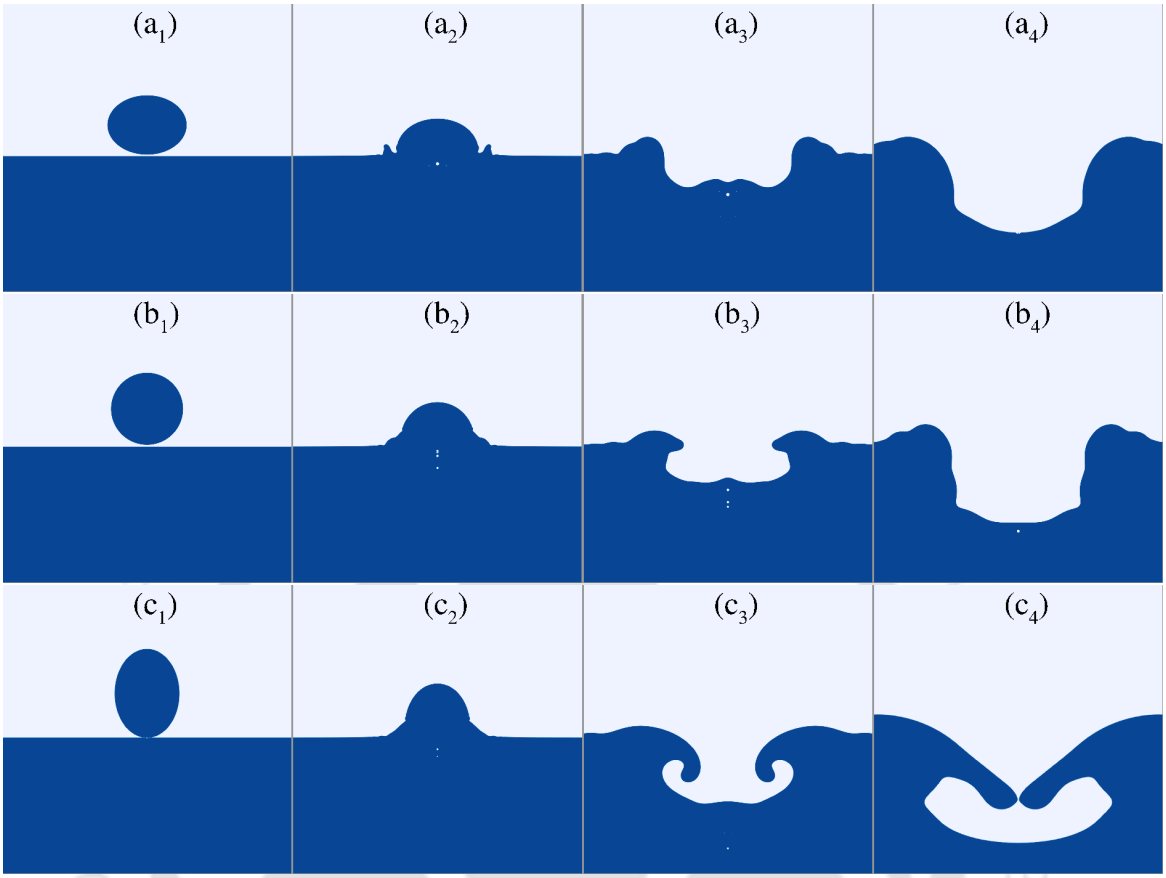

Figure 4.13: The evolution of the crater profile on coalescence of a drop of 5 mm diameter into a liquid pool at impact velocity 1 m/s. The first row ((a_1)-(a_4)) is for an oblate shaped drop ($AR = 0.75$), the second row ((b_1)-(b_4)) is for a spherical drop ($AR = 1$) and the third row ((c_1)-(c_4)) is for a prolate shaped drop ($AR = 1.37$). The other parameters are $We = 69$ and $Fr = 20.4$. The profiles (a_1)-(a_4) correspond to time 0.01 ms, 0.55 ms, 5.3 ms and 14.5 ms respectively. Similarly profile (b_1)-(b_4) correspond to time 0.01 ms, 0.55 ms, 5.3 ms and 14.5 ms respectively and (c_1)-(c_4) correspond to time 0.01 ms, 0.55 ms, 8.65 ms and 16.5 ms, respectively.

deeper penetration of vortex ring. The vortex ring then generates a vortical flow away from the interface. Later when the interface comes close to the vortex due to the crater opening, it pulls and deforms the interface to form the roll jet. Stronger vortical flow produces a more elongated roll jet. The roll jet is pulled by the surface tension force that merges above the crater leading to large bubble entrapment.

The strength of the vortex ring depends on the penetration of the vortex into the pool. With the decrease in aspect ratio, the penetration of the vortex into the pool decreases. If the penetration is less, then the interaction of the vortex with the

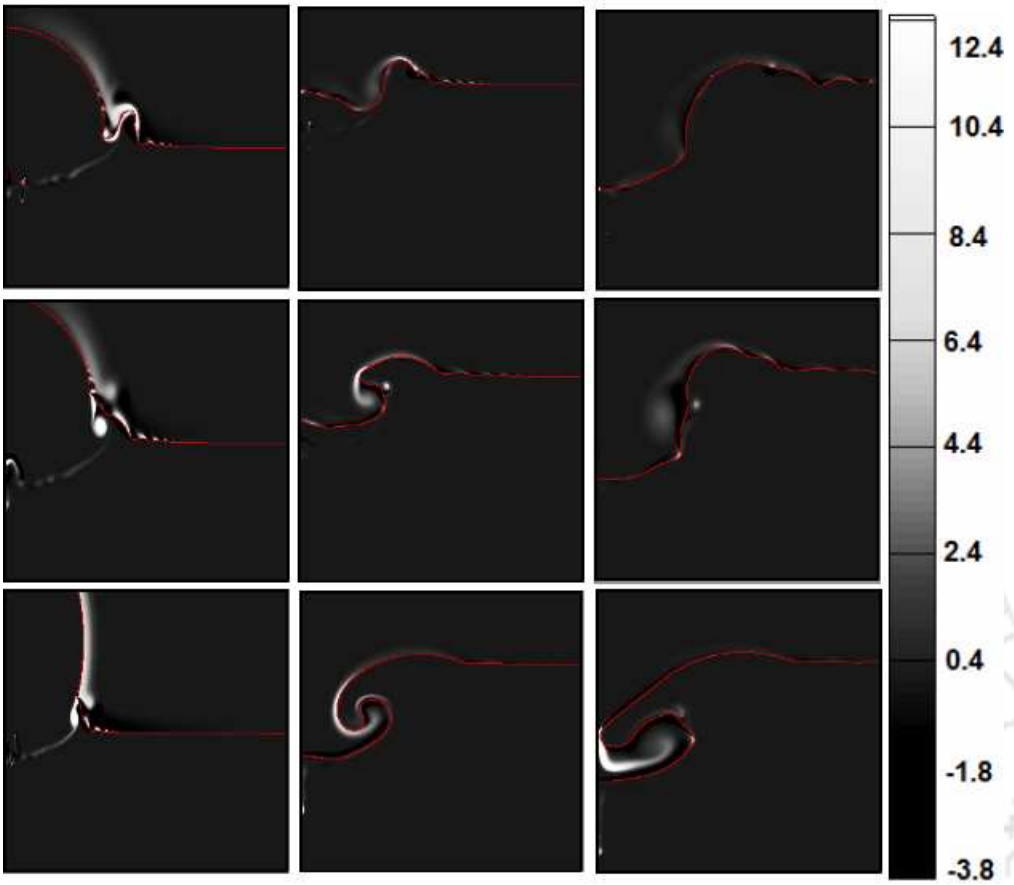

Figure 4.14: Vorticity contour for top row: oblate shaped drop ($AR = 0.75$), middle row: spherical drop ($AR = 1$) and bottom row: prolate shaped drops ($AR = 1.37$). The first sub-figure in each row is enlarged to show the vortex ring. The contour legends indicate vorticity values scaled down by a multiple of 10^{-3} from its values in SI unit. The other parameters are same as in Fig. 4.13.

interface starts early. The early pull of the interface destructs the strength of the vortex. For the prolate shaped drops where the vortex penetrates deep into the pool, the vortex strength is not destructed by early interface pull and hence it forms an elongated roll jet that merges at the centerline leading to large bubble entrapment.

4.4.4 Jet formation

For a particular range of drop diameter and impact velocity, the crater collapses in a way that always leads to the entrapment of air bubble below it. Pumphrey and Elmore [75] referred to this as "regular entrapment"since for such impact conditions,

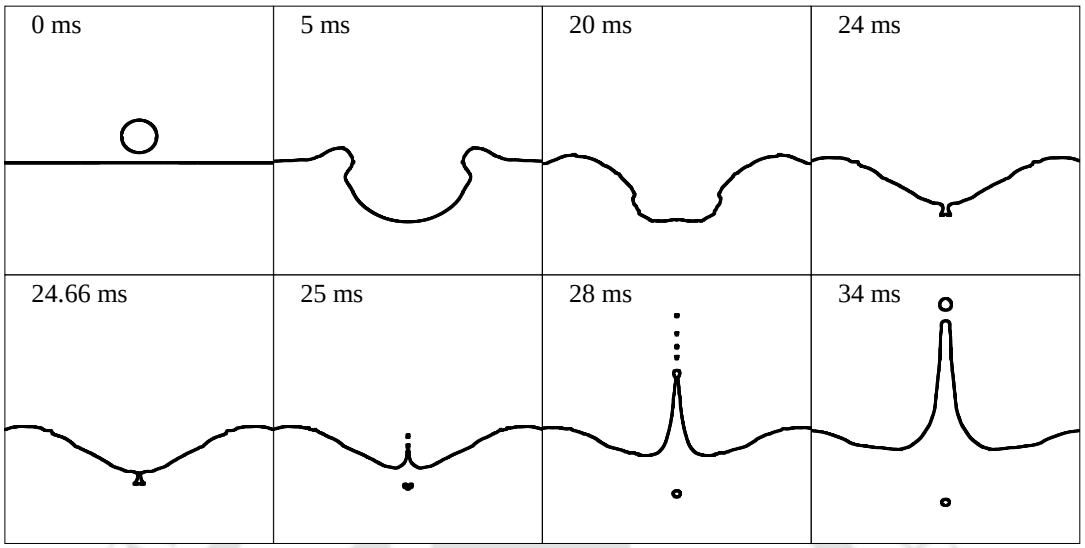

Figure 4.15: A typical case of regular bubble entrapment for the impact of a drop of diameter 2.8 mm and impact velocity 2.2 m/s. Other parameters are $We = 193$ and $Fr = 176$.

crater collapse always leads to bubble entrapment. This regular bubble entrapment region is identified on the traditional classification map as shown in Fig. 4.1. Figure 4.15 shows a typical case of regular bubble entrapment. The regular bubble entrapment is followed by the formation of a rising liquid jet which may be a thick jet or a thin jet depending on the impact parameters [4]. The crater depth and the jet height increase with the increase in impact velocity of the drop.

The entrapment of large bubble is also accompanied by a high-speed inward jet which is commonly known as Worthington jet [96, 97] and an outward jet as seen in Fig. 4.16(b). The inward jet and the outward jet start to emerge as the liquid tongue merges at the top of the crater to entrap the bubble. The inward liquid jet moves downward and starts penetrating the bubble. When this liquid jet touches the bottom of the entrapped bubble it transforms the shape of the bubble into a toroidal shape (Figs. 4.16(c) and 4.16(d)). The toroidal bubble later recombines at the centerline with an elongated liquid column inside it (Figs. 4.16(e) and 4.16(f)). This liquid column breaks into fragments due to instability as depicted in Figs. 4.16(g) and 4.16(h). The upward jet also forms a short, thin liquid column that returns back to the pool at a later time (Figs. 4.16(c)-4.16(h)).

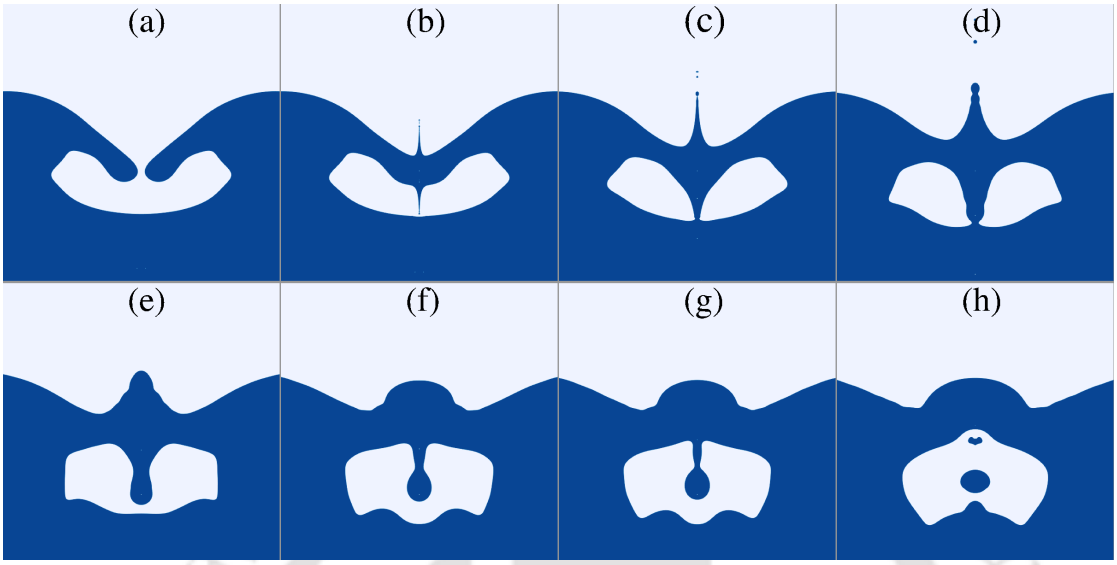

Figure 4.16: The evolution of the inward and the outward jet that forms during the large bubble entrapment. The profiles are for the impact of a drop of 5 mm equivalent diameter onto a liquid pool at an impact velocity of 1 m/s. The initial aspect ratio of the drop is 1.37. The other parameters are $We = 69$ and $Fr = 20.4$. The liquid tongue formed by roll jet can be seen in (a). An inward and outward jet emerges as the two liquid tongue merges as seen in (b). The inward jet penetrates to the bottom of the bubble making its shape toroidal as seen in (c) and (d). The toroid later recombines as evident in (e) and (f). The inward liquid column then break into fragments as seen in (g) and (h).

4.4.5 Effect of impact velocity and drop size

The enclosure depth (Z_n) of bubble entrapment decreases with the increase in impact velocity of the drops (Fig. 4.17). The enclosure depth is defined as the depth from the initial liquid pool interface to the point where the emanating liquid tongue from the periphery of the cavity first merges on the axis of symmetry. The trend of the experimental results is similar to that of the simulations. The little discrepancy in the experimental data is resulted from the effect of changed aspect ratio, as aspect ratio variation is not controllable in experiments. The crater depth (Z_c) also decreases with the increase in velocity of the impacting drops (Fig. 4.18), although, the crater depth is expected to be higher for higher impact velocity because of higher inertial force. This is in contrary to the regular entrapment case, where the crater depth increases with the increased impact velocity [79]. This is because, with the increase in impact velocity of the drop, it produces a stronger vortical flow near the

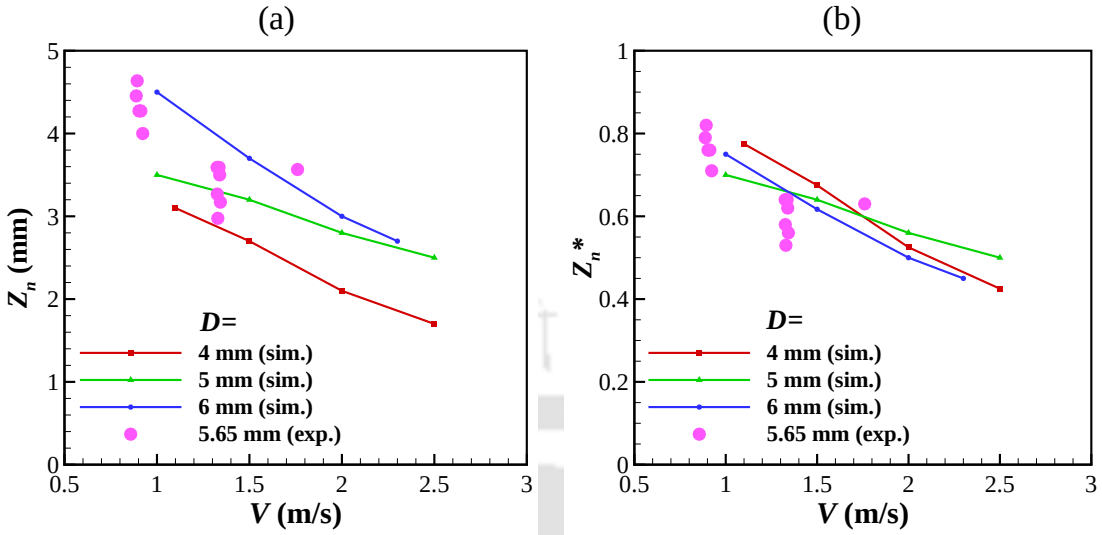

Figure 4.17: Variation of enclosure depth (Z_n) of the bubble for different impact velocity (V). The enclosure depth is shown in dimensional form in (a) and in non-dimensional scale in (b). The non dimensional depth, Z_n*, is defined as $Z_n^* = Z_n/D$. The aspect ratio of drop for all the simulations is 1.37.

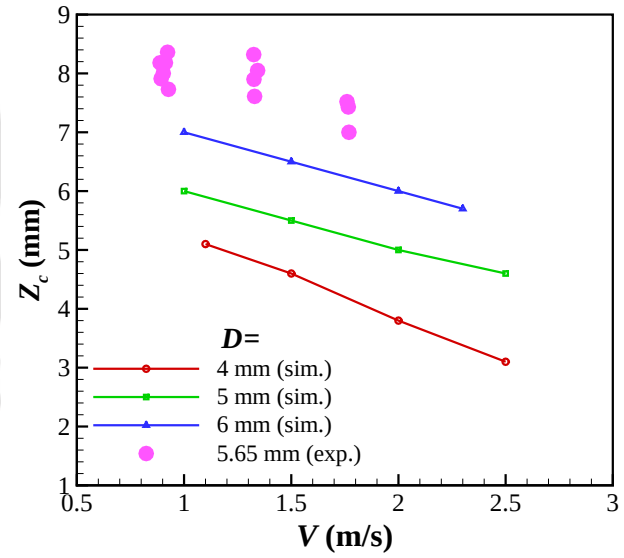

Figure 4.18: The crater depth (Z_c) inside the liquid pool is plotted for different impact velocity. The impacting drops have aspect ratio 1.37 in all the simulations.

interface. The vortex starts early interaction with the interface. The interaction with the interface brings about the formation of the roll jet. The roll jet thus formed, merges early. This can be seen in Fig. 4.19(a) that the pinch-off time (t_p)

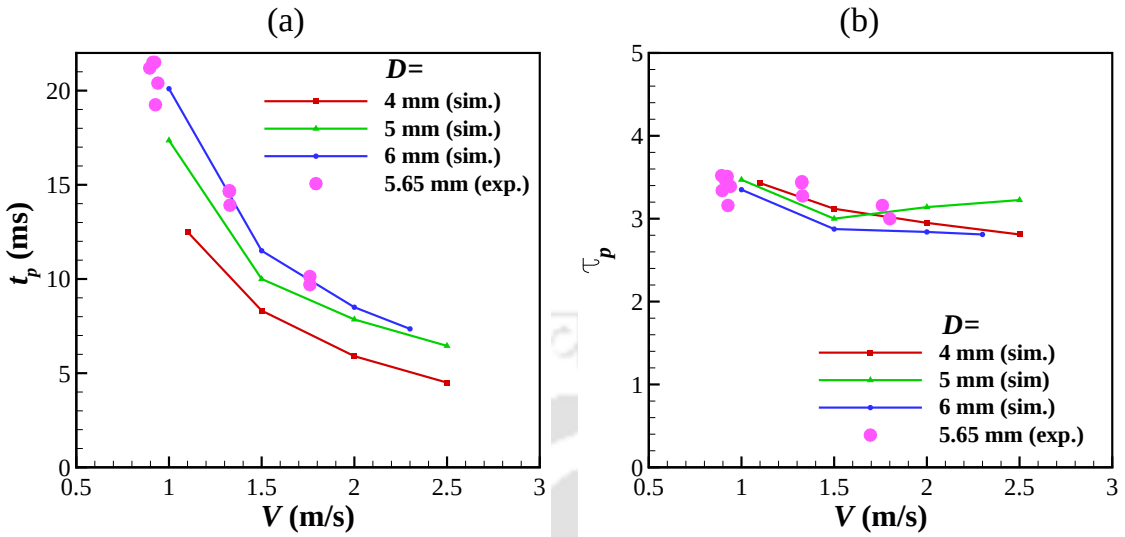

Figure 4.19: Variation of pinch-off time (t_p) of the bubble with the change of impact velocity (V). The dimensional pinch-off time (t_p) is plotted in (a) and the non-dimensional pinch-off time (τ_p) is plotted in (b). The aspect ratio of drop for all the simulations is 1.37.

of the bubble decreases at higher velocity. At a lower velocity of impact, the vortex moves deeper into the pool, which delays its interaction with the interface. This, in turn, delays the roll jet formation and also makes the crater to move deeper into the pool as depicted in Fig. 4.18. With the increase in drop volume, the crater depth increases because of higher inertial force. Increased drop volume increases the opening of the crater mouth that in turn delays the pinch-off time (Fig. 4.19(a)) resulting in deeper penetration of the crater. In non-dimensional time scale ($\tau_p = t_p V/D$), the pinch-off time is very close in all the cases and the value is close to 3.2 (Fig. 4.19(b)). There is an excellent consistency between the numerical and the experimental results. This is consistent with the earlier observations [53], where the range of τ_p is mentioned to vary between 2.7 and 3.5.

4.5 Summary

In this investigation, the mechanism of large bubble entrapment has been analyzed in detail. The regime of large bubble entrapment has been identified and a modified phase diagram for large bubble entrapment has been proposed on the V-D map and on the We-Fr map. Large bubble entrapment has been observed only for the

drops that are prolate at the time of impact. Sometimes the large bubble entrapment takes place together with the entrapment of a small bubble. The mechanism of large bubble entrapment is driven by the vorticity generated near the interface during drop impact. The vortex separates out from the interface and penetrates into the poll forming a vortex ring. Later, the vortex curls-up the interface and forms a roll jet. The roll jet merges at the central axis and entraps a large bubble inside the liquid pool. The emergence of merged ejecta-lamella sheet prevents the separation and penetration of the vortex ring onto the pool, which in turn, prevents the entrapment of large bubble. Large bubble entrapment is always accompanied by the formation of an inward and an upward jet.

Chapter 5

Dynamics of the cavity generated during the impact of high-speed microdrops

5.1 Introduction

The impact of liquid drops on a liquid or solid surface has been studied for centuries because of its importance in a wide variety of industrial applications and natural phenomena. Worthington [1] first reported different paradigms of drop impact on a liquid pool, captured using high-speed photography. Depending on the drop size, fluid properties, and flow parameters, different regimes were observed, such as jet formation, secondary drop formation, crown formation etc. Ray et al. [4] interpreted these phenomena as the consequences of different crater dynamics. Based on the shape of the crater, expansion and contraction time, the final outcome can be coalescence, jet formation with bubble entrapment or without bubble entrapment and splashing.

For the impact of a single drop of millimeter size, different categories of bubble entrapment were identified [75, 76, 98] such as regular entrapment, irregular entrapment, large bubble entrapment and Messler entrapment. At sufficiently low veloc-

The contents of this chapter have been published as an article entitled "Dynamics of tongue shaped cavity generated during the impact of high-speed microdrops", *Physics of Fluids*, 2018, vol. **30**(4), p. 042103.

ities, typically no bubble is entrapped. For a given drop size and impact velocity, the bubble entrapment is highly reproducible, and this behavior is referred to as small regular bubble entrapment. There is a second critical velocity above which bubbles are no longer regularly entrapped. During regular bubble entrapment, the bubble pinches off at the bottom of the crater during crater collapse. Pumphrey and Elmore [75] gave a range of upper limit and lower limit on the drop diameter (D) - impact velocity (V) plane and also on the Weber number ($We = \rho V^2 D/\sigma$) - Froude number ($Fr = V^2/gD$) plane, for regular bubble entrapment. The upper bound and the lower bound of this region were determined by Oguz and Prosperetti [76] as $We_u = 48.3Fr^{0.247}$ and $We_l = 41.3Fr^{0.179}$ respectively. In the case of large bubble entrapment, the single large bubble reproducibly pinches off at about halfway along the distorted cavity, which has been described in detail in Chapter 4. Such entrapments occur only for drops that are prolate at impact.

The impact of micrometer-sized drops has received more attention recently. This is because of the increasing applications of micrometer-sized drop-impacts such as in ink jet printing, immersion lithography, extreme ultraviolet lithography, 3D printing, spray painting and spray coating etc. Kim et al. [99] studied the impact of high-speed microdrops on solid surfaces and observed that the drops rapidly collapse into a thin disk after impacting the solid surface. After having reached the maximum spread, the drop recoils back due to surface tension force and increases the disk thickness. Visser et al. [100] investigated the impact of high-speed microdrops on a solid surface and reported the similarities and differences between millimeter-sized drop impact and micrometer-sized drop impact. Despite having high impact velocities up to 50 m/s, they did not observe splash for micrometer-sized drops. Chan et al. [101] studied the impact of high-speed microdrops on a deep liquid pool. They were the first to show the long slender cavity formation due to multiple drop impact on a deep liquid pool. They showed in their movie, the effect of number of impacting drops, keeping the drop diameter, impact velocity and frequency constant for all cases. Hurd et al. [102] again showed experimentally the detailed structure of the nested cavity shape formed in the wake of multiple drops and named it as the *matryoshka* cavity. They showed that for ideal impact frequency, a long conical cavity can be formed, extending much deeper below the free surface and lasting longer than a cavity generated from a single drop impact. Bouwhuis et al. [103] further investigated both experimentally and numerically the deep and narrow cavity as showed in Fig. 5.1, whose behavior is mainly determined by the inertial effects.

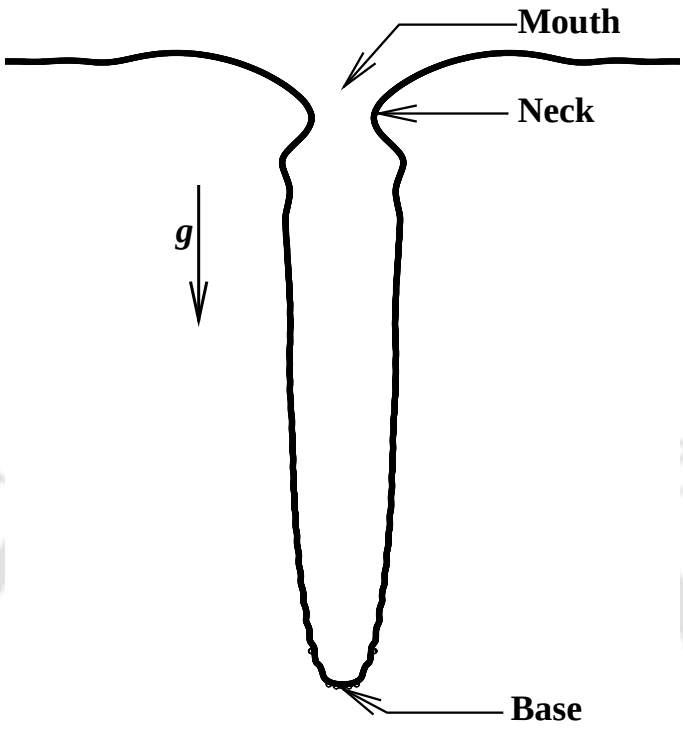

Figure 5.1: Schematic of the tongue shaped cavity formed during the impact of a train of high-speed microdrops.

They used the boundary-integral method to simulate the impact of a high-speed train of microdrops on a deep liquid pool, without considering the viscous effect. Because of the limitations of the boundary-integral method, they neglected the flow of air due to the movement of the drop train. Consequently, the deformation of the drop due to the drag force of air before it touched the liquid pool and the dynamic pressure drop because of the flow of air, were neglected. Although such assumptions affected the cavity dynamics, their investigation gave a good qualitative idea about many promising facts on the cavity behavior. The maximum radius of the cavity and the depth of the cavity were well predicted in their study based on a modified Weber number $We_m = \rho V_c^2 R/\sigma$, where V_c is the penetration speed of the cavity and R is the radius of the impacting drops. Such a cavity resembles the cavity created by the controlled impact of a solid disk on a liquid pool [104] or a cavity created by the impact of a solid sphere on a liquid pool [105].

However, all the previous studies could not explain following questions: (a) how the capillary waves generated during multiple drop impact affect the necking and

pinch-off, (b) how does the train length affect the cavity shape and most importantly (c) can we give a regime map in terms of non-dimensional numbers for the pinch-off of the cavity. Because of the complex nature of the phenomena, detailed investigations are needed for complete understanding of the underlying physics. Numerical investigation of such cavity behavior is a challenging task, because of high impact velocity and small dimension of the impacting drops. In the current investigation, we have attempted to numerically simulate the cavity penetration and collapse processes using CLSVOF method to elucidate the underlying physics and to solve the numerical challenges faced by the earlier researchers. This work aims at answering the above questions in terms of certain non-dimensional numbers which make the results universal and comparable with similar long slender cavity pinch-off phenomena during solid sphere impact or jet impact on a deep liquid pool.

5.2 Formulation

5.2.1 Computational domain

An axisymmetric coordinate system (r, z) is used to model the flow dynamics, where r and z represent the radial and axial coordinates, respectively. A representative diagram of the computational domain is shown in Fig. 5.2. The microdrops of diameter D hit the liquid pool with velocity V. The drops and the pool are of same liquid (Fluid 1). In the computational domain, the width $W = 25D$ and the height above the liquid pool $H_2 = 25D$ are kept constant in all the simulations, while the depth of the liquid pool H_1 is varied from $50D$ to $200D$ depending on the number of drops in the microdrop train. The pool liquid and the drop liquid are the same. The drops are initialized with a velocity equal to the impact velocity of the drops, at a height of $20D$ above the liquid pool interface. These microdrops pass through the surrounding fluid (Fluid 2) and continuously hit the liquid pool one after another. A periodic initialization technique is used, which initializes a drop after a predefined time interval to maintain the continuity of the train based on the frequency of drop impact. Present investigations are performed using an air-water system with constant temperature.

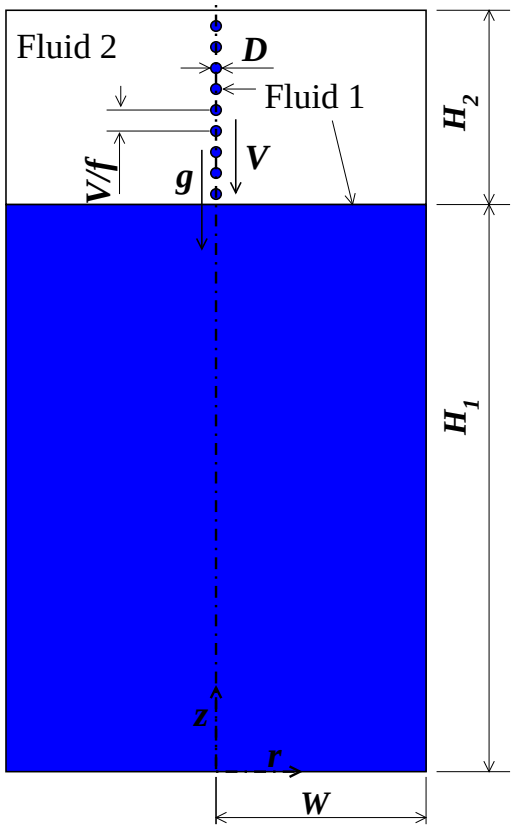

Figure 5.2: Computational domain for performing the simulations of impact of a train of high-speed microdrops on a deep liquid pool. The drops of diameter D impacts the liquid pool with velocity V. The width of the domain $W = 25D$ and the height above the liquid pool $H_2 = 25D$ are kept fixed in all the simulations. The depth of the liquid pool H_1 is varied from $50D$ to $200D$, depending on the number of drops in the microdrop train.

5.2.2 Boundary conditions

In the computational domain we have performed axisymmetric simulations and the axis of symmetry lies on the left boundary. At the axis of symmetry no fluid exits or enters the domain. This can be mathematically expressed in terms of the velocity components (u, v) along the $r-$ and $z-$directions as

$$u = 0, \frac{\partial v}{\partial r} = 0. \tag{5.1}$$

The same boundary conditions can be applied on the right boundary as the right boundary is considered to be frictionless. On the bottom wall we deploy the no-slip boundary condition and the impermeability condition,

$$u = v = 0. \tag{5.2}$$

At the top boundary, the natural Neumann boundary condition is applicable given as

$$\frac{\partial u}{\partial z} = \frac{\partial v}{\partial z} = 0. \tag{5.3}$$

The Neumann pressure boundary condition is applied at all the boundaries except at the top boundary where pressure is equal to the atmospheric pressure P_{atm}.

5.2.3 Scaling analysis

The physical parameters which are involved are density ρ, dynamic viscosity μ, surface tension σ, acceleration due to gravity g, drop diameter D, drop impact velocity V, frequency of drop impact f and length of drop train (center to center distance of first and last drop in the train) $L_t = (N-1)V/f$, where N is the number of drops in the train. There are three independent fundamental physical quantities: length, mass and time. Using Buckingham π theorem, five non-dimensional numbers can be obtained. These non-dimensional numbers are Reynolds number $Re = \rho V D/\mu$, Weber number $We = \rho V^2 D/\sigma$, Froude number $Fr = V^2/gD$, non-dimensional frequency $\tilde{f} = Df/V$ and non-dimensional train length $\tilde{L}_t = L_t/D$. The last two non-dimensional numbers can be combined to $\tilde{L}_t = (N-1)/\tilde{f}$. Here, the drop diameter D is used as the length scale, and time t is scaled by the inertial time D/V as $\tau = tV/D$. Thus, non-dimensional length and non-dimensional time scales are functions $F(Re, We, Fr, \tilde{L}_t)$ of these four non-dimensional numbers.

5.3 Validation and grid-independent test

In order to validate our results on the impact of high-speed microdrops, we compared our results with the experimental results of Bouwhuis et al. [103]. Figure 5.3 shows

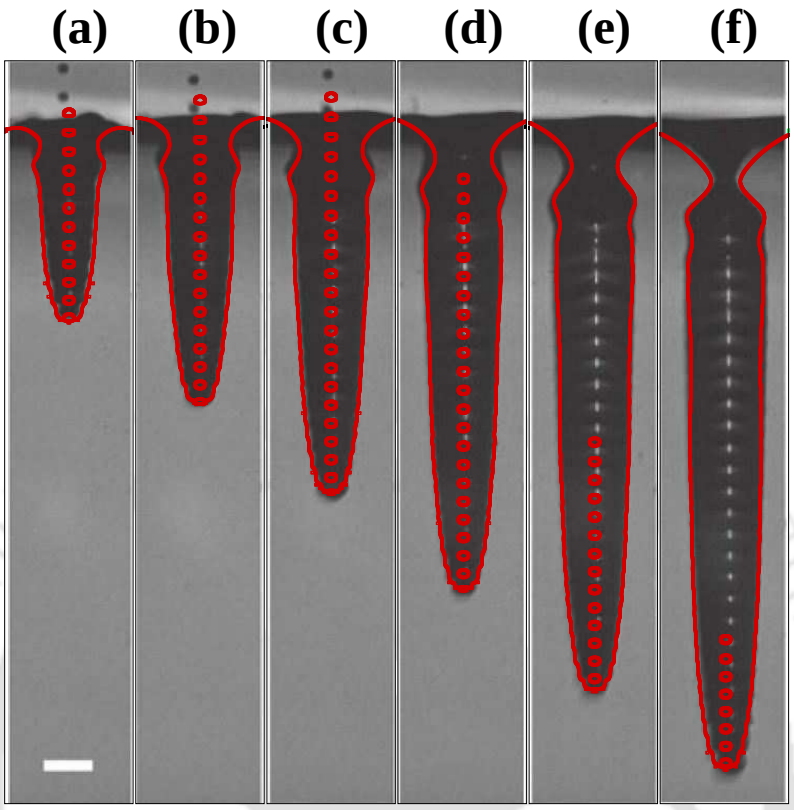

Figure 5.3: Comparison between the numerical results of present investigation and the experimental result of Bouwhuis et al. [103] for the impact of a train of water drops having diameter 40 μm and a frequency of 290 kHz. The impact velocity of the drops is 30 m/s. The results obtained from our numerical simulations (red colored profiles) are overlapped over the experimental photographs of Bouwhuis et al. [103]. Each profile $((a)-(f))$ is captured at every 40 μs interval. The non-dimensional parameters are $Re = 1200$, $Fr = 22.9 \times 10^5$, $We = 496$ and $\tilde{L}_t = 152.6$.

the comparison of our numerical results with the experimental results for the impact of a microdrop train on a deep liquid pool, with an impact velocity of 30 m/s and frequency of 290 kHz. The drop liquid is water ($\rho_1 = 998$ kg/m^3 and $\mu_1 = 10^{-3}$ Pa.s) and the surrounding fluid is air ($\rho_2 = 1.204$ kg/m^3 and $\mu_2 = 1.82 \times 10^{-5}$ Pa.s). For high-speed impact of a train of microdrops, the cavity depth increases much larger than the diameter of the impacting drops. This is because of continuous momentum transfer to the cavity by the train of microdrops. The penetration of the cavity in the liquid pool is well captured in our simulation.

Quantitative validations are performed by plotting the penetration depth of the cavity at different time instants, which has been shown in Fig. 5.4. The results

of Bouwhuis et al. [103] are denoted by the solid circles, and the continuous line represents our numerical result. The cavity depth increases continuously until the drop impact stops. The cavity mouth then closes, which results in entrapment of a bubble inside the liquid pool. The drops inside the cavity may continue to impact on the cavity base, even after the pinch-off. The cavity depth continues to increase until all the drops impact the cavity base. Our numerical results show an excellent match with the experimental results of Bouwhuis et al. [103] as depicted in Fig. 5.4.

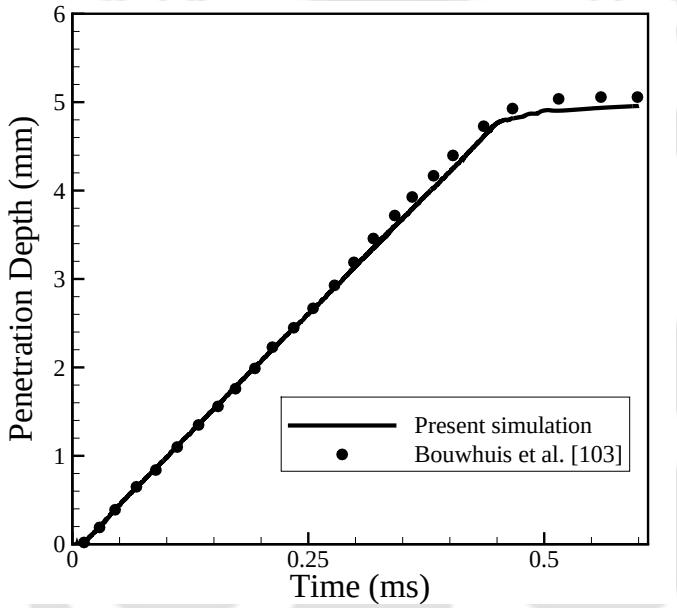

Figure 5.4: Comparison between the numerical results (solid line) of present investigation and the experimental results of Bouwhuis et al. [103] (solid circles) for temporal variation of penetration depth of the cavity. The impacting drops have diameter 40 μm, and frequency 290 kHz. The non-dimensional parameters are Re = 1070, $Fr = 18.23 \times 10^5$, We = 395 and $\tilde{L}_t$ = 193.7.

In order to perform the grid independent test, we deployed four different grid-meshes: 250 × 750, 500 × 1500, 570 × 1750 and 650 × 2000, for a train of 20 microdrops, having diameter 40 μm, impact velocity 26.75 m/s and frequency 290 kHz. Table 5.1 shows the penetration depth of the cavity at the time of pinch-off, for different grid-meshes. In Table 5.1, it can be seen that the percentage difference in penetration depth for the grid-meshes of 250 × 750 and 500 × 1500 is 10.63 %, while for the grid-meshes of 500 × 1500 and 570 × 1750 the percentage difference in penetration depth is 2.02 %. For the grid-meshes of 570 × 1750 and 650 ×

2000, the percentage difference in penetration depth of the cavity at the time of pinch-off is 0.14 %, which is very small. Hence, for the train of 20 microdrops, a grid-mesh of 570 × 1750 is used. Likewise, with a refined grid, our simulated results are grid-independent for all the trains of microdrops considered in this study.

Table 5.1: Grid-independent test for the impact a high-speed train of microdrops on a deep liquid pool.

Grid-mesh	Penetration depth (mm)	Change (%)
250 × 750	1.251	–
500 × 1500	1.384	10.63
570 × 1750	1.412	2.02
650 × 2000	1.414	0.14

5.4 Results and discussion

The behavior of the microdrops is different from that of the millimeter-sized drops. Because of the small size of the microdrops, they can travel at very high speed, without breakup. The depth of the crater formed by the impact of a high-speed microdrop is more because of larger inertial force. The penetration depth can be increased by consecutive drop impact. As reported in the literature [103], the penetration depth can be increased more than 1000 times the diameter of the drop by the impact of a train of high velocity microdrops. The cavity thus formed, closes at a later time, which results in entrapment of a bubble inside the liquid pool.

5.4.1 Cavity capillary waves

The interesting tongue-like shape of the cavity is formed due to the continuous impact of high-speed microdrops. When a drop impacts on a liquid pool, its momentum gets transferred into the pool, which makes the liquid in the pool to move outward in all directions from the point of impact. This results in formation of a crater in the pool. The crater initially expands until the momentum transferred by the impacting drop dissipates, and then it starts to retract. During the impact of multiple drops, the second drop hits the base of the crater formed by the impact of

the first drop and forms another crater at the base of the first crater. Likewise, for a train of drops, the drops hit the crater base continuously, and due to the continuous transfer of momentum, its penetration increases continuously, which results in formation of a deep cavity.

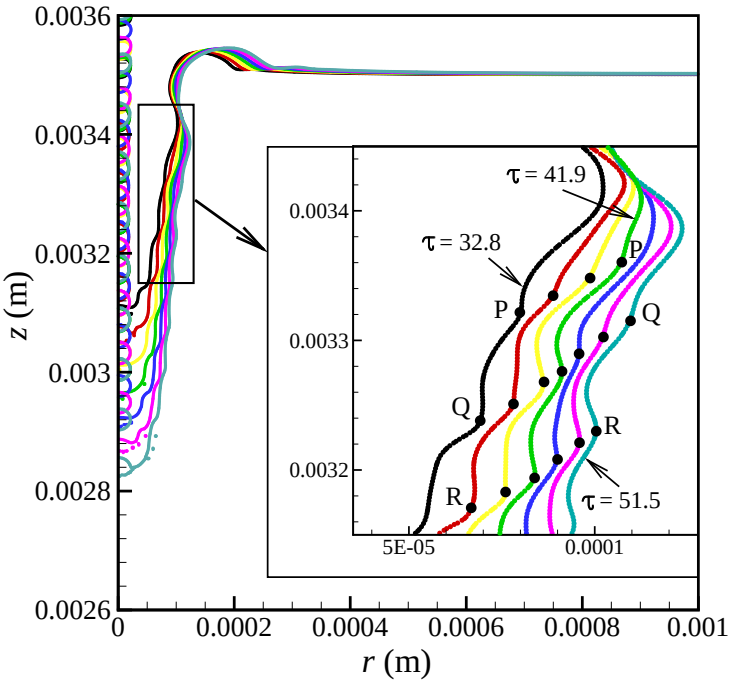

Figure 5.5: The interface profile of the cavity at different instants of time during the impact of a droplet train of 25 droplets having drop diameter 40 μm and impact velocity 26.75 m/s. The propagating capillary waves with distinct crest and trough can be seen in the zoomed view of the interface profiles. The wave crests marked by points P, Q and R are tracked at different instants of time and which show wave propagation with time. The dimensionless parameters are $\tilde{L}_t = 55.35$, $Re = 1070$, $Fr = 18.2 \times 10^5$ and $We = 395$.

Capillary wave culminates from the drop impact on the crater base. As multiple drops impact the crater, we see multiple waves emerging from the crater base and moving through the crater wall. The interface profiles of the cavity over a range of time is shown in Fig. 5.5 along with an enlarged view of a given location of the domain where distinct wave crests and troughs are clearly visible. The wave crests marked by points P, Q and R are tracked at different instants of time and are shown in the enlarged view of Fig. 5.5. The points P, Q and R move with time towards the cavity mouth depicting the propagation of the capillary wave along the interface.

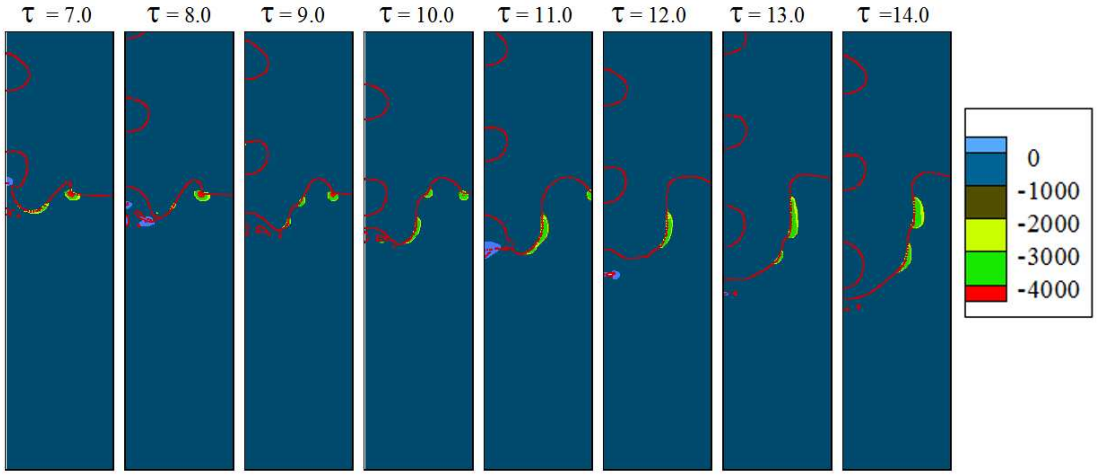

Figure 5.6: Pressure contour showing the generation and propagation of the capillary waves at different time instant during the initial stage of impact. The dimensionless parameters are $\tilde{L}_t = 136.05$, $Re = 1070$, $Fr = 18.2 \times 10^5$ and $We = 395$.

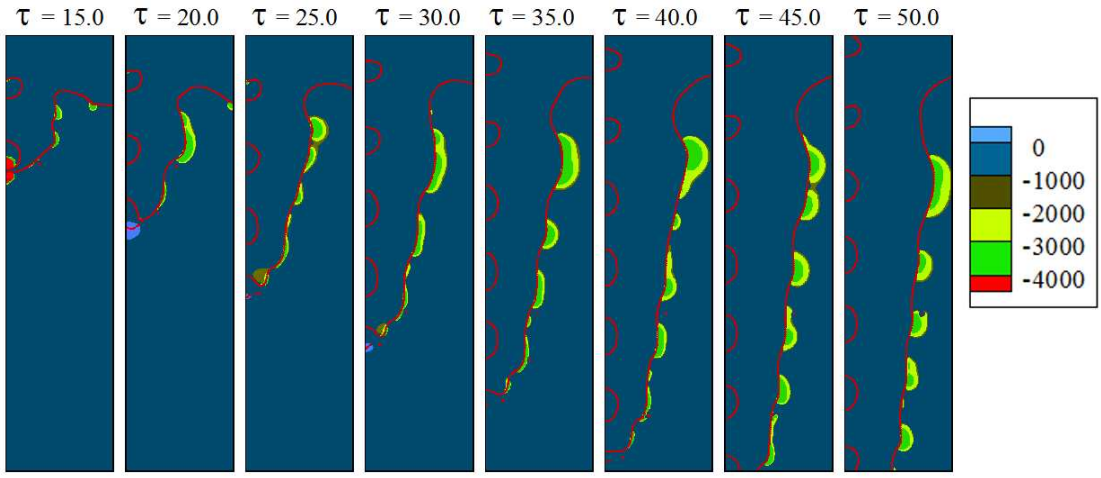

Figure 5.7: Pressure contour showing the propagation of capillary waves along with the penetration of the cavity at different instant of time. The dimensionless parameters are $\tilde{L}_t = 136.05$, $Re = 1070$, $Fr = 18.2 \times 10^5$ and $We = 395$.

The capillary waves propagate through the interface and converge near the cavity mouth. It can be seen in Fig. 5.5, where the wave crest P merges with the large amplitude wave crest near the neck after time $\tau = 41.9$. Each drop impact produces a capillary wave. During the impact of drops, capillary waves are produced by the expanding crater owing to the high curvature generated at the base. At wave crest the velocity of fluid is maximum and pressure is minimum. Capillary waves on the

crater can be seen by plotting the pressure contour, where lowest pressure value identifies the point of wave crest as shown in Figs. 5.6 and 5.7. The points where the contours are more pronounced and cover more regions signify large amplitude waves. Thoroddsen et al. [106] and Ding et al. [107] showed that when a drop comes in contact with the liquid surface, capillary waves generate at the point of contact and gradually the amplitude of the wave decays as it travels. Ray et al. [108] showed capillary waves for drop impact into liquid pool for different Weber numbers. In this study, since there are multiple impacting drops, the number of waves keeps on increasing until the last drop impacts on the pool. The wave crest with largest amplitude close to the surface leads to necking and pinch off. This particular wave crest is created owing to the impact of the first drop and its amplitude grows as the subsequent waves follow it. This can be seen in Fig. 5.6, which shows the generation and propagation of the capillary waves at the initial stage of impact. Using ideal-flow theory, the speed of a capillary wave of wavelength λ can be calculated as (Kundu and Cohen [109], page 237)

$$c = \sqrt{\frac{2\pi\sigma}{\rho\lambda}}. \tag{5.4}$$

A wave of arbitrary shape is composed of several Fourier components. Each component will have different phase speed as the wave speed depends on its wavelength. A reference velocity with which the wave packet moves, called group velocity can be obtained as (Kundu and Cohen [109], page 241)

$$c_g = \frac{3}{2}\sqrt{\frac{2\pi\sigma}{\rho\lambda}}. \tag{5.5}$$

The propagating capillary waves are continuously damped by viscosity. The capillary waves are generated at very fast rate owing to the large frequency of the impacting drops. As a result, the capillary wave generated by a drop impact merges with the wave generated by the earlier drop. In the subsequent impacts, as the cavity depth increases, the capillary waves merge below the first peak and produce local peaks as seen in Fig. 5.7. When the value of $\tilde{L}_t$ is smaller, the capillary wave generation stops early and reduces the effect of capillary wave motion on the movement of the cavity mouth. The role of the capillary waves during pinch-off is discussed in detail in Sec. 5.4.3.

5.4.2 Cavity penetration dynamics

The penetration depth of the cavity depends on the momentum transferred to the pool by the impacting microdrops. For each drop impact, the momentum dissipation takes a finite duration of time, during which the crater wall moves outward and downward. This stage is called the expansion stage of the crater. During the expansion stage, the penetration velocity of the crater is highest at the beginning and decreases continuously owing to viscous dissipation. The penetration velocity of the crater is defined as the velocity at which the crater base penetrate the liquid pool. The decay in penetration velocity with time for a single drop impact is widely reported in literature [79, 110, 111]. When the second drop impacts the crater base, its velocity again starts from a peak and decays continuously and finally its retraction starts. Whenever the second drop hits the crater base, after its retraction due to the first drop starts, some of its momentum is lost in overcoming the retracting force. This makes the penetration of the crater formed by the impact of the second drop less, which finally results in less penetration of the cavity. With the increase in $\tilde{f}$, the time interval between two consecutive impact decreases and the second drop impacts before the reversal of the crater formed by the impact of the first drop. The same process happens for the next drop and so on. Because of this, a continuous increase in penetration depth is seen in Fig. 5.8(a) with the increased frequency. However, after a certain limit, the phenomena start reversing and the penetration depth decreases with increase in frequency. At a large frequency, the interval between two consecutive drop impact is very small, and the individual craters do not get enough time for expansion and momentum diffusion. The next drop hits the cavity base much before the completion of the expansion stage owing to the impact of the earlier drop, which results in higher accumulation of momentum near the contact region. Subsequently, the momentum gets diffused in all directions. As a result, we observe increase in radial expansion of the cavity together with a decrease in penetration depth. The decrease in penetration depth can be seen for frequency $\tilde{f}$ = 0.52 and $\tilde{f}$ = 0.60 in Fig. 5.8(a). For any given combination of non-dimensional parameters, maximum penetration can be achieved at an optimum frequency. In Fig. 5.8(a), the slope of a line indicates the non-dimensional penetration velocity ($V_c^* = V_c/V$) of that cavity. The penetration velocity of the cavity increases with the increase in $\tilde{f}$, and converges to 1/2 as $\tilde{f} \to 1$, which corresponds to the special case in which momentum is continuously applied to the pool/cavity bottom. This

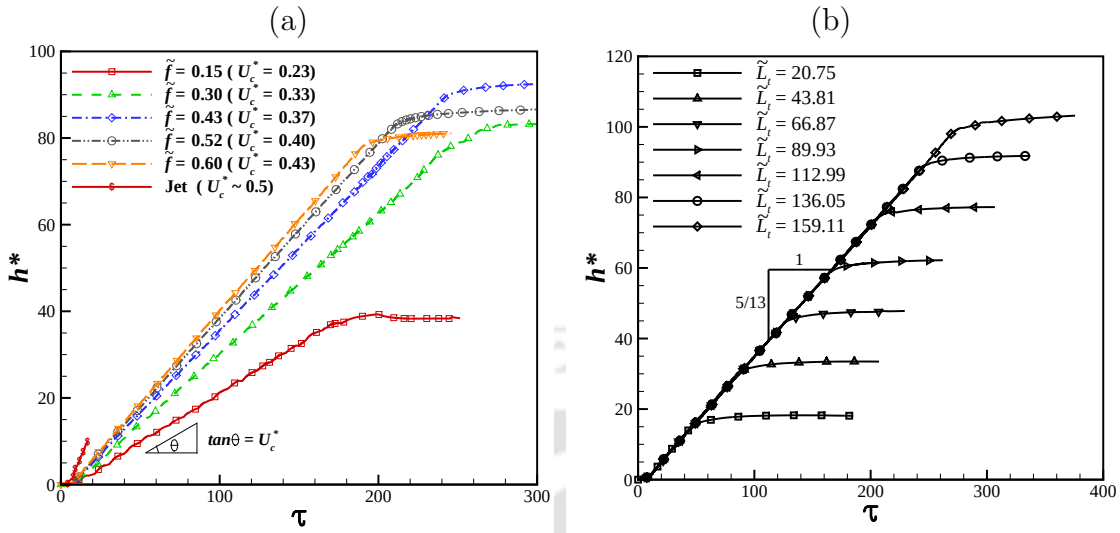

Figure 5.8: (a)Temporal variation of non-dimensional penetration depth of the cavity is plotted for different non-dimensional frequency of impact, along with the experimental data of Zhu et al. [112] for penetration depth during the impact of liquid jets. The other dimensionless parameters considered in the simulation are Re = 1070, $Fr = 18.2 \times 10^5$ and $We = 395$ and $\tilde{L}_t = 98.33 - 393.33$. (b) Temporal variation of non-dimensional penetration depth of the cavity is plotted for different values of $\tilde{L}_t$. The other dimensionless parameters are $Re = 1070$, $Fr = 18.2 \times 10^5$, $We = 395$ and $\tilde{f} = 0.43$.

is in agreement with the earlier observation of Oguz et al. [113] and Zhu et al. [112], for the impact of liquid jets on a liquid pool.

With the increase in $\tilde{L}_t$, as the train length increases, the momentum transfer during impact also increases which in turn increases the penetration depth of the cavity as seen in Fig. 5.8(b) and Fig. 5.9(a). The variation of penetration depth of the cavity with $\tilde{L}_t$ is approximately linear as shown in Fig. 5.9(a). However, the penetration velocity is not affected by the length of the train for a fixed value of $\tilde{f}$ as seen in Fig. 5.8(b) where the slope (h^*/τ) indicates the penetration velocity. The cavity penetration also increases with the increase in Weber number, We, as depicted in Fig. 5.9(b). However, the trend is not similar as that of $\tilde{L}_t$ as increased We also contributes to the widening of the cavity. With increased We, higher momentum is transferred into the pool. The momentum diffuses in all the directions from the point of impact. As a result, the width of the cavity also increases along with the increase of penetration depth.

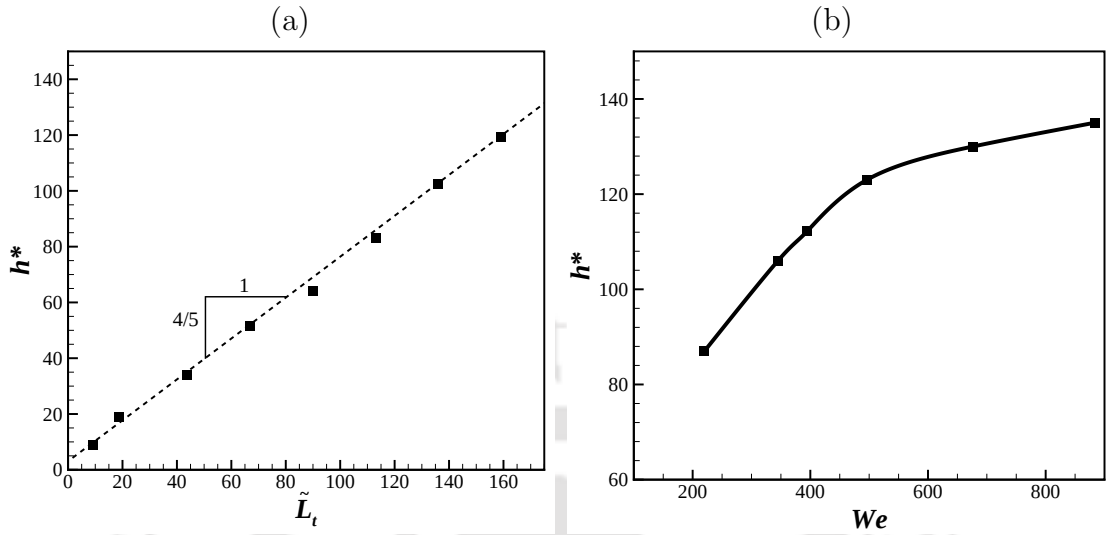

Figure 5.9: (a) The variation of non-dimensional penetration depth of the cavity ($h^* = h/D$) with the change of $\tilde{L}_t$. The other dimensionless parameters are $Re = 1070$, $Fr = 18.2 \times 10^5$ and $We = 395$. (b) Non-dimensional penetration depth of the cavity (h^*) is plotted for different Weber number (We). The other dimensionless parameters are $Re = 800-1600$, $Fr = 10.19 \times 10^5 - 40.7 \times 10^5$ and $\tilde{L}_t = 101.7-203.4$.

5.4.3 Dynamics of necking and pinch-off

In the case of multiple drop impact, the drops hit the cavity base continuously, and due to the continuous transfer of momentum, the depth of the cavity increases continuously. Because of the diffusion of the imparted vertical momentum, the cavity also expands in the radial direction. At a later time, the cavity mouth starts retracting in the inward radial direction and merges at the axis of symmetry. Here, the motion of the cavity mouth can be depicted by a two stage process, namely an expansion stage and a collapse stage. Figure 5.10 shows the time evolution of neck radius ($r^* = r/D$), demarcating the expansion stage and the collapse stage.

The cavities can be classified into two types, one is *shallow cavity* for which all the drops hit the cavity base before the initiation of necking and the other is *deep cavity* for which the drops continue to hit the cavity base even after the initiation of necking and retraction of the cavity mouth. In the case of a shallow cavity, necking starts after completion of the impact of all the drops. The propagating capillary waves reach the neck region and decay before the retraction stage of the cavity mouth starts as seen in Fig. 5.11. Moreover, the retraction and deformation of the entire cavity start during the collapse stage, which finally increases the pinch-off time (τ_p)

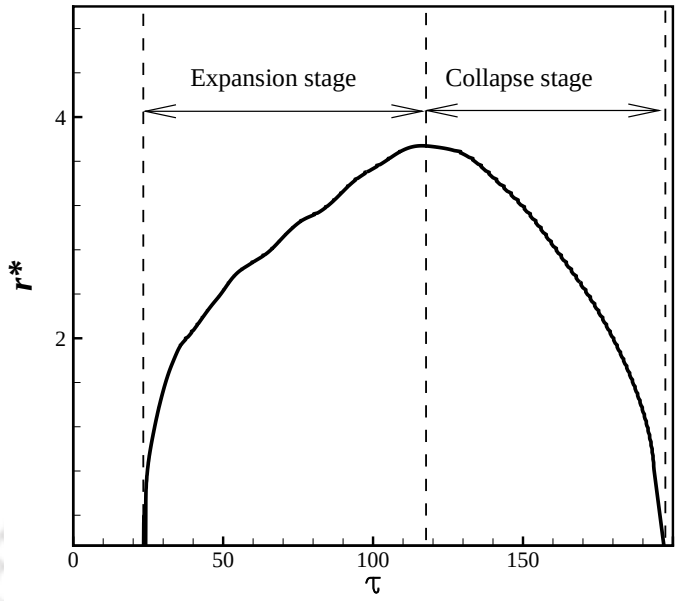

Figure 5.10: Temporal variation of the dimensionless neck radius ($r^* = r/D$) of the cavity. Two distinct stages, namely the expansion stage and the collapse stage have been shown. The microdrop train consists of 60 drops, having impact velocity 26.75 m/s and drop diameter 40 μm. The other non-dimensional parameters are Re = 1070, $Fr = 18.2 \times 10^5$ and $We = 395$ and $\tilde{L}_t = 136.05$.

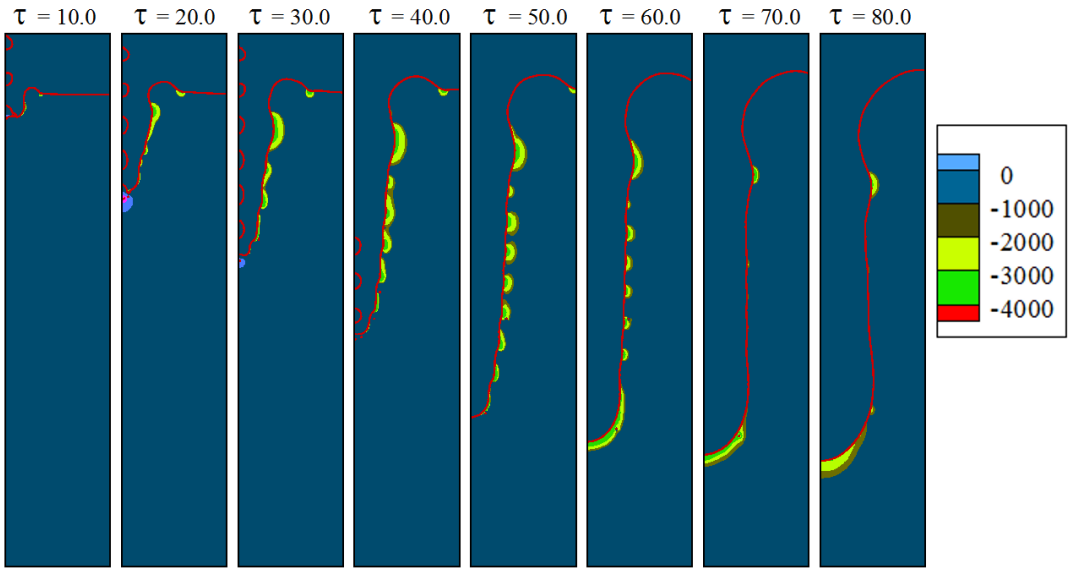

Figure 5.11: Pressure contour showing the propagation of capillary waves at different time instants. The cavity is a shallow cavity having $\tilde{L}_t = 27.67$. The other dimensionless parameters are $Re = 1070$, $Fr = 18.2 \times 10^5$ and $We = 395$.

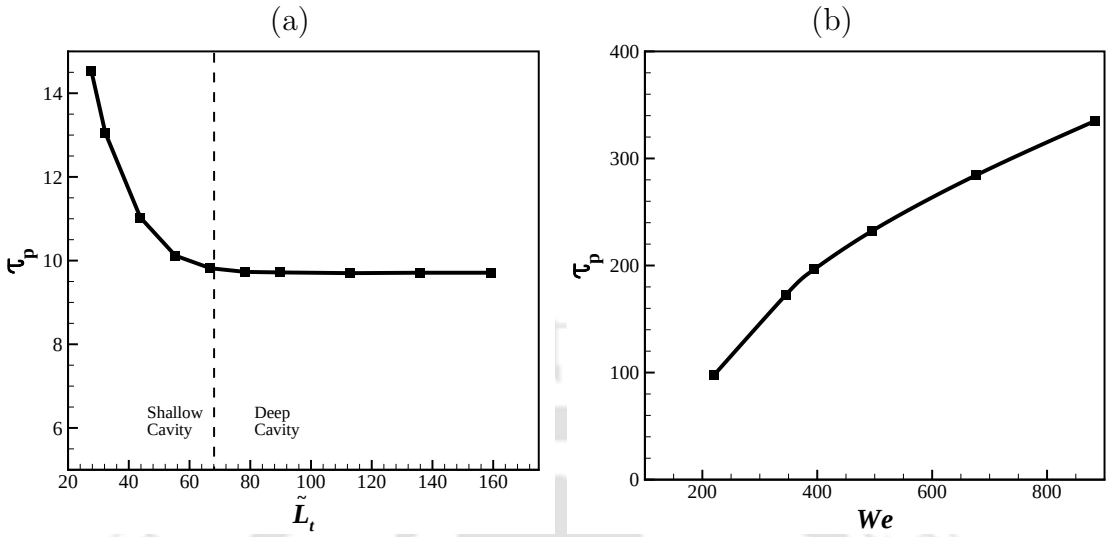

Figure 5.12: (a) The variation non-dimensional pinch-off time of the cavity (τ_p) with the change of $\tilde{L}_t$. The other dimensionless parameters are $Re = 1070$, $Fr = 18.2 \times 10^5$ and $We = 395$. (b) The non-dimensional pinch-off time of the cavity (τ_p) is plotted at different Weber number (We). The other dimensionless parameters are $Re = 800 - 1600$, $Fr = 10.19 \times 10^5 - 40.7 \times 10^5$ and $\tilde{L}_t = 101.7 - 203.4$.

of the cavity. The pinch-off time τ_p is the time taken from the instant the first drop impacts on the interface to the instant pinch-off of the cavity occurs. As the number of drops in the microdrop train increases, because of the continuous impact of the drops on the base of the cavity more capillary waves emerge and propagate through the interface. These capillary waves expedite the necking and retraction of the cavity mouth, leading to faster pinch-off of the cavity. The decrease in pinch-off time for a shallow cavity, with the increase in the train length $\tilde{L}_t$, can be seen in Fig. 5.12(a). However, with further increase in the number of drops in the drop train, the cavity transforms itself into a deep cavity and the pinch-off time becomes independent of the number of drops in the microdrop train. In the case of a deep cavity, the impact of the drops onto the cavity base continues after the initiation of necking and retraction of the cavity mouth. The capillary wave propagation is continuous because of the continuous impact of the drops. However, as the depth of the cavity increases, the capillary waves travel a longer distance to reach the neck region. The viscous effect, continuously damps out the capillary wave propagation, as seen in Fig. 5.13. As a result, the retraction speed of the neck remains almost constant and pinch-off time does not change with further increase in the number of drops in the microdrop train. The pinch-off time of the cavity increases with

the increase in We, as depicted in Fig. 5.12(b). The momentum transferred to the pool by each drop impact increases with the increase in We. Since the momentum gets diffused in all directions, the radial expansion of the cavity increases with the increased values of We. This results in longer duration of the expansion stage of the cavity neck as well as the longer retraction stage of the neck, which finally increases the pinch-off time of the cavity.

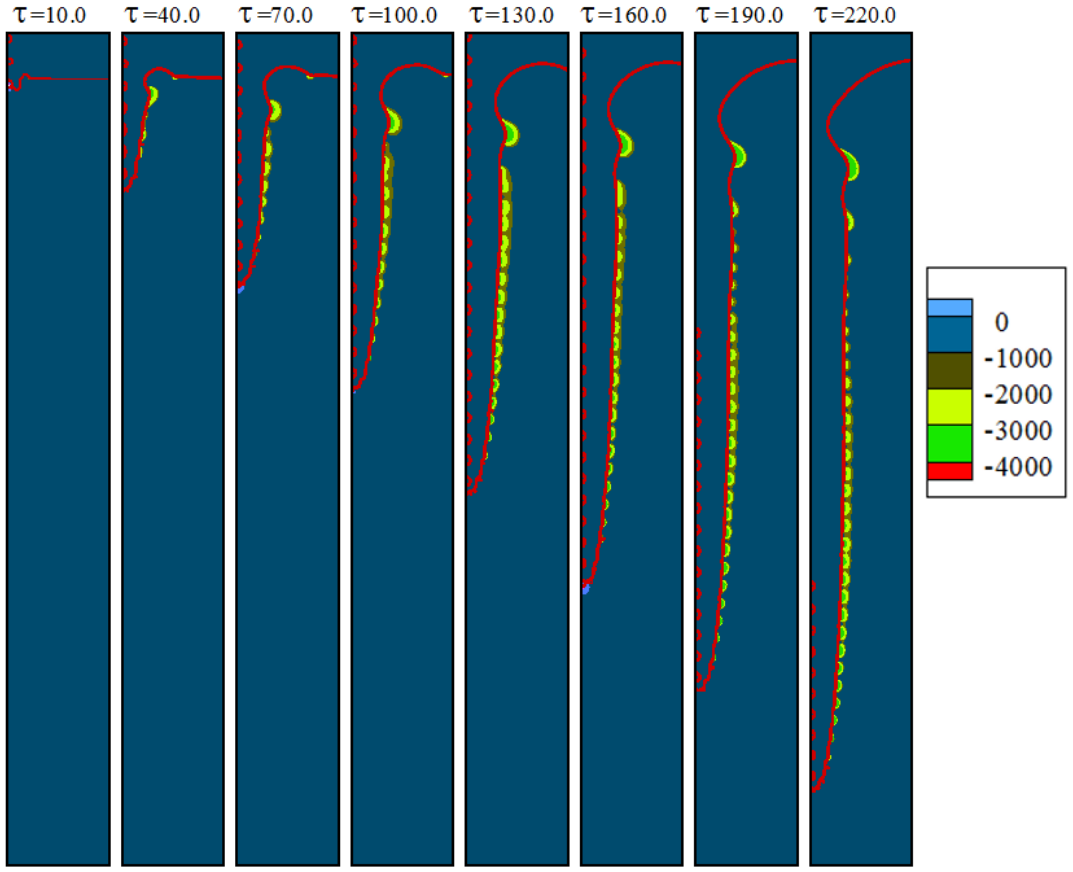

Figure 5.13: Pressure contour showing the propagation of the capillary waves at different instant of time in the case of a deep cavity. The dimensionless parameters are $Re = 1200$, $Fr = 22.9 \times 10^5$, $We = 496$ and $\tilde{L}_t = 152.58$.

The shape of the tongue shaped cavity formed during the impact of a train of microdrops is similar to the shape of the cavity formed during the impact of solid spheres onto a pool. However, the characteristic of the cavity in each of the two cases is different. In the case of impact of solid spheres, Aristoff and Bush [105] observed that with the increase in We the pinch-off depth of the cavity changes significantly. The pinch-off depth is defined as the depth from the initial liquid pool interface

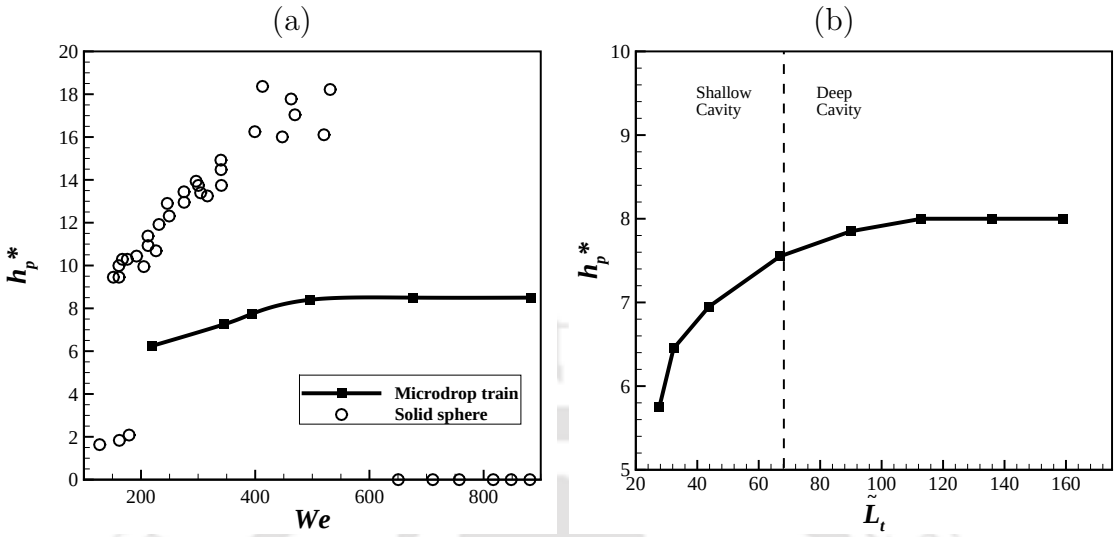

Figure 5.14: (a) The non-dimensional pinch-off depth of the cavity (h_p*) is plotted at different Weber number (We). The other dimensionless parameters are $Re = 800 - 1600$, $Fr = 10.19 \times 10^5 - 40.7 \times 10^5$ and $\tilde{L}_t = 101.7 - 203.4$. The circles represent the results of Aristoff and Bush [105], showing the the pinch-off depth of the cavity at different We during the impact of solid spheres. (b) The variation of non-dimensional pinch-off depth of the cavity (h_p*) with the change of $\tilde{L}_t$. The other dimensionless parameters are $Re = 1070$, $Fr = 18.2 \times 10^5$ and $We = 395$.

to the point where the neck of the cavity merges on the axis of symmetry. They observed different pinch-off regimes such as "shallow seal", "deep seal" and "surface seal" with increased values of We. When the cavity pinches off at a small depth from the initial liquid pool surface it is called shallow seal. In the case of deep seal, the cavity pinch-off takes place at a greater depth, approximately halfway between the pool surface and the base of the cavity. During surface seal, the cavity pinch-off takes place at the surface of the pool. With the increase in We, the transition of the pinch-off regime from shallow seal to deep seal and finally surface seal was observed. However, in the case of the impact of the microdrop train, no such transition has been observed, although we have covered a wide range of We. This can be seen in Fig. 5.14(a) where the circles represent the data of solid sphere impact [105] and the line represents the data of microdrop train impact. A transition from the deep seal to surface seal was observed near $We = 600$ ($We = 300$ in Aristoff and Bush [105] as We was defined based on sphere radius) during the impact of solid spheres as seen in Fig. 5.14(a). However, in the case of the impact of microdrops, the pinch-off depth initially increases by a small amount and remains almost constant. The pinch-off

depth increases with increased We because of the higher momentum transferred to the pool which exerts more downward pull on the surface of the cavity. However, with further increase in We the downward pull is not able to increase the depth of the necking region and a constant pinch-off depth is observed.

The pinch-off depth increases with the increase in train length in the shallow cavity regime as depicted in Fig. 5.14(b). In the deep cavity regime, initially the pinch-off depth increases with the increase in $\tilde{L_t}$ by a small amount and becomes constant for larger values of $\tilde{L_t}$. In the shallow cavity regime, with the increase in $\tilde{L_t}$ more capillary waves propagate through the interface owing to the effect of continuous impact of the drops on the base of the cavity. These waves merge with the largest amplitude wave crest close to the neck continuously and bring it deeper inside the pool leading to greater pinch-off depth. Moreover, because of the momentum transferred to the pool during the impact of drops, a downward axial pull continuously act on the cavity surface. With the increase in $\tilde{L_t}$, owing to the continuous impact of the drops the vertical pull continuously act which leads the neck to merge at a greater depth. As a result, the pinch-off depth continuously increases. This effect is also seen at the initial stage of deep cavity regime, where the pinch-off depth increases with the increase in $\tilde{L_t}$ as seen in Fig. 5.14(b). At larger values of $\tilde{L_t}$, the cavity depth becomes large. The propagating capillary waves travel a longer distance to reach the neck region and are damped by viscosity before they reach the neck region. Furthermore, at larger values of $\tilde{L_t}$ the neck merges before all the droplets hit the cavity base and the pinch-off depth does not change with further increase in $\tilde{L_t}$.

Figure 5.15 shows the change of neck radius of the cavity with time for deep and shallow cavities at different We. Initially, when the drops impact the liquid pool, the cavity mouth expands very rapidly, and a very sharp increase of neck radius can be observed (Fig. 5.15 (a)). This is because, large momentum of the impacting microdrops is completely transferred to the pool upon impact. The momentum gets diffused in the pool, which results in expansion of the cavity. The complete diffusion of momentum is brought about gradually by the reduced rate of expansion. Due to the propagation of disturbances from the cavity base to the cavity mouth, the radial expansion of the cavity mouth continues to increase at a slower rate. The widening of the cavity is brought about by the diffusion of the vertical momentum. Once the cavity reaches a certain depth, the transfer of the impacting momentum form the cavity base to the cavity mouth reduces and the cavity mouth starts retracting. The

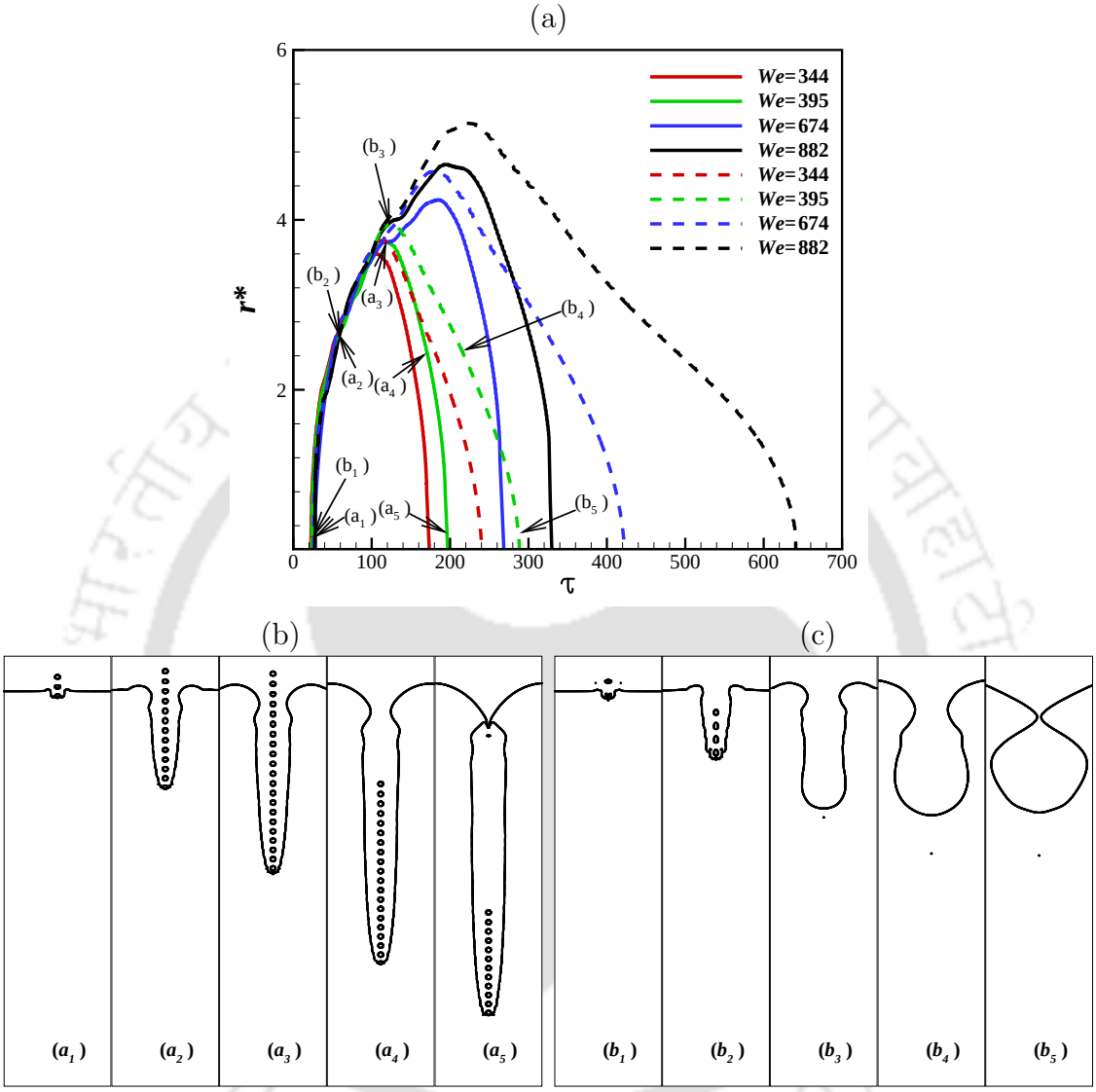

Figure 5.15: (a) Temporal variation of non-dimensional neck radius (r^*) of the cavity at different We. The solid lines indicated neck radius variation during the impact of a long drop train ($\tilde{L}_t = 127.1 - 202.4$) which forms a deep cavity. The dashed lines indicated the neck radius variation during the impact of a short drop train ($\tilde{L}_t = 25.86 - 41.37$) which forms a shallow cavity. (b) The corresponding cavity profiles at instants (a_1)-(a_5) for $We = 395$, in the case of a deep cavity ($\tilde{L}_t = 136.05$). (c) The corresponding cavity profiles at instants (b_1)-(b_5) for $We = 395$, in the case of a shallow cavity ($\tilde{L}_t = 27.67$). The other non−dimensional parameters are $Re = 1000 - 1600$, $Fr = 15.9 \times 10^5 - 40.7 \times 10^5$.

capillary waves enhance the neck retraction process and the neck radius decreases continuously. During the decrement period, the decrement is initially slow and the rate increases continuously. Finally, a sharp decrease in neck radius takes place and the cavity closes at the central axis. This change of neck radius with time can be represented by an approximate power law relation between neck radius (r) and time (t) of the type $r \sim t^n$. We used curve fitting technique to find the value of the exponent n. It has been found that during the expansion stage of the cavity mouth, the value of the exponent n is $n = 0.38 \pm 0.03$, which is same for both shallow and deep cavities. During the collapse stage, for the ease of analysis, the power law expression is slightly modified, given as, $r \sim (t_p - t)^n$, where t_p is the pinch-off time. In the case of a deep cavity, the value of the exponent n has been found as $n = 0.48 \pm 0.03$. However, in the case of a shallow cavity, a prolonged collapse period is observed as compared to that of a deep cavity (Fig. 5.15(a)). Here, the value of the exponent n has been found as $n = 0.53 \pm 0.03$. Figure 5.16 shows this variation of r with $(t_p - t)$ during the collapse stage of the cavity. The maximum percentage deviation between the observed values of r and the curve-fitted power law function of r calculated using specific values of the exponent n are approximately 5% for a shallow cavity and approximately 6% for a deep cavity. The difference in the values of the scaling exponents for shallow and deep cavities is attributed to the change in duration of the collapse period owing to the effect of capillary waves.

Burton et al. [114] used ultra-high-speed video imaging for experimental studies on the pinch-off of gas bubbles from a nozzle in liquids with a wide range of liquid viscosity. They predicted the pinch-off of gas bubbles in liquids using Rayleigh-Plesset equation [115] and observed three regimes of bubble pinch-off depending on the liquid viscosity. They observed that the radius of the neck decreases in time as a power law with an exponent of 1/2 for low viscosity liquid ($\mu_1 < 10$ cP), such as water and an exponent of 1 for the viscous liquid ($\mu_1 > 100$ cP). Our results have shown good agreement with the previous observations [114, 116] of single bubble pinch-off. The slight difference is observed because of the capillary wave effect owing to the continuous impact of drops. The deviation from the ideal value 1/2, predicted from Rayleigh-Plesset theory, was also reported earlier by Bergmann et al. [81] during the pinch-off of a giant bubble formed by the rapid pulling of a disk through a liquid. However, there is a substantial difference between the pinch-off of the cavity formed by microdrop impact with that of the experiments of Bergmann et al. [81], where the hydrostatic effect was dominant because of the large size of the cavity.

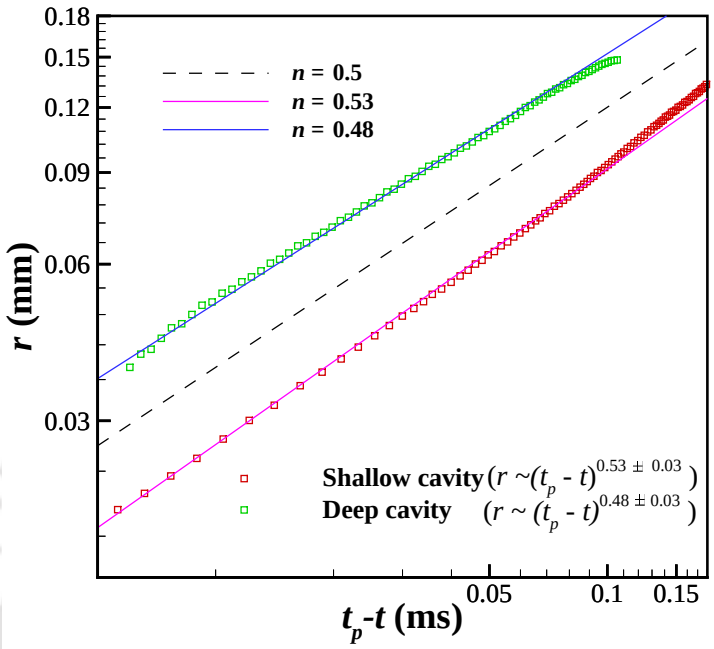

Figure 5.16: The variation of minimum neck radius of the cavity with $t_p - t$ during the collapse stage of the cavity. Two drop trains are considered, one having $\tilde{L}_t = 27.67$ which forms a shallow cavity, and the other having $\tilde{L}_t = 136.05$ which forms a deep cavity. The other non-dimensional parameters are $Re = 1070$, $Fr = 18.2 \times 10^5$ and $We = 395$.

The radial velocity of the neck can be calculated as,

$$u_r = \frac{dr}{dt}, \tag{5.6}$$

which finally leads to

$$u_r \sim r^{\frac{n-1}{n}}. \tag{5.7}$$

Here, the value of n has been found to be less than unity, and hence Eq. 5.7 signifies that the radial velocity near the neck increases as r decreases. This increase in velocity has been discerned at the beginning of the expansion stage and towards the end of collapse stage.

The maximum radial expansion of the neck of the cavity increases with the increase in Weber number, which also increases the pinch-off time. However, the temporal variation of the neck radius in each stage shows the same trend for various Weber numbers as shown in Fig. 5.15.

The pinch-off of a liquid drop is a prime example of a hydrodynamic singularity

and has been studied extensively [107, 117, 118]. During the pinch-off of drops, the pinch-off is independent of the initial conditions and any external forcing, and thus evolves self-similarly in time. Similar to the pinch-off of drops, the bubble pinch-off is also self-similar with a variation of exponents depending on the properties of the fluids [114, 119]. Bergmann et al. [81] reported that the self-similarity during bubble pinch-off holds only in the asymptotic regime of very large Froude number. In the present investigation, the range of Froude number is large and we expect self-similarity to persist during the cavity collapse.

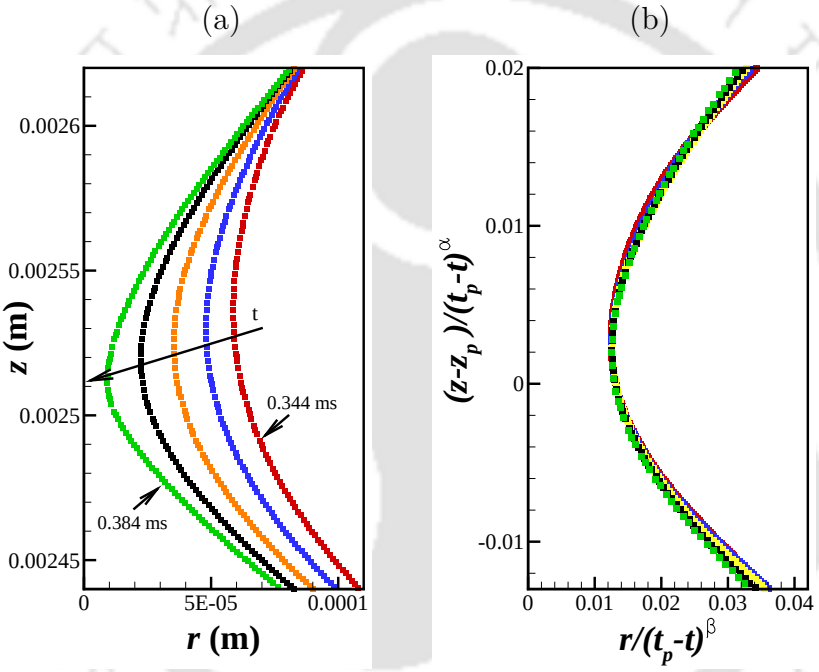

Figure 5.17: (a) The variation of the neck profile during the collapse of a shallow cavity. The different curves correspond to different times. The non-dimensional parameters are $\tilde{L}_t = 27.67$, $We = 395$, $Fr = 18.2 \times 10^5$ and $Re = 1070$. (b) The same profiles showed on the left hand side collapse into a single profile after the use of similarity scaling. The radial coordinate r is scaled as $r/(t_p - t)^\beta$ and the axial coordinate z is scaled as $(z - z_p)/(t_p - t)^\alpha$.

Hogrefe et al. [120] developed a relation for the height (z) of the growing spike for gravity-capillary singular phenomena as a function of radius (r) of the spike and the time (t) of growth, which is given as

$$z(r,t) = at^\alpha (rt^\beta)^\gamma, \tag{5.8}$$

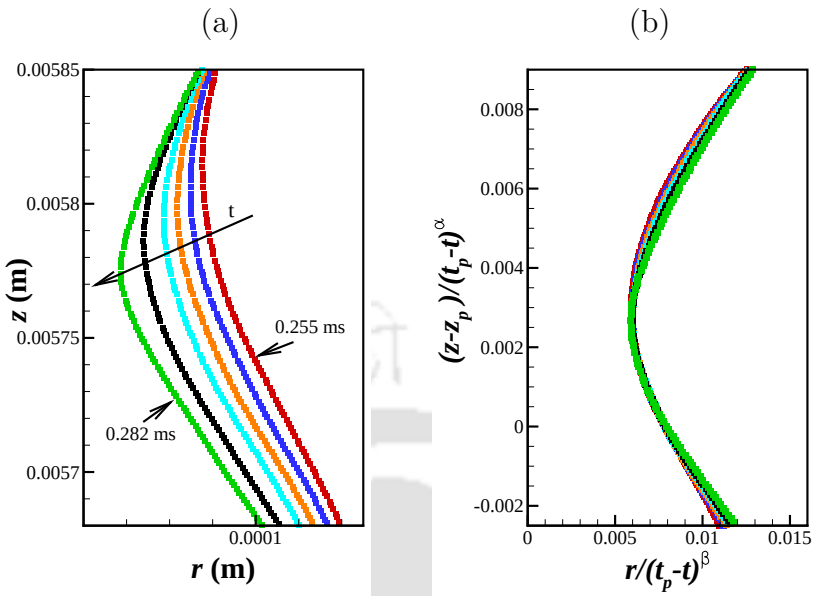

Figure 5.18: (a) The variation of the neck profile during the collapse of a deep cavity. The different curves correspond to different time instants. The non-dimensional parameters are $\tilde{L}_t = 136.05$, $We = 395$, $Fr = 18.2 \times 10^5$ and $Re = 1070$. (b) The same profiles showed on the left hand side collapse into a single profile after the use of similarity scaling. The radial coordinate r is scaled as $r/(t_p - t)^\beta$ and the axial coordinate z is scaled as $(z - z_p)/(t_p - t)^\alpha$.

where a, α, β and γ are constants. The collapse of the cavity formed by the impact of microdrops is an inertia-capillary dominant phenomenon. Earlier investigations on drop and bubble pinch-off [114, 117–119] show that the pinching region shows self similarity as a function of time until pinch-off $(t_p - t)$. We performed the self-similarity analysis for the cavity neck profile near the pinching region. The fitting function we used is of the form

$$\frac{z - z_p}{(t_p - t)^\alpha} = \frac{ar}{(t_p - t)^\beta}. \tag{5.9}$$

Here, the radial coordinate r is scaled as $r/(t_p - t)^\beta$ and the axial coordinate z is scaled as $(z - z_p)/(t_p - t)^\alpha$. Here, z_p is the axial location of the point where neck merges during pinch-off. We observed that the profiles at different time instants superimpose into a single profile after rescaling, as depicted in Fig. 5.17 and Fig. 5.18. In the case of a shallow cavity, the values of the exponents α and β have been found as 0.87 and 0.53, respectively. In the case of a deep cavity, there is a

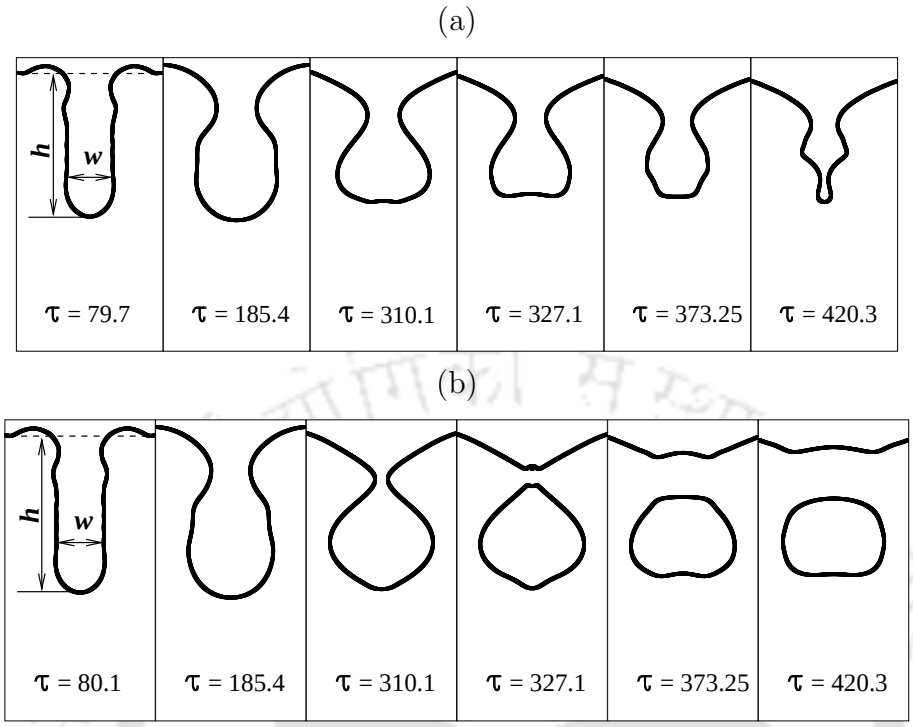

Figure 5.19: Cavity profiles after the impact of microdrop trains of water having (a) 12 drops ($\tilde{L}_t = 25.37$) and (b) 13 drops ($\tilde{L}_t = 27.67$) at different instants of time. In both the cases the drop diameter is 40 μm and the impact velocity is 26.75 m/s. The non-dimensional parameters are $We = 395$, $Fr = 18.2 \times 10^5$ and $Re = 1070$.

continuous propagation of capillary wave because of continuous impact of drops. In the case of a deep cavity, the values of the exponents α and β are 0.85 and 0.48, respectively. There is a clear collapse of the data as depicted in Fig. 5.17(b) and Fig. 5.18(b).

5.4.4 Criteria for pinch-off

The entrapment of the bubbles does not always take place upon drop impact on a pool. Bick et al. [121] concluded that the crater depth must exceed the critical crater depth for bubble entrapment. They studied bubble formation owing to the impact of multiple drops of millimeter size, having comparatively lower velocity. Essentially bubble formation does not take place if $h/l_c \ll 1$, where h is the cavity depth and l_c is the capillary length scale given by $l_c = \sqrt{\sigma/\rho g}$. Figures 5.19 (a) and (b) show the cavity profile owing to the impact of trains of 12 and 13 drops, having $\tilde{L}_t = 25.37$ and $\tilde{L}_t = 27.67$ respectively. In the case of a train of $\tilde{L}_t = 25.37$, the pinch-off does not take place even though the necking takes place and the cavity reaches the onset

of pinch-off. In the case of a train of $\tilde{L}_t = 27.67$, we observe the pinch-off to take place. In order to estimate the optimum $\tilde{L}_t$ for which the pinch-off takes place, we simulated different cases for different Weber numbers (We), as shown in Fig. 5.20. In Fig. 5.20, the red squares indicate the points where pinch-off took place and the dark circles indicate the points for which the cavity collapses without pinch-off.

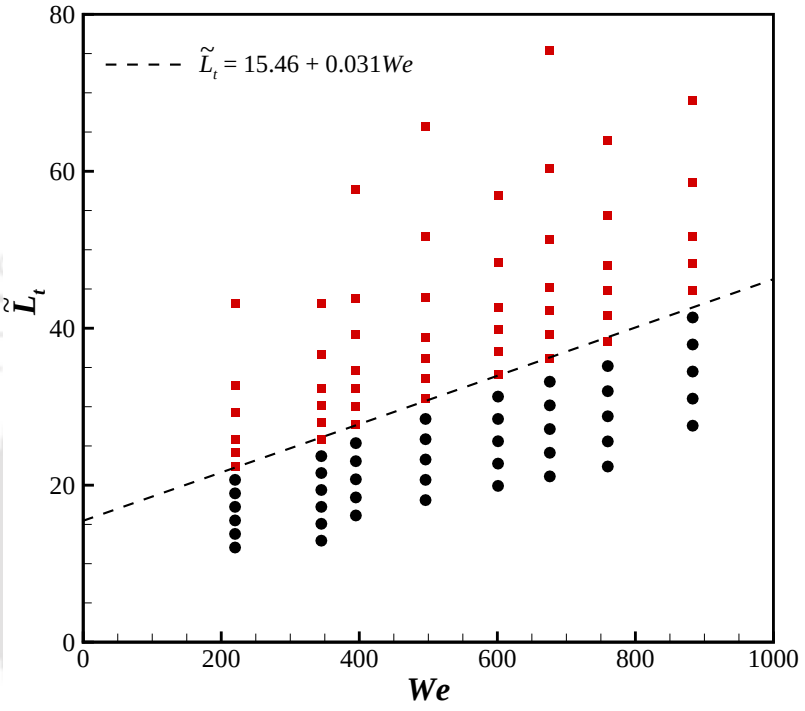

Figure 5.20: The $\tilde{L}_t$-We plot, showing the transition from no-pinch-off to pinch-off regime. The red squares indicate the points where pinch-off took place and the black circles indicate the points where pinch-off is suppressed. The other non-dimensional parameters are $Re = 600 - 2000$, $Fr = 8.15 \times 10^5 - 54.0 \times 10^5$.

In the case of the impact of high-speed microdrops on a liquid pool, the capillary forces contribute to the dynamics of collapse of the cavity. It may be noted that the collapse of the cavity mentioned above, is primarily surface tension driven collapse [103]. Aristoff and Bush [105] predicted the pinch-off time considering a balance between inertia force and surface tension force that eventually culminated in cavity collapse based on the maximum radius of the cavity as $t_p \sim \sqrt{\rho R_c^3/\sigma}$, where R_c is the maximum radial extent of the cavity. Bouwhuis et al. [103] solved the Young-Laplace equation and predicted the maximum radius of the cavity as $R_c \sim RWe_m$, where We_m is the modified Weber number defined as $We_m = \rho V_c^2 R/\sigma$. Here V_c is the penetration velocity of the cavity. In continuation, they also predicted the depth

of the cavity at the time of pinch-off as $h_p \sim RWe_m^2$. It has been observed that both penetration depth of the cavity and the radial expansion of the cavity are important parameters indicating pinch-off of the cavity. The critical $\tilde{L}_t$ has been observed when the value of h/w is close to 3, where w is the average diameter of the undeformed cavity. By undeformed cavity, we mean that the cavity shape is almost cylindrical, such as the first profiles of Fig. 5.19 (a) and Fig. 5.19 (b). Likewise, h is the depth of the undeformed cavity from the free surface of the liquid pool. The corresponding values of h and w are 0.771 mm and 0.266 mm in Fig. 5.19(a) and 0.814 mm and 0.266 mm in Fig. 5.19(b), respectively. For $\tilde{L}_t$ below this critical value, the pinch-off of the cavity does not take place, even if the necking starts and reaches the onset of pinch-off. Instead, the cavity shrinks continuously and finally collapses forming an upward jet, similar to the collapse of the crater formed by millimeter-sized drops as reported by Rein [77]. The critical $\tilde{L}_t$ for pinch-off increases with the increase in We, as seen in Fig. 5.20. This is because the radial expansion of the cavity increases with the increase in We and to reach the h/w ratio close to 3, larger $\tilde{L}_t$ is needed. From the simulated data, we obtain the correlation for the variation critical $\tilde{L}_t$ with We as $\tilde{L}_t = 15.46 + 0.031We$.

5.5 Summary

The present investigations have focused on the cavity dynamics during the impact of a high-speed train of microdrops on a deep liquid pool. The impact of a high-speed train of microdrops creates a deep slender tongue shaped cavity. The capillary waves emerge from the base of the cavity and propagate along the cavity wall. These capillary waves converge near the cavity mouth and expedite the necking. The variations of different pertinent parameters, such as penetration depth, penetration velocity, pinch-off time, pinch-off depth have been investigated in detail. The motion of the cavity mouth can be demarcated into an expansion stage and a collapse stage. The radial movement of the neck shows power law behavior in both expansion stage and collapse stage. In the pinching region, the phenomenon of cavity collapse is self-similar in nature. The critical train length for pinch-off increases with the increase in We. Current investigation reveals that pinch-off occurs only when the penetration depth of the cavity becomes greater than three times the average diameter of the cavity.

Chapter 6

Coalescence dynamics of unequal sized drops

6.1 Introduction

The interaction and coalescence of drops in a flow have been the subject of research due to their fundamental importance in a variety of multiphase flow systems. After the pioneering work of Worthington [1], drop coalescence attracted attention of many researchers because of the complex nature of the underlying phenomena. Later on, several investigations [4, 79, 122–126] were reported on coalescence of a drop. Consequently, different regimes of drop coalescence have been identified. It has also been unveiled that depending on the impact condition, the drop may either coalesce with the receiving liquid or it may splash. The coalescence may be partial with the formation of a secondary drop or may be complete. In addition, the drop may also bounce off or float on the liquid surface [127–130].

When a drop comes in contact with a surface, it floats on the interface for a small duration. The film between the drop and the interface becomes thinner and thinner, and finally ruptures to create an aperture. Through this aperture, some liquid from the drop drains out to the pool unless the neck closes to form a secondary drop. The phenomenon of formation of the secondary drop and the subsequent smaller drops is known as partial coalescence. The secondary drop is also called satellite drop or daughter drop. Partial coalescence can result in a cascade of self-similar events [125], bearing far reaching implications in a variety of natural and

engineering processes such as the rain formation in clouds [131], ocean mist, and airborne salt particles [132], coarsening of emulsions [133] and vortex generation near an interface [134, 135], to name a few. Moreover, it plays an important role in liquid/liquid separation, efficiency of separator or mixing vessels, as well as mixing processes in microfluidic devices.

Charles and Mason [123], from their experimental investigation, reported that partial coalescence results from the formation of a liquid column which contracts at the base and detaches itself to form the secondary drop owing to Rayleigh instability. A theoretical explanation was also provided by them using the theory of Rayleigh [136], regarding the breakup of the liquid column and formation of a secondary drop. Schotland [124] reported that partial coalescence occurred only at a lower impact velocity of the drop. Pikhitsa and Tsargorodskaya [137] suggested that the existence of the monolayer surfactant film is crucial for the multistage coalescence of a drop on an air-liquid interface. The drop rests on the interface for a finite time because of this thin film layer of the surrounding fluid. After a finite time, the surrounding fluid drains out, owing to the weight of the drop and this layer becomes thin enough for coalescence to occur [126, 134, 138].

Honey and Kavehpour [138] suggested that the capillary force is the main driving force for the partial coalescence and coalescence-induced bouncing of drops. Chen et al. [139] reported that partial coalescence is governed primarily by inertia and interfacial tension. Further, they delineated three regimes of partial coalescence based on the roles of viscosity and gravity. The three regimes are gravity regime, inertio-capillary regime, and viscous regime. At higher values of Bond number ($Bo = (\rho_1 - \rho_2)gD^2/\sigma$), the coalescence phenomenon is driven by gravity and at lower values of the Bond number, the viscous effect becomes dominant. At intermediate values of Bond number, the phenomenon is driven by inertia and capillary force. Here, D is the drop diameter, g is the acceleration due to gravity, σ is the surface tension coefficient, and, ρ_1 and ρ_2 are the densities of the drop fluid and the surrounding fluid respectively. Partial coalescence is mainly observed in the inertio-capillary regime. The capillary waves move through the interface of the drops, converge at the apex of the drop, and exert an upward pull [108, 140]. Because of this upward pull, the drop forms a columnar structure and finally pinches off which leads to the formation of a secondary drop. The occurrence of pinch-off is determined by a competition between the vertical and horizontal collapse rate of the connected drop. When the vertical collapse is sufficiently delayed by the converging capillary

waves, the horizontal collapse succeeds in pinching off the neck and producing a daughter drop. Increased viscosity retards the capillary wave movement, and thus minimizes the upward vertical pull which finally leads to complete coalescence. The effect of physical properties of the fluids on the system characteristics and the effect of external electric field on the coalescence process are thoroughly reviewed by Kavehpour [141].

The coalescence of two drops is very common in two-phase flows. Similar to the coalescence of a drop on a flat liquid pool, during the coalescence of two drops, the interfaces of the two drops approach each other by squeezing out the thin film of the suspending fluid in between them. Coalescence takes place only when the clearance distance between the two drop interfaces is smaller than a certain critical value [142–145]. This critical value is equal to the molecular interaction range, typically of the order of 10^{-8} m [146]. Several investigations [147–151] have been performed to understand the film drainage during the impact of drops. Bouncing takes place when the thickness of the surrounding fluid film trapped between the two drops is larger than this minimum clearance distance. The motion following contact is driven by surface tension and the mixing between the two drops is a process of dissipation of excess surface energy [152–155]. Many investigations have been executed to elucidate the coalescence dynamics and two distinct regimes of coalescence have been observed, namely the viscous regime and the inertial regime [153, 156, 157]. In the viscous regime, the neck radius R linearly grows with time ($R \propto t$) [156, 158, 159] and in the inertial regime it grows as square root of time ($R \propto \sqrt{t}$) [156, 160, 161]. At the initial stage, the coalescence dynamics is always dominated by the viscosity of the drop fluid [162].

Thoroddsen et al. [159] experimentally studied the coalescence of a pendant and a sessile drop, to analyze the coalescence dynamics. They proposed a dynamic inertia-capillary model based on the vertical spacing between the two drops surfaces to describe the outward motion of the contact region for low viscosity liquids. The unbalanced surface tension force across the neck region makes the coalescence very fast. The coalescence speed is slowed down by increased viscosity of fluids [158, 159]. When the two drops are of different liquids, their coalescence speed is governed by the liquid having the weaker surface tension [116]. However, these studies were solely focused on the coalescence, rather than satellite formation.

The satellite production during the coalescence of drops is a fascinating process and the resulting drop size distribution is of direct importance in a wide variety of

industrial applications. Blanchette and Bigioni [140] speculated that the diameter ratio of the two drops must be larger than 2, for the generation of daughter drops during coalescence of two drops of dissimilar size. However, later on, the same authors reported that partial coalescence can be observed even up to a minimum diameter ratio of approximately 1.6 [163]. Zhang et al. [164], from their experimental observations, reported that the critical size ratio of two water drops in an air medium, above which a satellite is pinched off during their coalescence is around 1.55. The critical size ratio increases monotonically with the increase in Ohnesorge number (Oh). They defined Ohnesorge number based on the radius of the mother drop as $Oh = \mu_1/\sqrt{\rho_1 \sigma R_m}$, where R_m is the radius of the mother drop and μ_1 is the viscosity of the drop liquid. The mother drop is the smaller drop at the top and the bigger drop at the bottom is called the father drop.

Although the satellite drop formation has been widely studied for the case of a drop interacting with a flat surface, the spatio-temporal events concerning the dynamical evolution of the coalescence of two unequal sized drops remain far from being comprehensively addressed. Earlier investigations [140,163,164] reported that there exists a critical diameter ratio below which satellite formation is inhibited. However, why does the satellite formation is inhibited under such conditions is still not addressed. In the current investigation, we have attempted to numerically simulate the coalescence of two drops and the inherent processes using the CLSVOF method to understand the underlying physics. The present investigation consists of a numerical study on the identification of various coalescence events, with emphasis on the conditions and mechanisms leading to partial coalescence and generation of secondary drops during the coalescence of two unequal sized drops. The critical values of appropriate non-dimensional parameters for which transition from complete coalescence to partial coalescence occurs have been explored.

6.2 Formulation

6.2.1 Computational domain

A representative diagram of the computational domain is shown in Fig. 6.1. An axisymmetric coordinate system (r, z) is used to model the flow dynamics, where r and z represent the radial and axial coordinates, respectively. In the numerical sim-

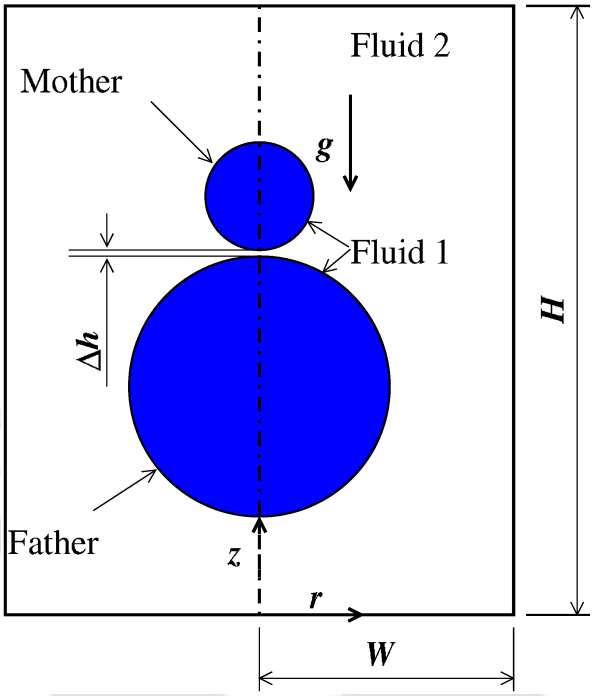

Figure 6.1: Computational domain used in numerically simulations of coalescence of two unequal sized drops. Depending on the size ratio of the father and mother drops (D_f/D_m), the width of the domain is varied in the range $W = 4D_m - 20D_m$ and the height of the domain is varied in the range $H = 10D_m - 50D_m$. The mother drop is initialized at a height of $\Delta h = 0.01D_m$ above the father drop.

ulations, we have initialized the two drops vertically one above the other. Following the conventional notation reported in Zhang et al. [164], the lower drop is called the father drop and the upper drop is called the mother drop. The two drops are separated by a very small gap ($\approx 0.01D_m$) such that the coalescence is unaffected by the gap between the two drops. Here, D_m is the diameter of the mother drop. The liquid of the father drop and the mother drop is same (Fluid 1), which coalesce on a surrounding medium (Fluid 2). The initial velocity of the father drop is considered to be zero. In order to initiate the coalescence, the mother drop is initialized with a very small velocity ($\approx 5 \times 10^{-3}$ m/s). The velocity is considered to be very small such that the coalescence dynamics is not affected by this initial velocity. After few time steps, the mother drop comes in contact with the father drop and initiates the coalescence. Depending on the diameter ratio of the father and mother drops (D_f/D_m), the width of the domain is varied in the range $W = 4D_m - 20D_m$ and the height of the domain is varied in the range $H = 10D_m - 50D_m$.

6.2.2 Boundary conditions

Here, we have performed axisymmetric simulations and the axis of symmetry lies on the left boundary. At the axis of symmetry, no fluid exits or enters the domain. This can be mathematically expressed in terms of the respective velocity components (u, v) along the radial and axial directions as

$$u = 0, \quad \frac{\partial v}{\partial r} = 0. \tag{6.1}$$

The same boundary conditions can be applied on the right boundary as the right boundary is considered to be frictionless.

On the bottom wall, we deploy the no-slip boundary condition and the impermeability condition as

$$u = v = 0. \tag{6.2}$$

At the top boundary the natural Neumann boundary condition is applicable.

$$\frac{\partial u}{\partial z} = \frac{\partial v}{\partial z} = 0 \tag{6.3}$$

The Neumann pressure boundary condition is applied in all the boundaries, except at the top boundary where pressure is equal to the atmospheric pressure P_{atm}.

6.2.3 Scaling analysis

The coalescence behavior of a drop is governed by the interfacial tension, gravity and the viscosity of the drop and the surrounding fluid. The dimensional analysis of Gilet et al. [165] and Ray et al. [108] show that the partial coalescence of a drop onto a liquid pool can be described by four dimensionless parameters. The relevant non-dimensional parameters are Bond number, $Bo = \rho_c g D_m^2/\sigma$, the Ohnesorge numbers, $Oh_1 = \mu_1/\sqrt{\rho_a \sigma D_m}$ and $Oh_2 = \mu_2/\sqrt{\rho_a \sigma D_m}$ and the Atwood number $A = \rho_c/2\rho_a$. Here, ρ_1, ρ_2 are the densities and μ_1, μ_2 are the dynamic viscosities of the drop fluid and the surrounding fluid, respectively. $\rho_a = (\rho_1+\rho_2)/2$ is the average density and $\rho_c = \rho_1 - \rho_2$ is the density difference between the two fluids. In the case of coalescence of two drops, the same non-dimensional parameters govern the coalescence behavior

along with one additional parameter, which is the diameter ratio of the father and the mother drop, D_f/D_m. The non-dimensional parameters pertinent to the present investigation are Bond number, $Bo = \rho_c g D_m^2/\sigma$, the Ohnesorge numbers, $Oh_1 = \mu_1/\sqrt{\rho_a \sigma D_m}$ and $Oh_2 = \mu_2/\sqrt{\rho_a \sigma D_m}$, the Atwood number $A = \rho_c/2\rho_a$ and the diameter ratio of the father and the mother drop, D_f/D_m. The length scales are non-dimensionalized using the mother drop diameter D_m, and the time is scaled by capillary time, $\tau_c = \sqrt{\rho_a D_m^3/\sigma}$.

6.3 Validation and grid-independent test

In order to validate the efficacy of the code in capturing the coalescence of two drops, the code is tested rigorously and validated with experimental results which shows excellent agreement. Zhang et al. [164] investigated the satellite formation during the coalescence of two unequal sized vertically aligned drops. Initially, the upper drop rests on the interface of the lower drop for a small duration until the film between the two drop ruptures. The breakup of the thin air film between the two

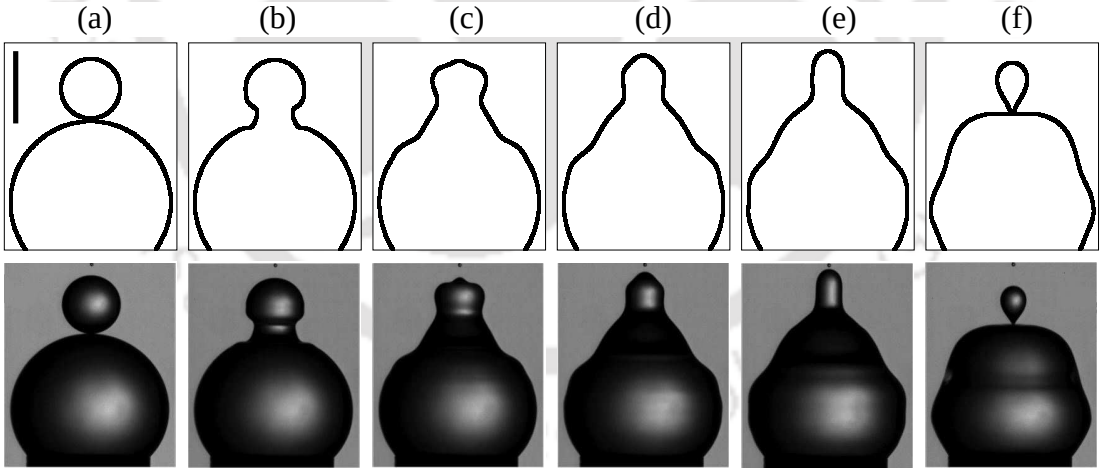

Figure 6.2: Comparison between the numerical results of present investigation and the experimental result of Zhang et al. [164], for the partial coalescence of two unequal sized drops with $D_f/D_m = 2.72$. The drop liquid is water and the surrounding is air. The first row shows the profiles observed in our numerical investigation and the second row is the experimental results of Zhang et al. [164]. The profiles, (a)-(f), are shown at 0.0 ms, 0.27 ms, 0.67 ms, 0.93 ms, 1.2 ms and 1.8 ms respectively. The scale bar is 1 mm long. The non-dimensional parameters are $Oh_1 = 0.0058$, $Oh_2 = 0.000116$, $A = 0.997$, and $Bo = 0.092$.

Table 6.1: Comparison between the numerical results obtained using different mesh resolution. The non-dimensional parameters are same as mentioned in Fig. 6.2.

Grid-mesh	D_d/D_m	Percentage change (%)
120×240	0.557	–
150×300	0.546	2
200×400	0.542	0.75
300×600	0.542	0.0

drops creates an aperture, through which some liquid of the mother drop drains out and mixes with the father drop. After a certain time, it forms a columnar structure which gradually becomes thin and sets necking at its base. Finally, the neck pinches off, which results in the formation of a secondary drop or daughter drop. Figure 6.2 shows the coalescence sequence of two drops of unequal size, having a diameter ratio of the father and the mother drop, $D_f/D_m = 2.72$. The drop liquid is distilled water and the surrounding fluid is air. In Fig. 6.2, the first row is the results obtained from the numerical simulations. The second row is the experimental results of Zhang et al. [164]. The results of numerical simulations have shown an excellent agreement with the experimental results of Zhang et al. [164], as evident in Fig. 6.2.

In order to reveal grid independence, a sample grid independence study was performed using the same parameters as mentioned in Fig. 6.2 with different mesh resolution. We considered four different grid-meshes and calculated the diameter ratios of the daughter drop to that of the mother drop (D_d/D_m) for each grid-mesh, which are presented in Table 6.1. The percentage difference for the grid-meshes of size 120×240 and 150×300 is around 2%, while for the grid-meshes of 150×300 and 200×400 is nearly 0.75%. The results for the grid-meshes of 200×400 and 300×600 are same. The results due to a mesh size of 200×400 are considered to be grid independent results. Likewise, all the results presented in this study are grid independent.

6.4 Results and discussion

The coalescence of a drop with a flat liquid surface pinches off a satellite from its top, which is a well-known coalescence cascade phenomenon. Such cascade of coalescence can be observed during the coalescence of two unequal sized drops. However, the coalescence mechanism has many distinctive features, different from the coalescence

of a drop onto a pool.

6.4.1 Coalescence speed

When the two liquid drops approach each other, van der Walls forces join the two drops together and form a tiny liquid bridge [160]. The drops then coalesce rapidly, owing to the large curvature and unbalanced surface-tension forces in the contact region. Thoroddsen et al. [159] modeled the outward motion of the neck by balancing the dynamic pressure ρu^2 and the capillary pressure σk. Based on that model, the local outward velocity of the neck can be calculated as

$$u(r) = \frac{dR}{dt} = C\sqrt{\frac{\sigma}{\rho}\left(\frac{1}{\delta} - \frac{1}{R}\right)}, \tag{6.4}$$

where R is the instantaneous radial location of the neck and C is a proportionality constant. δ is the vertical spacing of the two drop surfaces at the instantaneous radial location $R(t)$. The value of δ, as a function of R, was calculated from the static drop shapes. For two spherical drops, δ can be calculated as

$$\delta = R_1 + R_2 - \sqrt{R_1^2 - R^2} - \sqrt{R_2^2 - R^2}. \tag{6.5}$$

In the present investigation, R_1 and R_2 are the radius of the mother and the father drops, respectively. Substituting the value of δ in the above equation, the instantaneous velocity of the neck can be determined as a function of $R(t)$ for different fluid combinations. We compared the instantaneous velocity of the neck calculated from our numerical simulation, with the theoretical prediction of Thoroddsen et al. [159], which has shown an excellent match. Figure 6.3 shows the comparison of the radial velocity of the neck for different combinations of Ohnesorge number. The theoretical prediction of Thoroddsen et al. [159] is represented by the solid line, and the red squares indicated the values obtained from the numerical simulations. The value of the coefficient C is found from best fit to the data. Thoroddsen et al. [159] estimated the value of best fit coefficient C as $C = 0.80 \pm 0.05$ for low viscosity fluids, during the coalescence of a pendant drop and a sessile drop. We observed that during the coalescence of two unequal size drops, the model has given the best fit with the numerical data for $C = 0.75$. The good fit between the model and the numerical data

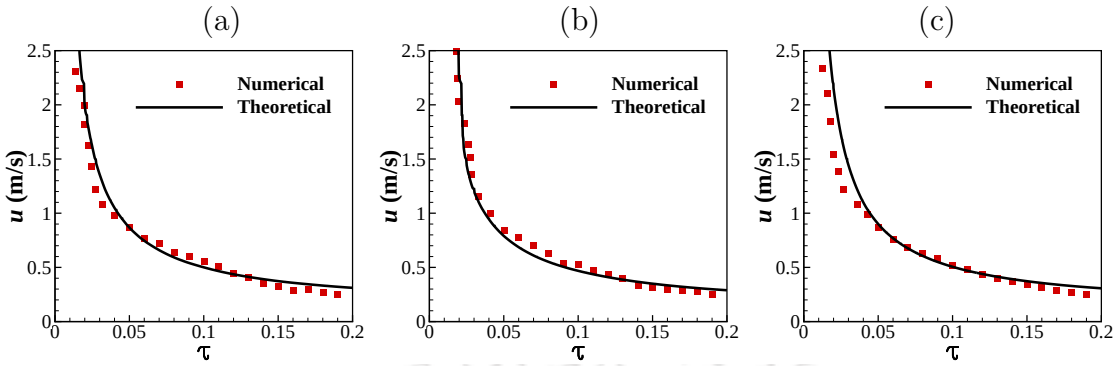

Figure 6.3: The variation of radial velocity of the neck with time for different combination of Ohnesorge number, during the coalescence of two unequal sized drops. In (a) the both the fluids have low viscosity ($Oh_1 = 0.005$ and $Oh_2 = 0.001$), in (b) the liquid viscosity is increased ($Oh_1 = 0.03$) keeping the surrounding fluid viscosity same ($Oh_2 = 0.001$) and (c) shows the variation of radial velocity of the neck when the surrounding fluid viscosity ($Oh_2 = 0.03$) is higher than the drop fluid ($Oh_1 = 0.005$). The theoretical model of Thoroddsen et al. [159] shows a good fit with constant $C = 0.75$. The other dimensionless parameters are $Bo = 0.131$ and $A = 0.8$.

confirms that gravity does not play a significant role in the coalescence dynamics, considering the free fall of the drops. This is because the radial expansion of the neck is much faster than the vertical fall of the drops.

6.4.2 Capillary waves and pinch-off dynamics

Traveling capillary waves have been reported earlier following the work of Blanchette and Bigioni [140] in the context of coalescence of a drop onto a liquid pool, where they reported that the partial coalescence critically depends on the ability of the capillary waves to vertically stretch the drop and delay the vertical collapse. The traveling capillary waves carry momentum along with it. Later on, these propagating capillary waves are studied extensively [107, 108, 116] and it has been observed that the surface tension and the curvature change the pressure in the liquid, because of which traveling capillary wave is engendered. The capillary waves propagate along the interface of the drop and converge at its apex. The converged capillary waves exert a vertical pull and stretch the drop upwards. This upward stretching can be seen in Fig. 6.4, where the dotted line indicates the position of the drop apex at the time of start of the coalescence. Owing to the capillary pull, the drop is stretched

upward and crosses the dotted line, which can be seen at $\tau = 0.66$ and $\tau = 0.82$ of Fig. 6.4.

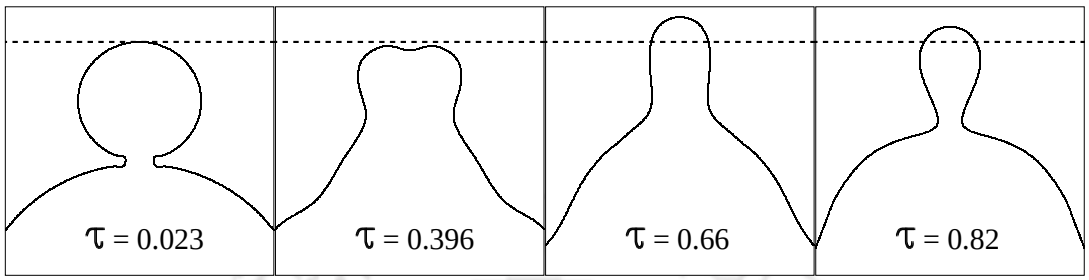

Figure 6.4: The coalescence sequence of two drops at different instants of time. The dotted line represents the position of the mother drop tip at the start of coalescence. The upward pull exerted by the converging capillary waves vertically stretch the drop, which can be seen at $\tau = 0.66$ and $\tau = 0.82$. The dimensionless parameters are $Oh_1 = 0.005$, $Oh_2 = 0.001$, $Bo = 0.131$ and $A = 0.8$.

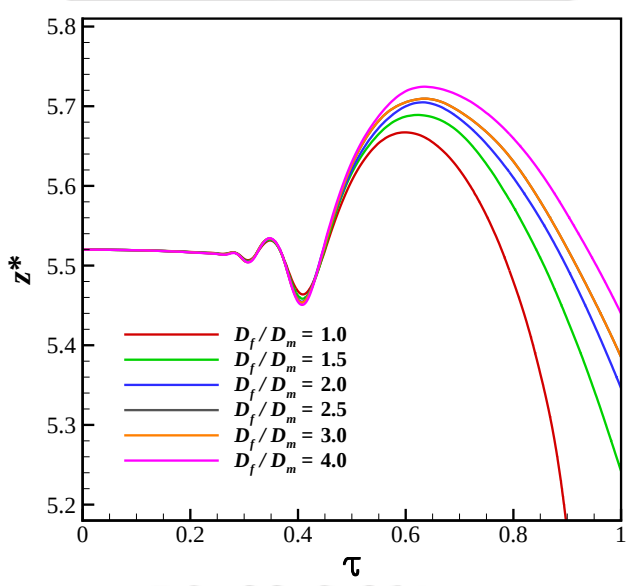

Figure 6.5: The temporal variation of the drop tip for different values of diameter ratio D_f/D_m. The dimensionless parameters are $Oh_1 = 0.005$, $Oh_2 = 0.001$, $Bo = 0.131$ and $A = 0.8$.

Capillary wave is produced by the expanding neck because of the high curvature generated near the contact line. This high curvature is generated at the initial stage of merging and decreases with the expansion of the neck. With the increased value of D_f/D_m, the flatness of the father drop surface increases. Owing to the higher

flatness of the father drop surface, a higher curvature is generated in the contact region. Higher curvature produces stronger capillary waves [166, 167]. This effect of sharpness of the neck region on the generated capillary waves can be seen in Fig. 6.5, where the drop tip position is plotted with time for different values of D_f/D_m. The vertical stretching of the mother drop decreases continuously with the decrease in D_f/D_m because of the decrease in the strength of the propagating capillary waves. This local curvature contributes to the limiting condition of critical diameter ratio, below which satellite formation is inhibited. Earlier, Gilet et al. [165] also observed the similar motion of the drop tip owing to the effect of capillary waves during the coalescence of a drop on a liquid pool. Zhang and Thoroddsen [168] plotted the tip position of a bubble with time during the coalescence of two unequal sized bubbles. They observed higher fluctuation of the bubble tip compared to the coalescence of drops and concluded that during the coalescence of bubbles, several wave crests reach the apex before the daughter bubble is pinched off.

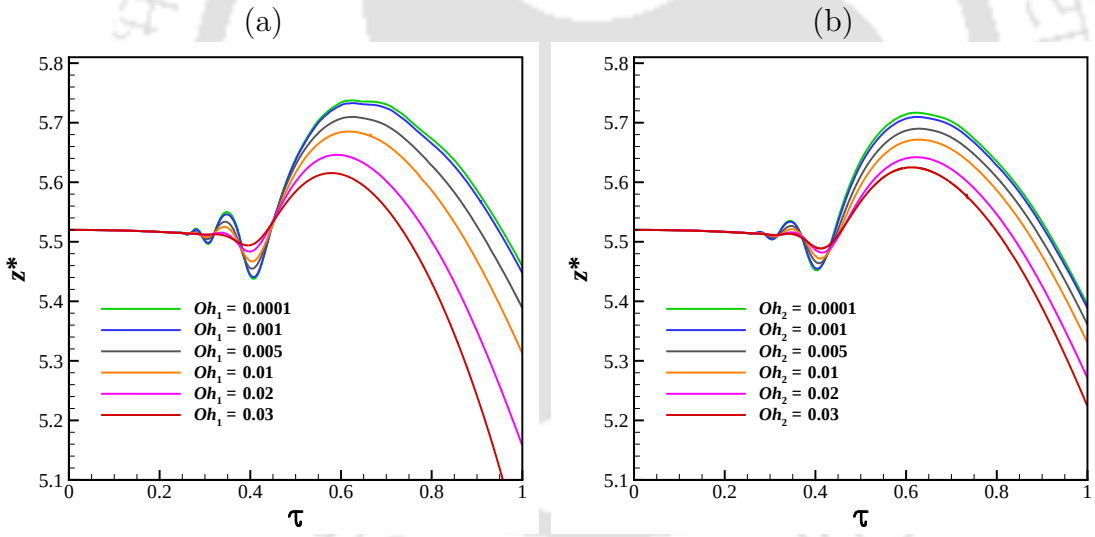

Figure 6.6: The temporal variation of the drop tip for different values of Ohnesorge number. In (a) the drop tip position is plotted for different drop liquid viscosity keeping the surrounding fluid viscosity constant ($Oh_2 = 0.001$) while in (b) surrounding fluid viscosity is varied keeping the drop fluid same ($Oh_1 = 0.005$). The other dimensionless parameters are $Bo = 0.131$ and $A = 0.8$.

The propagation of the capillary wave is damped by viscosity, which reduces the vertical pull on the drop. Moreover, the increased viscosity also reduces the amplitude of the capillary waves, because increased viscosity reduces the curvature change during neck expansion [159]. This viscous damping effect of the capillary

waves can be seen in Fig. 6.6, which shows the position of the upper drop apex with time for different values of Ohnesorge number. In Fig. 6.6(a), the drop tip position is plotted for different values of Oh_1. The increased values of Oh_1 decreases the vertical stretching of the drop, because the propagation of the capillary waves are damped by the increased viscosity of the drop fluid. The same effect is observed when the viscosity of the surrounding fluid is increased, keeping the viscosity of the drop fluid same. This effect of the surrounding fluid viscosity can be observed in Fig. 6.6 (b), which shows the temporal variation of the drop tip for different Oh_2. Both the drop fluid and the surrounding fluid viscosity affect the capillary wave propagation. It has been observed that the propagation speed of the capillary waves is dominated by the high viscosity fluid.

During the coalescence of a drop on a flat liquid pool, capillary waves also travel along the flat interface, away from the point of contact of the drop and the pool interface. The capillary waves traveling along the liquid pool interface have no effect other than deforming the liquid pool interface. In a similar manner, during the coalescence of two unequal sized drops, the capillary waves travel along the interface of the father drop in the downward direction. However, during the coalescence of two unequal sized drops, not only the capillary waves traveling through the interface of the mother drop, but also the waves moving through the interface of the father drop in the downward direction affect the coalescence dynamics. The capillary wave motion through the interface of the father drop is shown in Figures 6.7(a)and 6.8(a). The capillary waves, which travel through the interface of the lower father drop converge at its bottom and impart a downward pull on the interface. The capillary waves pull the drop bottom in the downward direction and stretch it to elongate the drop, in the similar way it pulls the upper drop in the upward direction (and forms the column structure). Similar stretching was observed earlier by Menchaca-Rocha et al. [161] in their experiments of coalescence of two mercury drops. The stretching is more prominent with the decrease in the size of the father drop.

In the case of bigger father drops, the capillary waves need to travel a longer distance to reach the base of the father drops. The capillary wave motion is continuously damped out by viscosity, because of which, the strength of the capillary waves continuously decreases and makes the downward capillary pull weaker. As a result, the deformation of the drop decreases as the size of the drop increases and finally becomes unaffected by the capillary wave motion once it crosses a critical limit.

However, in the case of the smaller father drops, the capillary waves reach the

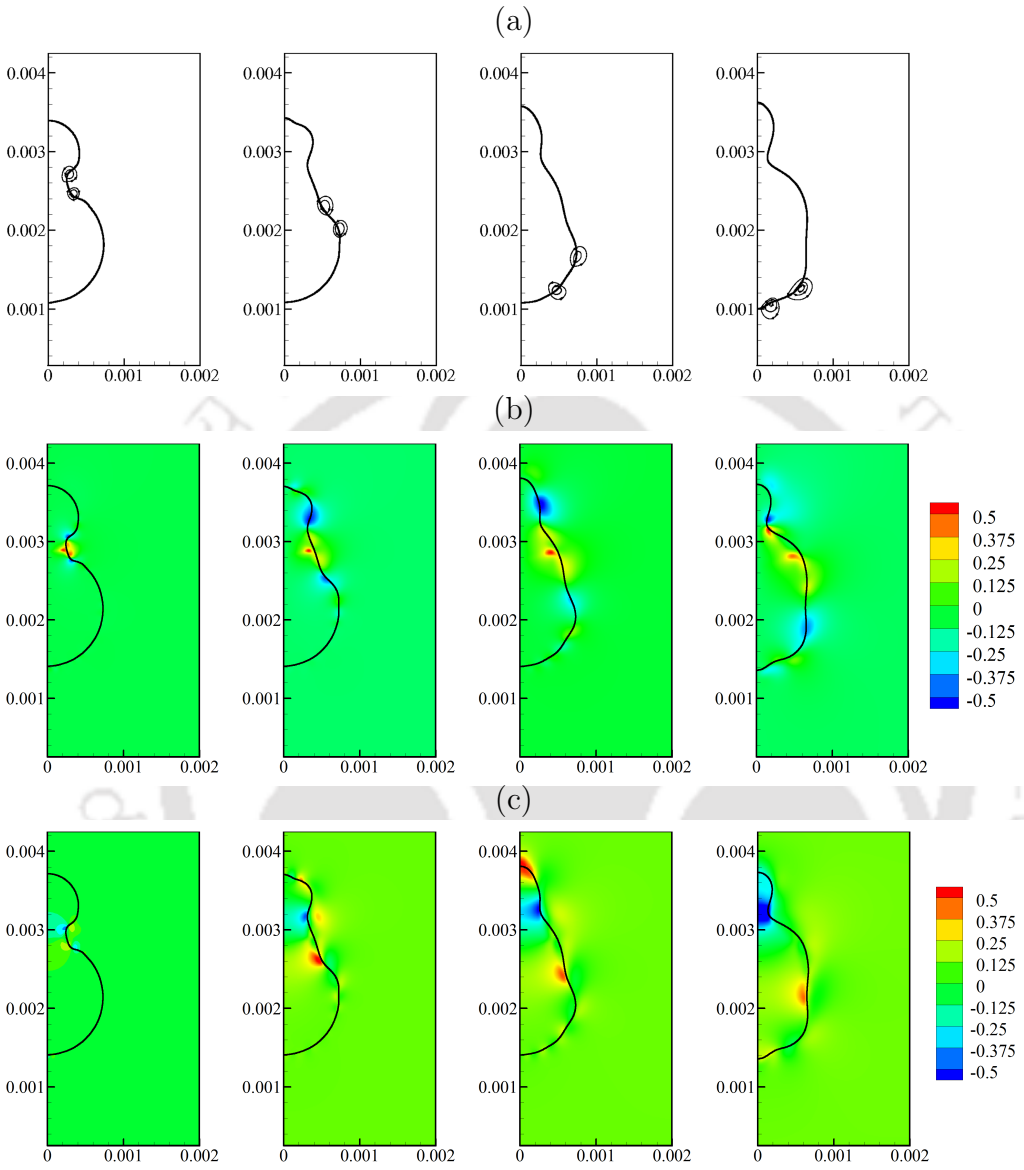

Figure 6.7: (a) The movement of the capillary wave is indicated in the streamline plot, during the coalescence of two drops having diameter ratio $D_f/D_m = 1.8$. The capillary waves reach the bottom of the lower drop before satellite formation and restrict the pinch-off. The profiles from left to right are at time $\tau = 0.16$, 0.36, 0.53 and 0.82 respectively. (b) $u-$velocity and (c) $v-$velocity contour at the same instants of time. The axis labels are in meter. The other non-dimensional parameters are $Oh_1 = 0.005$, $Oh_2 = 0.001$, $A = 0.8$, and $Bo = 0.131$.

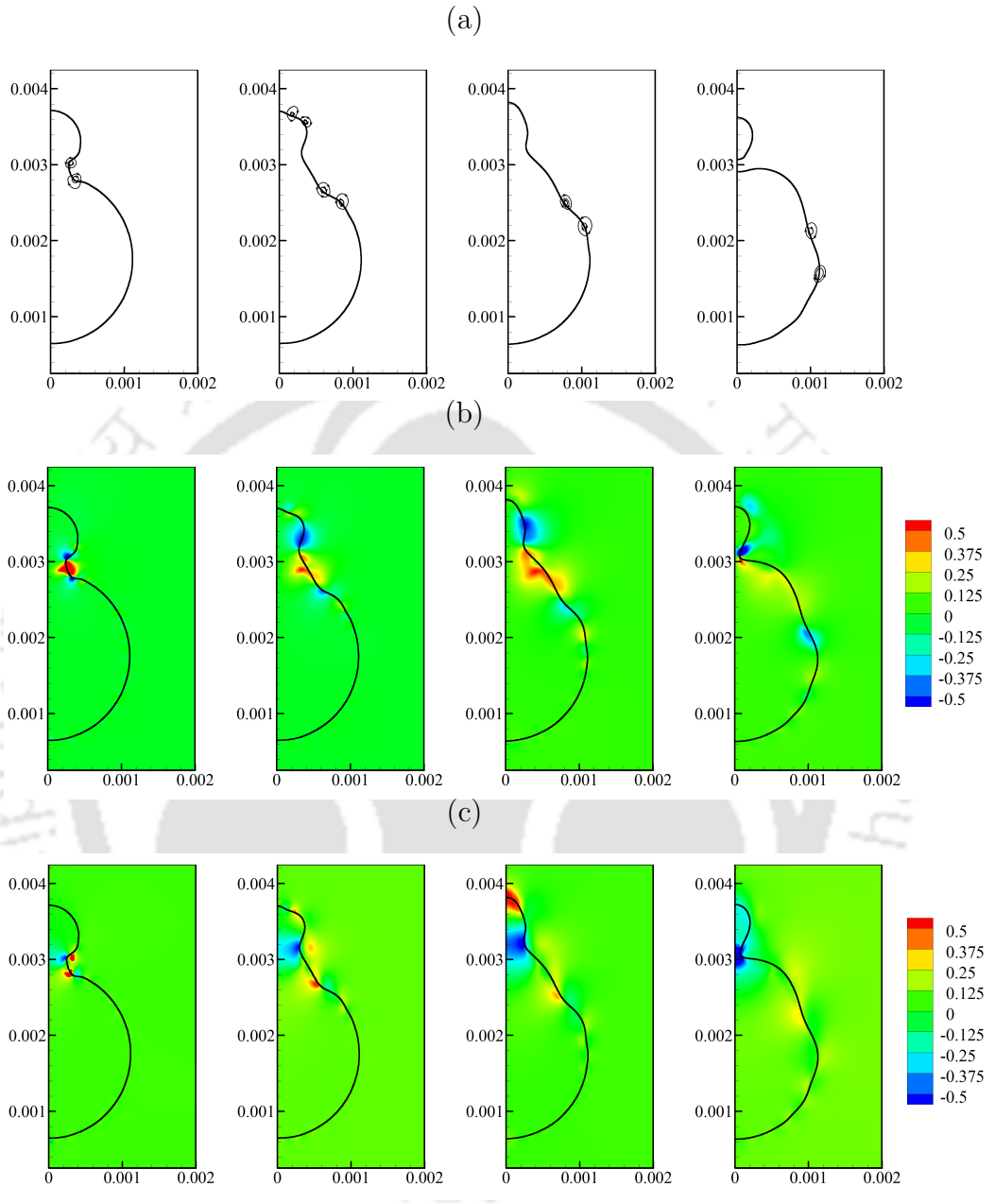

Figure 6.8: (a) The movement of the capillary wave is indicated in the streamline plot, during the coalescence of two drops having diameter ratio $D_f/D_m = 2.72$. The pinch-off takes place before the capillary waves reach the bottom of the lower drop. The profiles from left to right are at time $\tau = 0.16$, 0.36, 0.53 and 0.96 respectively. (b) $u-$velocity and (c) $v-$velocity contour at the same instants of time. The axis labels are in meter. The other non-dimensional parameters are $Oh_1 = 0.005$, $Oh_2 = 0.001$, $A = 0.8$, and $Bo = 0.131$.

drop bottom early, and the capillary pull affects the drop shape and the coalescence dynamics. The capillary wave motion on the lower drop gives a critical condition for the pinch-off of the daughter drop. The downward pull exerted by the capillary waves stretches the father drop and hinder the inward movement of the neck (Fig. 6.7) which finally restricts the pinch-off. Because of this reason, the capillary waves must not reach the bottom of the father drop before the neck merges, for pinch-off to occur. With the increase in diameter ratio of the two drops (D_f/D_m), the time taken by the capillary waves to reach the bottom of the father drop increases. With further increase in the diameter ratio, the neck merges before the capillary waves reach the drop bottom (Fig. 6.8) and culminate the pinch-off.

The criterion of coalescence, whether it is partial or complete, is determined by the competition between the horizontal and vertical rate of collapse [108, 140]. The upward pull generated by the capillary waves stretches the mother drop upward and retards the vertical rate of collapse. This convergence of capillary waves can stretch the drop upwards by as much as 30% of its initial radius [140]. This can be seen in Fig. 6.4, which shows the axial position of the drop tip at different time instants.

Figures 6.7 (b) and 6.8 (b) show the $u-$velocity contour, and, Figures 6.7 (c) and 6.8 (c) show the $v-$velocity contour in the coalescence regime at different time instants. The horizontal and vertical movement inside the drop can be seen in the $u-$velocity and $v-$velocity contour. The upward momentum, exerted by the converged capillary waves, can be seen in Fig. 6.7 (c) and Fig. 6.8 (c). This upward pull stretches the drop and delays the vertical collapse of the drop. Because of this delay in vertical collapse, the horizontal collapse gets sufficient time for completion and the neck pinches off at the centerline to form the daughter drop.

6.4.3 Capillary pressure and neck expansion

When the film between the two drops is broken, it quickly opens due to high pressure gradients created near the hole by surface tension. For smaller values of D_f/D_m, owing to the high pressure inside both the drops, the radial expansion of the neck increases. The radial expansion of the neck is a crucial parameter on the dynamics of pinch-off. Figure 6.9 shows the variation of neck radius (R^*) with time (τ) for different values of father to mother drop diameter ratio (D_f/D_m). The maximum expansion of the neck (R^*_{max}) increases with the reduction in the D_f/D_m ratio, which can be clearly seen in the magnified view shown in the top-right corner of Fig. 6.9.

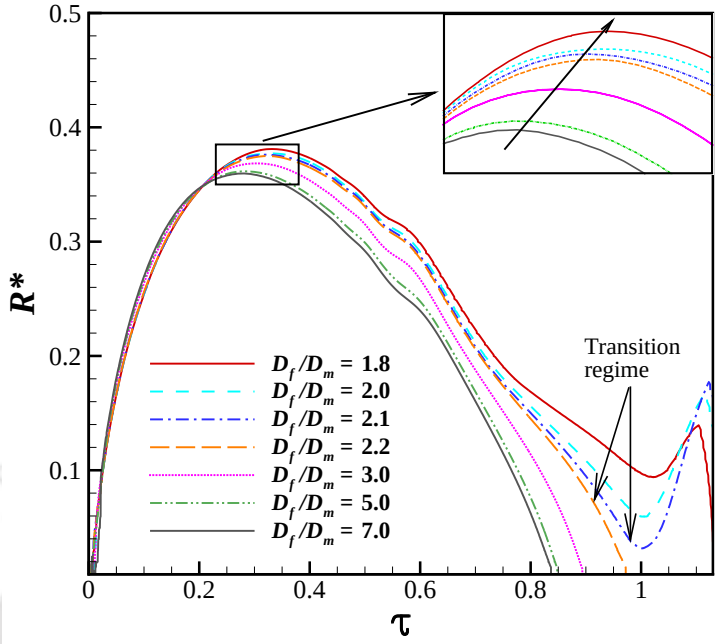

Figure 6.9: The variation of neck radius (R^*) with non-dimensional time (τ) for different values of the diameter ratio of the father drop to the mother drop (D_f/D_m). The value of maximum neck radius (R^*_{max}) increases with the decrease in D_f/D_m. There is a transition from pinch-off regime to no-pinch-off regime above a limit of R^*. The non-dimensional parameters are $Oh_1 = 0.005$, $Oh_2 = 0.001$, $Bo = 0.1311$ and $A = 0.8$.

This is because of the increased capillary pressure inside the father drop with the reduction in the D_f/D_m ratio. Because of larger opening of the neck, the drainage increases and the volume of the daughter drop decreases. Moreover, the start of the retraction stage is also delayed with the decrease in D_f/D_m ratio, resulting in an increase of drainage period and pinch-off time (see Fig. 6.13 (b)). As the retraction of the neck is delayed with the increase in neck opening, the horizontal collapse of the neck is hindered during the retraction period. Beyond a particular limit, the inward horizontal momentum set by capillary wave movement cannot pull back the neck to merge at the center-line and the pinch-off is inhibited. This transition from the pinch-off regime to the no-pinch-off regime is shown by arrows in Fig. 6.9.

Moreover, during the retraction stage of the neck, the local curvature near the neck plays an important role in the pinch-off process. Earlier, Zhang et al. [164] reported the effect of the local curvature of the neck in the second stage pinch-off of satellite. Figure 6.10 (a) shows close-up view of the neck shapes for two different values of D_f/D_m at the onset of pinch-off for two contrasting pinch-off process.

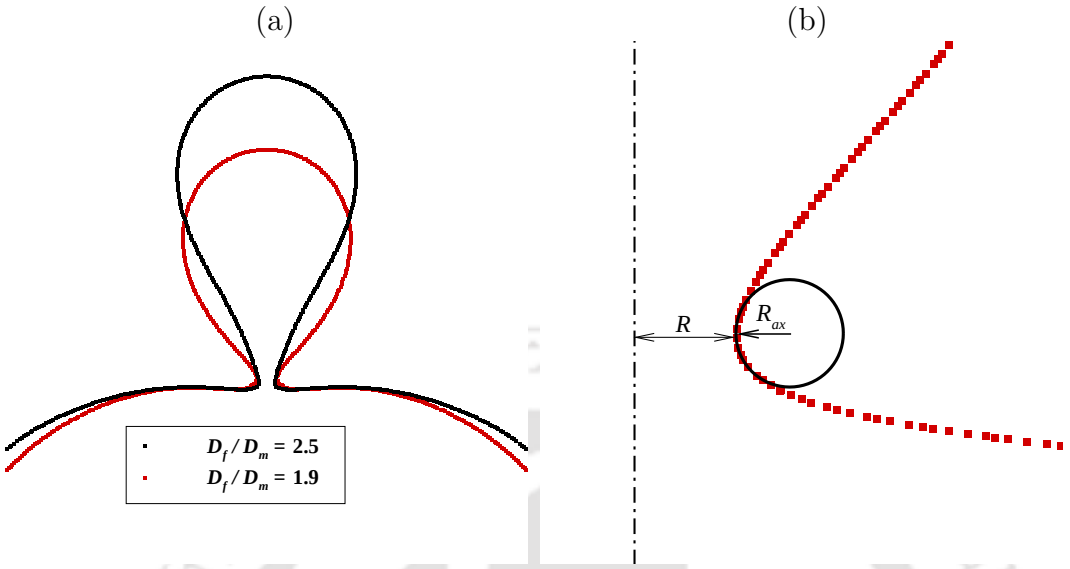

Figure 6.10: (a) Comparison of surface shapes at the onset of pinch-off for two different cases having diameter ratio $D_f/D_m = 1.9$ and $D_f/D_m = 2.5$, possessing for two contrasting pinch-off process. The other dimensionless parameters in both the cases are same ($Oh_1 = 0.005$, $Oh_2 = 0.001$, $A = 0.8$, $Bo = 0.1311$). (b) Typical image to find the radius of curvature in the neck region. The axial radius of curvature (R_{ax}) is measured by fitting the inscribed circle to the surface shape in the neck region.

For $D_f/D_m = 2.5$, the neck merges at the centerline pinching off a daughter drop. However, the neck expands without the pinch-off of the daughter for $D_f/D_m = 1.9$, starting the next stage of coalescence. It can be seen in the profiles of the neck shape that the axial curvature $1/R_{ax}$ is sharper in the second case ($D_f/D_m = 1.9$). We have measured the axial curvature by fitting an inscribed circle to the surface shape, whose radius is equal to the local radius of curvature (R_{ax}) in the neck region as shown in Fig. 6.10 (b). With increases value of axial curvature $1/R_{ax}$, the capillary pressure on the neck owing to axial curvature ($\sim \sigma/R_{ax}$) increases, which tends to expand the neck.

Figure 6.11 shows the variation of R^*_{ax} with the change in radial location of the neck for two different values of diameter ratio D_f/D_m ($D_f/D_m = 1.9$ and $D_f/D_m = 2.5$). It can be seen in the figure that for lower values of D_f/D_m ratio, value of R^*_{ax} is less at the same radial locations ($R^* < 0.165$). Owing to the rapid decrease of R^*_{ax} with the decrease in D_f/D_m, the axial curvature of the neck, $1/R^*_{ax}$, becomes very sharp. As a result, the capillary pressure near the neck region becomes high.

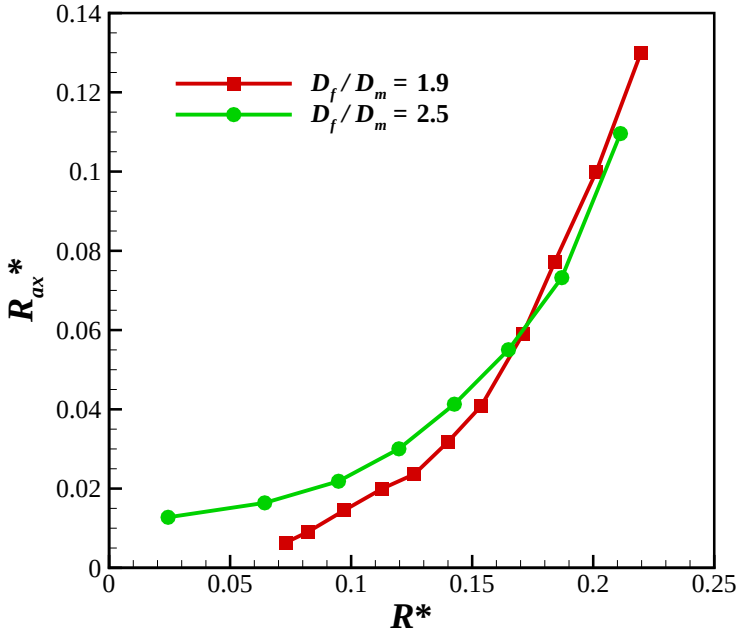

Figure 6.11: The radius of curvature (R^*_{ax}) of the neck at different radial locations for different values of D_f/D_m (1.9 and 2.5). At $D_f/D_m = 2.5$ pinch-off of the daughter drop is observed, whereas at $D_f/D_m = 1.9$ pinch-off is inhibited. The other dimensionless parameters in both the cases are same ($Oh_1 = 0.005$, $Oh_2 = 0.001$, $A = 0.8$, $Bo = 0.1311$).

This high pressure zone can be seen in Fig. 6.12 (a), where the pressure contours are plotted on the left hand side of the axis of symmetry. The high pressure developed near the neck tends to expand the neck and restrict the inward movement of the neck to merge at the centerline. When the diameter ratio is high, the curvature is low and no such high pressure zone is observed as evident in Fig. 6.12 (b) for $D_f/D_m = 2.5$. The velocity vectors are shown on the right hand side of the axis of symmetry in Figs. 6.12 (a) and (b). By examining the velocity field, it has been observed that for $D_f/D_m = 1.9$ the inward horizontal momentum of the collapsing neck becomes very less as the neck becomes thin and reaches the onset of pinch-off. This inhibits the neck from merging at the centerline and the vertical collapse prevails. However, for diameter ratio $D_f/D_m = 2.5$ an inward horizontal momentum is strong enough to cause the merging of the neck at the centerline. This is evident in the velocity vector plot at the onset of pinch-off shown in Fig. 6.12 (b).

The inward moving neck merges at the center-line which leads to pinch-off of the daughter drop. The diameter ratio of the daughter drop to mother drop, D_d/D_m,

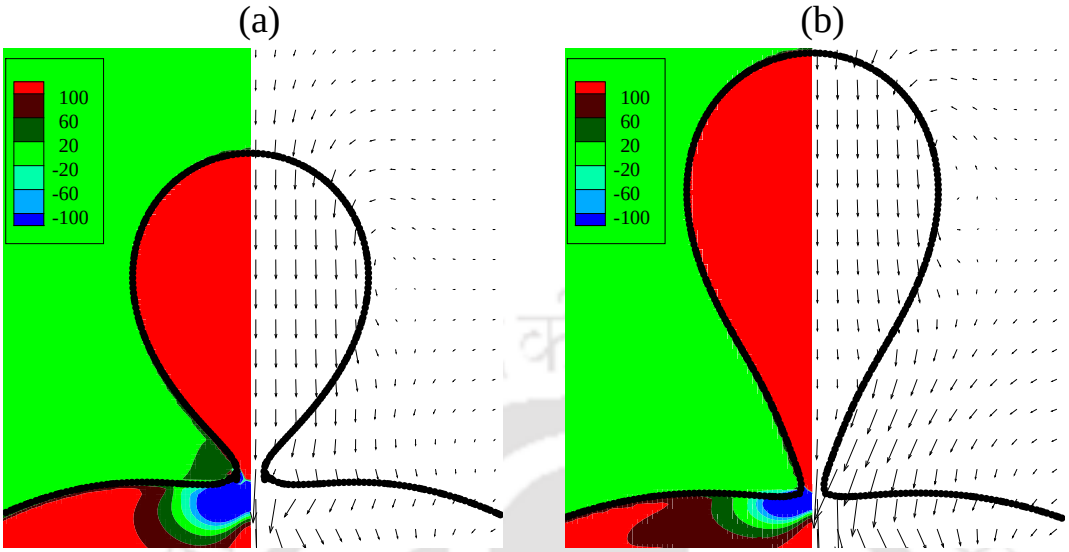

Figure 6.12: The velocity vectors and the pressure contours are plotted at the onset of pinch-off for two different values of D_f/D_m. The D_f/D_m values in (a) and (b) are 1.9 and 2.5, respectively. The velocity vectors are plotted on the right hand side of the symmetry axis and pressure contours are shown are shown on the left hand side of the axis of symmetry. The other dimensionless parameters in both the cases are same ($Oh_1 = 0.005$, $Oh_2 = 0.001$, $A = 0.8$, $Bo = 0.1311$).

depends on the diameter ratio of the father drop to mother drop, D_f/D_m, as depicted in Fig. 6.13 (a). The value of D_d/D_m increases continuously with the increase in the value of D_f/D_m, and reaches an asymptote when the value of D_f/D_m is very large. This asymptotic value of D_d/D_m is equal to the value of D_d/D_m during the coalescence of a drop on a flat liquid pool. In Fig. 6.13 (a), this value is indicated by the dashed line. In can be seen in Fig. 6.13 (a) that the value of D_d/D_m comes closer to this asymptotic value, as the value of D_f/D_m increases. Earlier, Zhang et al. [169] investigated the effect of diameter ratio of the parent drops on the satellite size ratio during the coalescence of two unequal sized bubbles. They observed that the satellite size variation is very small with the change in diameter ratio of the parent drops at large values of D_f/D_m. However, they observed a decrease in the satellite size as D_f/D_m comes close to the critical value below which no pinch-off occurs.

With the increased value of D_f/D_m, the radial expansion of the neck continuously decreases. As a result, the retraction starts early, which promotes the pinch-off. This variation of pinch-off time with the change of D_f/D_m ratio can be seen in Fig.

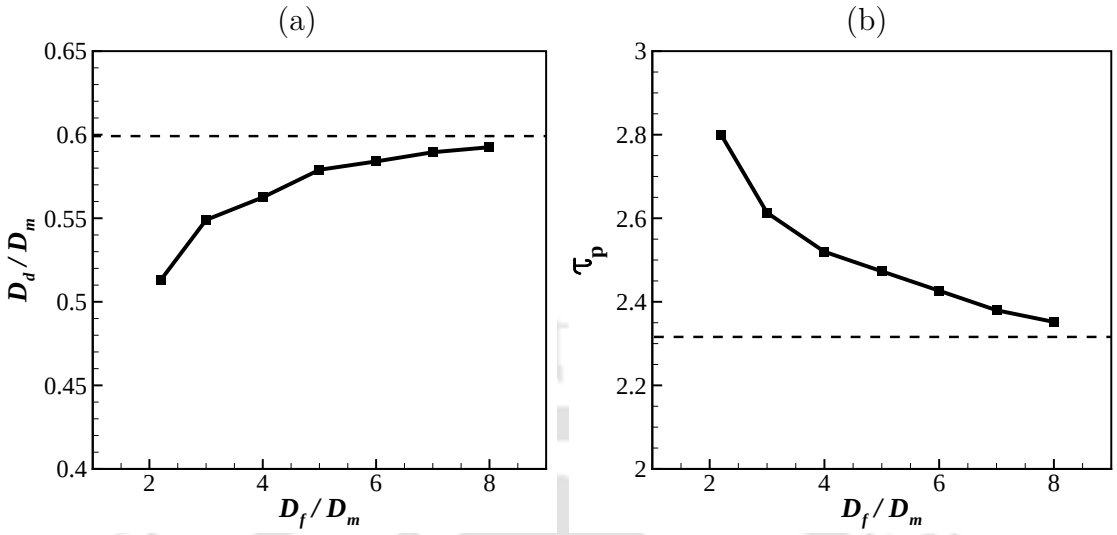

Figure 6.13: (a) The diameter ratio of the daughter drop to mother drop, D_d/D_m, is plotted for different values of the diameter ratio of the father drop to the mother drop D_f/D_m. The value of D_d/D_m increase continuously with the increase in D_f/D_m. (b) The pinch-off time of the daughter drop (τ_p) for different values of the diameter ratio D_f/D_m. The pinch-off time decreases with the increase of D_f/D_m ratio. The dashed line indicate the values in the case of coalescence onto a flat liquid pool. The non-dimensional parameters are $Oh_1 = 0.005$, $Oh_2 = 0.001$, $Bo = 0.1311$ and $A = 0.8$.

6.13 (b). The pinch-off time decreases with the increase of the value of D_f/D_m, because of ease of inward movement of the interface. This is in agreement with the experimental observations of Zhang et al. [164]. Zhang et al. [169] also observed similar trend during the coalescence of two unequal sized bubbles. Because of the early pinch-off of the daughter drop, the drainage from the mother drop onto the father drop decreases. As a result, the volume of the daughter drop increases with the increase in D_f/D_m ratio, as evident in Fig. 6.13 (a).

6.4.4 Effect of viscosity

The stretching of the drop decreases with the increase in Ohnesorge number (both Oh_1 and Oh_2), because, the propagating capillary waves are damped out by the increased viscosity. It has been described in Fig. 6.6, where the axial location of the drop tip is plotted with time for different Ohnesorge numbers. Because of the inhibition of capillary wave movement with increased viscosity, the critical diameter ratio for satellite formation increases with the increase in Ohnesorge number. In Fig.

6.14, the critical diameter ratio for which the daughter drop pinches off, is plotted for different values of Ohnesorge number. The critical diameter ratio $(D_f/D_m)_c$ increases monotonically with the increase in the value of Oh_1, as depicted in Fig. 6.14 (a). The increased viscosity of the surrounding fluid has the same effect as that of the drop fluid as the capillary wave movement is also damped out by the viscosity of the surrounding fluid. The effect of surrounding fluid viscosity can be seen in Fig. 6.14 (b), where the variation of $(D_f/D_m)_c$ is plotted for different values of Oh_2. For lower values of Oh_1 and Oh_2, the critical diameter ratio $(D_f/D_m)_c$ for daughter formation is less. The minimum value of $(D_f/D_m)_c$ was predicted to be approximately 1.55 by Zhang et al. [164] and to be approximately 1.6 by Blanchette and Bigioni [163]. We also attempted to find out this minimum value of D_f/D_m, below which pinch-off is observed during the coalescence of two free-floating unequal sized drops. In this investigation, we have observed that the minimum value converges at 1.65 for the inviscid case, which is slightly higher than the earlier predictions.

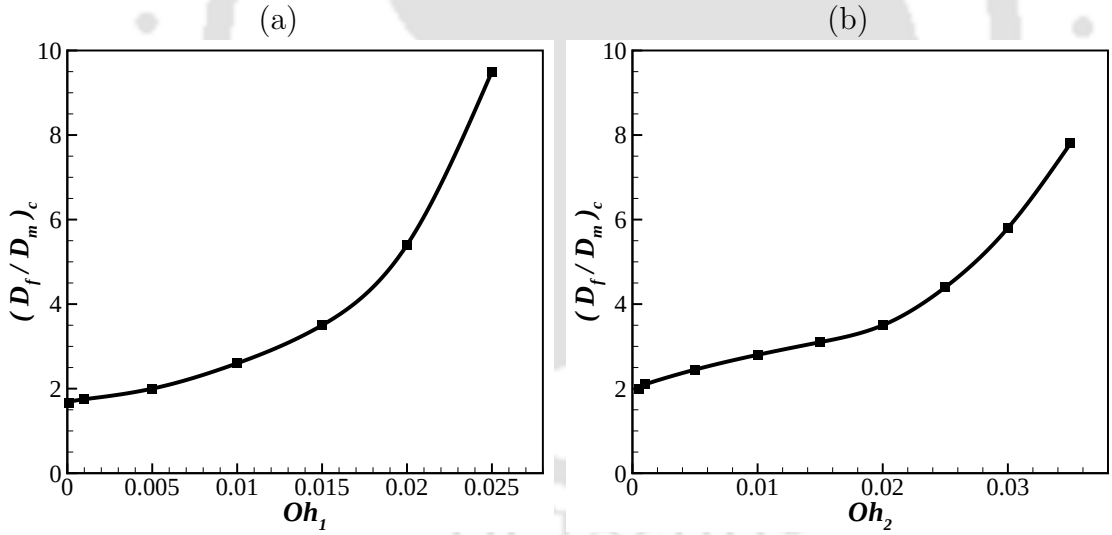

Figure 6.14: (a) Variation of critical diameter ratio, $(D_f/D_m)_c$, for different values of Oh_1.The other dimensionless parameters are $Oh_2 = 0.001$, $A = 0.8$, and $Bo = 0.1311$. (b) Variation of critical diameter ratio, $(D_f/D_m)_c$, for different values of Oh_2. The other dimensionless parameters are $Oh_1 = 0.005$, $A = 0.8$, and $Bo = 0.1311$.

However, it worth pointing out that Zhang et al. [164] predicted the critical diameter ratio based on the experimental observations, where the father drop was resting on a nozzle. When the capillary waves traveling through the interface of

the father drop reach the bottom nozzle, the waves either reflect back from the nozzle or the waves die down on the liquids in the nozzle. However, in the case of coalescence of two free-floating drops, the capillary waves that travel through the interface of the lower drop converge at its bottom and impart a downward vertical momentum. The downward pull on the father drop interface imparts additional restriction to pinch-off, which is absent in the case of a drop resting on a nozzle. Hence, the critical parameter for free-floating drops deviates a little than that of the experimental observations of drops resting on a nozzle.

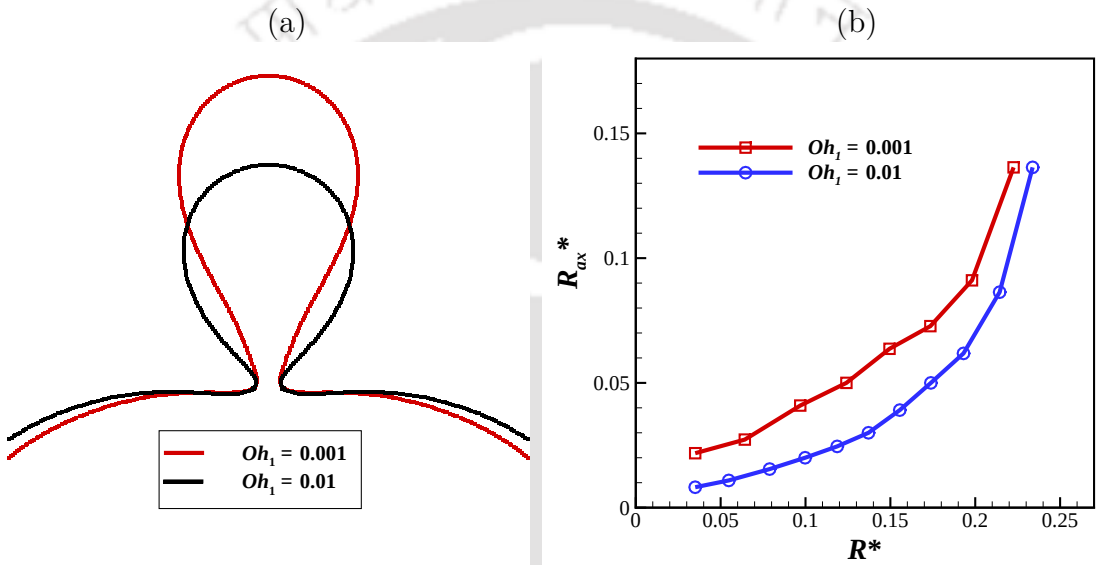

Figure 6.15: (a) Comparison of surface shape at the onset of pinch-off for different values of Ohnesorge number (Oh_1). (b) The radius of curvature (R^*_{ax}) of the neck at different radial locations for different values of Oh_1 (0.001 and 0.01). With increased viscosity the axial radius of curvature of the neck decreases. The other dimensionless parameters in both the cases are same ($D_f/D_m = 2.5$, $Oh_2 = 0.001$, $A = 0.8$, $Bo = 0.1311$).

The local curvature near the neck plays an important role in the pinch-off process. Figure 6.15 (a) shows a close-up view of the neck shapes at the onset of pinch-off for two different Ohnesorge number having a contrasting pinch-off sequel. At $Oh_1 = 0.001$ pinch-off took place, whereas the neck expands without pinch-off for $Oh_1 = 0.01$. It can be seen in the profiles of the neck shape that the axial curvature $1/R_{ax}$ is sharper in the second case ($Oh_1 = 0.01$). With increases value of axial curvature $1/R_{ax}$, the capillary pressure on the neck region owing to axial curvature ($\sim \sigma/R_{ax}$) increases, which tends to expand the neck. Figure 6.15 (b) shows the variation of

R^*_{ax} with the change in radial location of the neck for the two different values of Ohnesorge number ($Oh_1 = 0.001$ and $Oh_1 = 0.01$). At higher viscosity, the value of R^*_{ax} is less at the same radial locations. Therefore, the net capillary force tends to expand the neck and restrict the pinch-off.

6.4.5 Effect of density contrast

The apparent weight of the drop ($(\rho_1 - \rho_2)g$) depends on the density contrast between the drop liquid and the surrounding fluid. With the decrease in the density contrast, the relative weight of the drop decreases, which results in ease of lift-up. A difference in density between the two fluids does not generate any significant delay in the capillary wave propagation [165]. As a result, the same capillary pull is able to stretch and lift up the mother drop more easily with the decrease in density contrast. This effect of density contrast, on the formation of daughter drop, can be seen in Fig. 6.16. The critical diameter ratios of the father and mother drops at different values of Atwood number (A) have been plotted in Fig. 6.16. The critical ratio, $(D_f/D_m)_c$, for daughter drop formation decreases with the decrease of Atwood number, indicating the ease of pinch-off with the decrease in density contrast. As the value of A increases, the more lifting force is needed for the pinch-off of

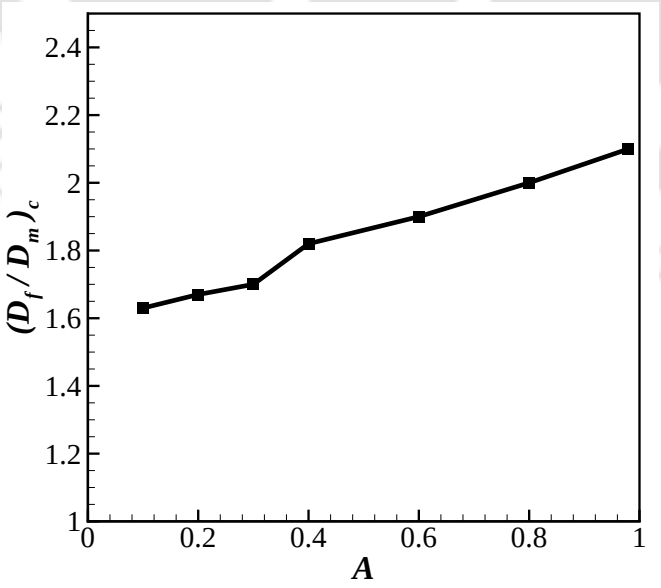

Figure 6.16: Variation of critical diameter ratio (D_f/D_m) for different values of Atwood number (A). The other non-dimensional parameters are $Oh_1 = 0.005$, $Oh_2 = 0.001$, and $Bo = 0.0164 - 0.1635$.

the secondary drop, such that the vertical collapse is sufficiently delayed and the horizontal collapse reach completion. The lifting force during pinch-off is provided by the capillary pull, which is limited. Because of this reason, the value of critical diameter ratio for the formation of secondary drop increases with the increase in Atwood number.

6.4.6 The coalescence cascade

Partial coalescence of a drop may take place in several steps of coalescence, each time generating a daughter drop of smaller volume [125, 138]. Thoroddsen and Takehara [125] named it as coalescence cascade and observed that the phenomenon is self-similar in each consecutive steps of the coalescence cascade. Experimentally, such a cascade is observed up to eight steps, during the coalescence of a drop onto a liquid

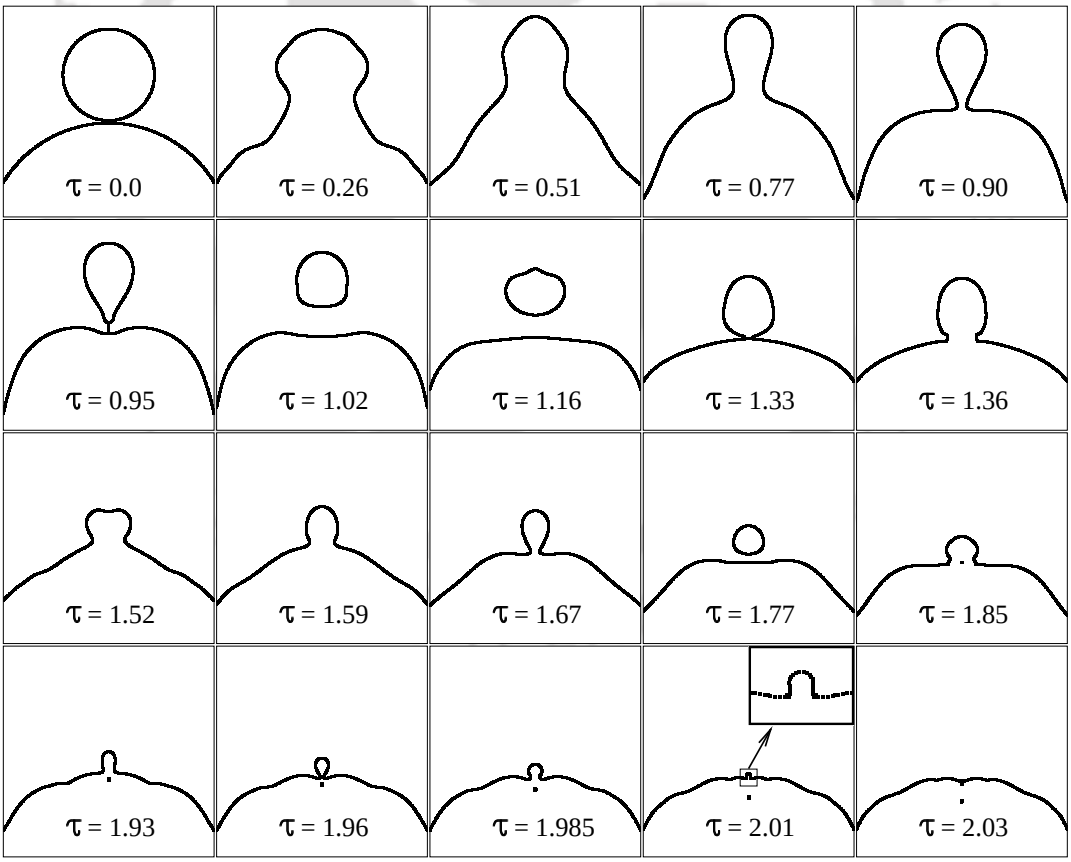

Figure 6.17: The coalescence cascade observed during the coalescence of two drops having diameter ratio $D_f/D_m = 2.72$. The other dimensionless parameters are $Oh_1 = 0.0046$, $Oh_2 = 9.215 \times 10^{-5}$, $Bo = 0.228$ and $A = 0.997$.

pool [123]. In the current investigation, it has been observed that the formation of such coalescence cascade also takes place during the coalescence of two dissimilar sized drops. Figure 6.17 shows such a cascade of coalescence during the coalescence of two unequal sized drops having diameter ratio $D_f/D_m = 2.72$. As depicted in Fig. 6.17, at $\tau = 0.95$ we observe the first pinch-off. The resulting daughter drop undergoes prolate-oblate-prolate oscillation, and after a certain duration, the daughter drop moves down and comes in contact with the interface ($\tau = 1.33$), and the second stage of partial coalescence begins.

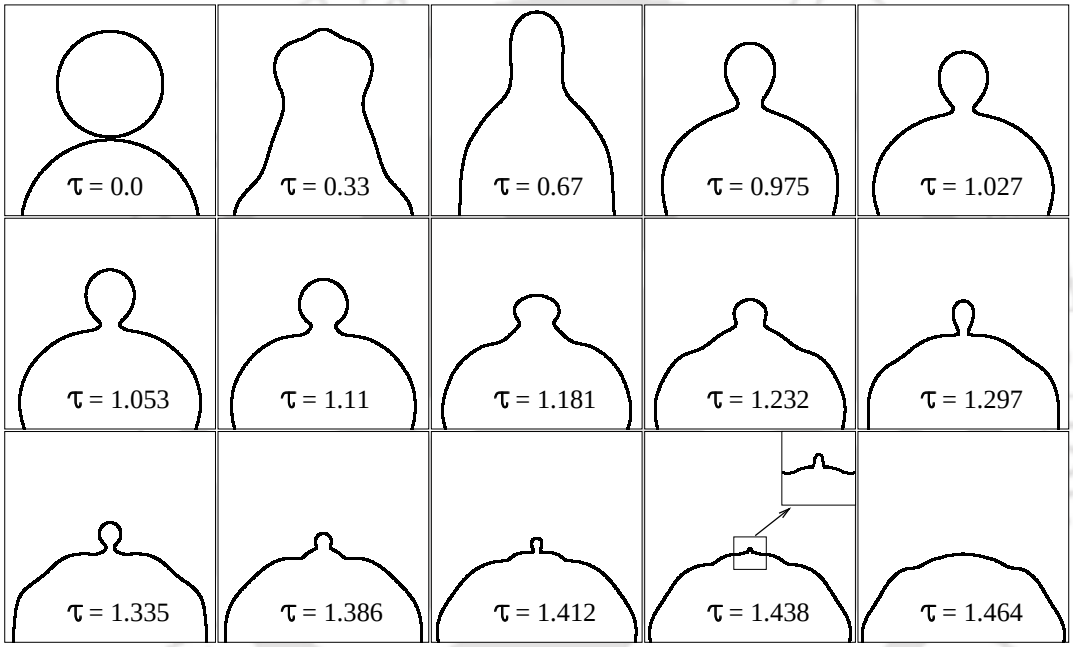

Figure 6.18: The coalescence cascade observed during the coalescence of two drops having diameter ratio $D_f/D_m = 1.7$. The other dimensionless parameters are $Oh_1 = 0.0046$, $Oh_2 = 9.215 \times 10^{-5}$, $Bo = 0.228$ and $A = 0.997$.

In the second stage, the daughter drop of the first stage behaves like a new mother drop and repeats the same processes like column formation and necking and at $\tau = 1.77$ we observe a tertiary drop. The tertiary drop then undergoes prolate-oblate-prolate oscillation and finally touches the interface. The tertiary drop after touching the father drop again forms a columnar structure ($\tau = 1.93$) and reaches the onset of pinch-off. However, without any intermediate detachment, the fourth stage of partial coalescence begins. In the fourth stage, the drop again forms a columnar structure and completely coalesces onto the father drop. The diameter ratios of the daughter and mother drops in the first two steps are 0.58 and 0.55,

respectively. Here, the process of partial coalescence completes in a cascade of four steps, with two distinct pinch-offs.

Figure 6.18 shows another partial coalescence cascade for $D_f/D_m = 1.7$, $Oh_1 = 0.0046$, $Oh_2 = 9.215 \times 10^{-5}$, $Bo = 0.228$ and $A = 0.997$. Similar to Fig. 6.17, the drops after coalescence form a columnar structure ($\tau = 0.67$) and the necking starts. However, in this case, the satellite does not detach from the father drop. After completing the retraction stage ($\tau = 1.027$), the neck expands and the second stage of coalescence begins. In the second stage also, the neck expands without the pinch-off of the satellite after reaching the onset of pinch-off ($\tau = 1.297$), starts the third stage of coalescence. During the third stage, it again forms a columnar structure ($\tau = 1.386$) with the initiation of necking. The neck again expands without the pinch-off of the daughter and starts the fourth stage of coalescence. The columnar structure of the drop at the fourth stage of coalescence can be observed at $\tau = 1.438$. The mother drop finally coalesces into the father drop completely. The coalescence cascade completes in four steps, although no intermediate detachment of satellite takes place.

6.5 Summary

In this study, the coalescence dynamics of two unequal sized free-floating drops have been investigated. The effect of the fluid properties on the dynamics of partial coalescence has been studied. Capillary waves are generated during the coalescence of drops owing to the high curvature developed near the contact region. The capillary wave motion and the local curvature effect near the neck drive the satellite formation process. Satellite formation is inhibited below a critical value of the diameter ratio between the father and mother drops. The minimum value of critical diameter ratio for satellite formation is found to be approximately 1.65. The coalescence of two unequal sized drops may take place through the formation of a cascade of coalescence, with or without intermediate detachment.

Chapter 7

Conclusions and scope for future work

In this thesis, some of the fascinating aspects of drop formation, impact of a falling drop on a liquid pool and bubble entrapment have been investigated. In addition, the impact of a train of high-speed microdrops on a deep liquid pool have been investigated. Investigations have also been performed on satellite generation during the coalescence of two unequal sized drops. The coupled level set and volume-of-fluid (CLSVOF) method has been used to numerically model the flow and investigate the subsequent dynamics. The main findings of these investigations and the conclusions that are drawn from these studies have been summarized in this chapter. Furthermore, during the investigations, we have identified some of the areas which need more focused attention for complete understanding of the underlying physics. These topics form the basis for future work. These scopes for future work have been enumerated in this chapter.

7.1 Conclusions

The objectives of the present investigations have been prompted by the progress in research so far. The investigations are performed to elucidate some of the inherent features of drop formation and coalescence to get more insight into the underlying physics. Some of the intrinsic features of drop formation and coalescence processes have been revealed. The numerical methodology used for modeling the flow has

been elaborately explained. The conclusions drawn from the investigations that have been performed during the course this thesis work are outlined below.

Numerical simulations are performed on the mechanism of non-spherical drop formation from an orifice in the dripping regime. The oscillating behavior of a drop after pinch-off has been studied. Based on the investigations performed, the following conclusive remarks have been drawn.

During drop formation from an orifice, the surface tension force holds the drop pendant from the orifice without allowing it to fall until the surface tension force can no longer balance the gravitational force pulling the drop down. The pendant drop then rapidly elongates and its diameter reduces around the mid-plane initiating the necking. The neck finally merges at the central axis and the drop separates from the fluid attached to the orifice. With the increase in flow rate, the liquid inertia that acts in the axial direction increases the length of pendant drop and the necking takes place at a greater height from the tip of the pendant drop. This is because, at a higher flow rate, a larger velocity gradient exists inside the drop which culminates in a strong shear force within the drop. As a result, the axial length of the drop at the incipience of pinch-off becomes more than the radial length and converts it into a prolate shaped drop. The aspect ratio of a drop, during pinch-off, continuously increases with the increase in Weber number.

Increased viscosity of the drop fluid damps out the velocity gradient inside the drop. As a result, the deformation of the drop decreases with the increase in viscosity of the drop fluid and assumes a nearly spherical shape at higher values of viscosity. The shape of the pinching drop is also affected by the properties of the surrounding fluid. The drop shape does not depend on the density of the surrounding fluid at lower values of density ratio. However, at higher values of density ratio, the shear stress distribution inside the drop is affected by the net buoyant force acting on the drop surface and the aspect ratio of the drop increases with increase in density ratio. Similarly, the drop shape is affected very little by the surrounding fluid viscosity at lower values of viscosity ratio. However, at higher values of viscosity ratio, the shear stress distribution inside the drop is affected by the viscosity of the surrounding fluid and the aspect ratio of the drop at the time of pinch-off increases with increase in viscosity of the surrounding fluid.

A non-spherical drop oscillates while falling through a surrounding medium because of the local capillary pressure developed across the interface. At the time of pinch-off, the downward vertical momentum near the pinching region of the drop

becomes very high. Because of the higher downward vertical momentum near the pinching region, a vertical pull acts on the drop surface near the pinching region. As a result, the liquid near the pinching region moves inward and deforms the shape of the drop after pinch-off, and thus initiating the oscillation of the drop. The oscillatory motion of a drop is damped by the viscosity. The oscillatory motion of drops can be reduced substantially at higher values of Oh as higher Oh culminates in a spherical shape during pinch-off and also resist the deformation and oscillation of the drop after pinch-off.

In the sequel, the investigations are performed on the mechanism of large bubble entrapment during a drop impact on a deep liquid pool. The important findings of this investigation are summarized below.

The large bubble entrapment regime is not the small regime as previously reported on the traditional V-D map. Large bubble entrapment is observed over a wide region on the V-D map. In the current study, the regime of large bubble entrapment on the V-D map and on the We-Fr map have been identified. The shape of the drop must be prolate at the time of impact for large bubble entrapment to take place. Sometimes the large bubble is accompanied by the entrapment of a small bubble. In the current investigation, the sequential bubble pair has been simulated proving the discovery from experiments.

Vorticity is generated near the interface during drop impact on a pool. The strength of the vorticity depends on the impact conditions and on the shape of the drop at the time of impact. For a prolate shaped drop, the vortex moves deeper into the pool. This vortex later pulls and curls-up the interface to form the roll jet. The roll jet merges at the centerline to entrap a large bubble inside the pool. The vorticity strength must be strong enough to make the roll jet merge at the centerline for the entrapment of large bubble. For an oblate shaped drop, the vortex penetration is less and its strength decreases due to early interaction with the interface.

Depending on the impact conditions, an ejecta sheet may emerge near the neck region during drop impact onto a pool. The emergence of ejecta sheet merged with the lamella, prevents the separation and penetration of the vortex ring onto the pool, which in turn, prevents the entrapment of large bubble. The emergence of ejecta sheet which leads lamella culminates in a wider opening of the crater mouth without the formation of roll jet.

Large bubble entrapment takes place because of the merging of the roll jet at the centerline and is always accompanied by the formation of an inward and an upward

jet. The inward jet penetrates the bubble and deforms its shape. In the case of large bubble entrapment, the crater dynamics is controlled by the vortical flow. We have observed that within the large bubble entrapment regime, the enclosure depth, the crater depth and the pinch-off time decrease with the increase in impact velocity of the drops. The same parameters increase with the increase in the size of the drops. Quantitative analysis of the cavity characteristics reveals consistency in the trends apparent in the numerical and experimental results.

Furthermore, investigations are performed on the cavity dynamics during the impact of a high-speed train of microdrops on a liquid pool. The major conclusions that have been drawn from this investigation are listed below.

The impact of a high-speed microdrop on a liquid pool creates a deep crater on the pool because of the large momentum transferred by the impacting microdrop on the pool. The depth of the crater can be increased by continuous impact of multiple microdrops. Such impact of a train of high-speed microdrops creates a deep cavity inside the liquid pool, whose depth could be more than hundred times the microdrop diameter. Capillary waves emerge from the crater base owing to the impact of drops and propagate along its wall. As multiple drops impact the crater, we observe multiple waves emerging from the crater base and moving through the crater wall. In the current investigation, it has been observed that these capillary waves converge near the cavity mouth and expedite the necking.

The penetration depth continuously increases with the increase in train length. However, with the increase in frequency of the impacting microdrops, the penetration depth first increases and then starts to decrease. Maximum penetration can be achieved at an optimum frequency, above which the penetration decreases because of shortage in adequate time for momentum diffusion for the impact of each individual drop. The penetration velocity of the cavity increases with the increase in frequency. The maximum penetration velocity can be achieved when the drops are attached to each other, which forms a continuous liquid jet. The maximum attainable penetration velocity of the is equal to half the impact velocity of the drops, which is in agreement with earlier investigations.

A long train of microdrops produces a deep cavity, where the retraction of the cavity mouth takes place before the completion of impact of all the drops in the train. Whereas a shorter train of microdrops produces a shallow cavity, where the necking and retraction of the cavity mouth start after the impact of all the drops in the train. In the case of a shallow cavity, the pinch-off time of the cavity decreases

with the increase in train length $\tilde{L_t}$. However, the pinch-off time is independent of train length for a deep cavity. For both shallow and deep cavities, the pinch-off time increases with the increase in Weber number. Moreover, the pinch-off depth increases with the increase in $\tilde{L_t}$ in the case of shallow cavities. For deep cavities, the pinch-off depth initially increases by a small amount and becomes constant for higher values of $\tilde{L_t}$.

The motion of the cavity mouth has an expansion stage and a collapse stage. The radial movement of the neck shows power law behavior in both expansion stage and collapse stage. In the pinching region, the cavity collapse phenomenon is self-similar in nature. The cavity profiles at different time instants can be collapsed into a single profile by using a suitable fitting function.

In the present investigation, it has been observed that the pinch-off of a cavity depends on the depth of penetration of the cavity as well as on the radial expansion of the cavity. The critical train length $\tilde{L_t}$ for which cavity pinch-off occurs has been observed when its penetration depth becomes approximately three times the average diameter of the cavity. The critical train length for pinch-off increases with the increase in We, as larger We culminates into more radial expansion of the cavity.

Finally, we have studied the coalescence dynamics of two unequal sized drops. The conclusions drawn from this investigation as summarized as follows.

When two liquid drops are brought into contact, the drops rest on the interface for a small duration until the film between the two drops ruptures. The drops then coalesce rapidly, owing to the large curvature and unbalanced surface-tension forces in the neck region. The coalescence speed of the drops can be modeled by balancing the dynamic pressure and the capillary pressure.

Capillary wave is produced by the expanding neck because of the high curvature generated near the contact line. With the increased value of diameter ratio of the father and mother drops D_f/D_m, the flatness of the surface of the father drop increases which results in higher curvature in the neck region. Higher curvature produces stronger capillary waves resulting in more vertical stretching of the drops. The capillary pull delays the vertical collapse of the mother drop such that the horizontal collapse reaches completion resulting in pinch-off of daughter drops. The propagation of the capillary wave is damped by viscosity which reduces the vertical pull on the drop and thus inhibits the pinch-off.

During the coalescence of two drops, the capillary waves which travel through the interface of the lower father drop converge at its bottom and impart a downward

pull. The capillary pull stretches the father drop and hinders the inward movement of the neck, thus inhibiting the pinch-off when the capillary waves reach the bottom of the father drop before the pinch-off of the daughter.

The capillary pressure inside the drops is an important parameter affecting the radial expansion of the neck during the coalescence. The maximum expansion of the neck increases with the reduction in the D_f/D_m ratio because of the increased capillary pressure inside the father drop. The retraction of the neck is delayed with the increase in neck opening and the horizontal collapse of the neck is hindered during the retraction period. Because of larger opening of the neck, the drainage increases and the volume of the daughter drop decreases. Beyond a particular limit, the vertical rate of collapse dominates over the horizontal rate of collapse and inhibits the satellite formation.

The local curvature near the neck plays an important role in the pinch-off process. When the azimuthal curvature of the neck becomes significantly sharper, it increases the local capillary pressure in the neck region which tends to expand the neck and hinders the pinch-off. The curvature of the neck increases with the decrease in D_f/D_m ratio as well as with the increase in viscosity, owing to the hindrance in vertical stretching of the mother drop in both the cases. Increased viscosity dampens out the capillary wave propagation, and thus favors the coalescence. As a result, which the critical diameter ratio for satellite formation increases with the increased value of Ohnesorge number. During the coalescence of two free-floating drops, the minimum value of critical diameter ratio for satellite formation is found to be approximately 1.65.

In the present investigation, it has been observed that the coalescence of two dissimilar sized drops takes place through the formation of a cascade of coalescence. Such a cascade may form with or without the intermediate detachment of the satellite drops. In the case of detachment of satellite drops, the satellite drops oscillate between the prolate and oblate shapes before it comes in contact with the interface and begins the next stage of coalescence.

7.2 Scope for future work

In the context of the outcomes of the present investigations, it has been observed that some of the areas need further investigations to completely understand the

underlying physics. The scope for future study related to various dynamical aspects of free surface flows in the context of drop formation and coalescence are listed below.

In this thesis, the drop formation process has been investigated focusing the shape of the drop during pinch-off. However, the investigations are performed on Newtonian fluids only. More investigations are needed to elucidate the effects of various flow parameters on the resulting shape of the drop in the case of non-Newtonian fluids. The effects of the electro-hydrodynamic and magneto-hydrodynamic forces on the shape of the drop at the incipience of pinch-off are to be investigated with rigour.

The regime of large bubble entrapment has been identified in the current investigation. However, further investigations are needed to elucidate the effect of constriction on large bubble entrapment during the impact of a drop on a constricted liquid pool. It will be interesting to observe the interaction of the vortex ring with the constricted wall and its effect on the dynamics of large bubble entrapment.

The coalescence behavior of a drop is to be analyzed when there is a temperature difference between the drop and the pool liquid. The effect of temperature gradient along the interface is likely to culminate in the tangential component of the capillary force to act at the interface. This leads to Marangoni convection in the surrounding liquid which may change the coalescence dynamics.

Furthermore, investigations need to be performed to understand the effects of external electric field and magnetic field on the dynamics of the slender cavity formed by the impact of high-speed microdrops.

In the present investigations, the pinch-off dynamics and the parameters controlling the satellite generation during the first stage coalescence have been analyzed. In the experimental work of Zhang et al. [164], they observed satellite pinch-off in the second stage of coalescence without intermediate detachment in the first stage of coalescence. Further study is needed to shed light on the controlling parameters for satellite generation to get the complete insight of such pinch-off mechanism. In a recent investigation, Dong et al. [170] observed that the range of inertio-capillary regime reduces with the presence of surfactants during the coalescence of a drop on a liquid pool. Investigations need to be performed to see the effect of surfactants on satellite generation during the coalescence of two unequal sized drops.

References

[1] Worthington A.M., *A Study of Splashes* (Longmans, Green and Co., 1908), 1st Ed.

[2] Harlow F.H. and Shannon J.P. (1967) 'Distortion of a splashing liquid drop', *Science*, vol. 157(3788), pp. 547–550.

[3] Harlow F.H. and Shannon J.P. (1967) 'The splash of a liquid drop', *Journal of Applied Physics*, vol. 38(10), pp. 3855–3866.

[4] Ray B., Biswas G., and Sharma A. (2015) 'Regimes during liquid drop impact on a liquid pool', *Journal of Fluid Mechanics*, vol. 768(10), pp. 492–523.

[5] Basaran O.A., Gao H., and Bhat P.P. (2013) 'Nonstandard inkjets', *Annual Review of Fluid Mechanics*, vol. 45(1), pp. 85–113.

[6] Hirt C.W. and Nichols B. (1981) 'Volume of fluid (VOF) method for the dynamics of free boundaries', *Journal of Computational Physics*, vol. 39(1), pp. 201–225.

[7] Welch S.W. and Wilson J. (2000) 'A volume of fluid based method for fluid flows with phase change', *Journal of Computational Physics*, vol. 160(2), pp. 662–682.

[8] Lafaurie B., Nardone C., Scardovelli R., Zaleski S., and Zanetti G. (1994) 'Modeling merging and fragmentation in multiphase flows with SURFER', *Journal of Computational Physics*, vol. 113, pp. 134–147.

[9] Noh W.F. and Woodward P. (1976) 'Slic (simple line interface calculation)', *Proceedings of the Fifth International Conference on Numerical Methods in*

Fluid Dynamics, June 28 – July 2, 1976, Twente University, Enschede, pp. 330–340.

[10] Youngs D.L., 'Time-dependent multi-material flow with large fluid distortion', in 'Numerical Methods for Fluid Dynamics', (Academic Press, New York, 1982), pp. 273–285.

[11] Puckett E.G., Almgren A.S., Bell J.B., Marcus D.L., and Rider W.J. (1997) 'A high-order projection method for tracking fluid interfaces in variable density incompressible flows', *Journal of Computational Physics*, vol. 130(2), pp. 269–282.

[12] Renardy Y. and Renardy M. (2002) 'Prost: A parabolic reconstruction of surface tension for the volume-of-fluid method', *Journal of Computational Physics*, vol. 183(2), pp. 400–421.

[13] Osher S. and Sethian, J. A. (1988) 'Fronts propagating with curvature dependent speed', *Journal of Computational Physics*, vol. 79, pp. 12–49.

[14] Sussman M. and Puckett E.G. (2000) 'A coupled level set and volume-of-fluid method for computing 3D and axisymmetric incompressible two-phase flows', *Journal of Computational Physics*, vol. 162(2), pp. 301–337.

[15] Gerlach D., Tomar G., Biswas G., and Durst F. (2006) 'Comparison of volume-of-fluid methods for surface tension-dominant two-phase flows', *International Journal of Heat and Mass Transfer*, vol. 49(3-4), pp. 740–754.

[16] Brackbill J.U., Kothe D.B., and Zemach C. (1992) 'A continuum method for modeling surface tension', *Journal of Computational Physics*, vol. 100, pp. 335–354.

[17] Sussman M., Smereka P., and Osher S. (1994) 'A level set approach for computing solutions to incompressible two-phase flow', *Journal of Computational Physics*, vol. 114, pp. 146–159.

[18] Harlow F.H. and Welch J.E. (1965) 'Numerical calculation of time-dependent viscous incompressible flow of fluid with free surface', *Physics of Fluids*, vol. 8, pp. 2182–2189.

[19] Strang G. (1968) 'On the construction and comparison of difference schemes', *SIAM Journal on Numerical Analysis*, vol. 5(3), pp. 506–517.

[20] Chang, Y. C., Hou T.Y., Meriman B., and Osher S. (1996) 'A level set formulation of Eulerian interface capturing methods for incompressible fluid flows', *Journal of Computational Physics*, vol. 464(124), pp. 449–464.

[21] Son G. (2003) 'Efficient implementation of a coupled level-set and volume-of-fluid method for three-dimensional incompressible two-phase flows', *Numerical Heat Transfer, Part B: Fundamentals*, vol. 43(6), pp. 549–565.

[22] Center for Applied Science Computing, Lawrence Livermore National Laboratory, USA (2006) *Hypre 2.0.0 user manual*, silver Ed.

[23] Harkins W.D. and Brown F.E. (1919) 'The detrrmination of surface tension (free surface energy), and the weight of falling drops: The surface tension of water and benzine by the capillary height method', *Journal of the American Chemical Society*, vol. 41(4), pp. 499–524.

[24] Yildirim O.E., Xu Q., and Basaran O.A. (2005) 'Analysis of the drop weight method', *Physics of Fluids*, vol. 17(6), p. 062107.

[25] Heideger W.J. and Wright M.W. (1986) 'Liquid extraction during drop formation: Effect of formation time', *AIChE Journal*, vol. 32(8), pp. 1372–1376.

[26] Utada A.S., Lorenceau E., Link D.R., Kaplan P.D., Stone H.A., and Weitz D.A. (2005) 'Monodisperse double emulsions generated from a microcapillary device', *Science*, vol. 308(5721), pp. 537–541.

[27] Eggers J. and Villermaux E. (2008) 'Physics of liquid jets', *Reports on Progress in Physics*, vol. 71(3), p. 036601.

[28] Reitz R.D. and Beale J.C. (1999) 'Modeling spray atomization with the Kelvin-Helmholtz/Rayleigh-Taylor hybrid model', *Atomization and Sprays*, vol. 9(6), pp. 623–650.

[29] Shield T.W., Bogy D.B., and Talke F.E. (1987) 'Drop formation by dod ink-jet nozzles: A comparison of experiment and numerical simulation', *IBM Journal of Research and Development*, vol. 31(1), pp. 96–110.

[30] Wilson W.C. and Boland T. (2003) 'Cell and organ printing 1: Protein and cell printers', *The Anatomical Record Part A: Discoveries in Molecular, Cellular, and Evolutionary Biology*, vol. 272A(2), pp. 491–496.

[31] Tate T. (1864) 'On the magnitude of a drop of liquid formed under different circumstances', *The London, Edinburgh, and Dublin Philosophical Magazine and Journal of Science*, vol. 27(181), pp. 176–180.

[32] Lord Rayleigh (1899) 'XXXVI. Investigations in capillarity:-The size of drops.-The liberation of gas from supersaturated solutions.-Colliding jets.-The tension of contaminated water-surfaces', *The London, Edinburgh, and Dublin Philosophical Magazine and Journal of Science*, vol. 48(293), pp. 321–337.

[33] Wilson S.D.R. (1988) 'The slow dripping of a viscous fluid', *Journal of Fluid Mechanics*, vol. 190, pp. 561–570.

[34] Eggers J. and Dupont T.F. (1994) 'Drop formation in a one-dimensional approximation of the Navier-Stokes equation', *Journal of Fluid Mechanics*, vol. 262, pp. 205–221.

[35] Zhang X. and Basaran O.A. (1995) 'An experimental study of dynamics of drop formation', *Physics of Fluids*, vol. 7(6), pp. 1184–1203.

[36] Zhang D.F. and Stone H.A. (1997) 'Drop formation in viscous flows at a vertical capillary tube', *Physics of Fluids*, vol. 9(8), pp. 2234–2242.

[37] Ambravaneswaran B., Phillips S.D., and Basaran O.A. (2000) 'Theoretical analysis of a dripping faucet', *Physical Review Letters*, vol. 85, pp. 5332–5335.

[38] Chen A.U., Notz P.K., and Basaran O.A. (2002) 'Computational and experimental analysis of pinch-off and scaling', *Physical Review Letters*, vol. 88, p. 174501.

[39] Subramani H.J., Yeoh H.K., Suryo R., Xu Q., Ambravaneswaran B., and Basaran O.A. (2006) 'Simplicity and complexity in a dripping faucet', *Physics of Fluids*, vol. 18(3), p. 032106.

[40] Castrejón-Pita J.R., Castrejón-Pita A.A., Thete S.S., Sambath K., Hutchings I.M., Hinch J., Lister J.R., and Basaran O.A. (2015) 'Plethora of transitions

during breakup of liquid filaments', *Proceedings of the National Academy of Sciences*, vol. 112(15), pp. 4582–4587.

[41] Tomotika S. (1935) 'On the instability of a cylindrical thread of a viscous liquid surrounded by another viscous fluid', *Proceedings of the Royal Society of London A: Mathematical, Physical and Engineering Sciences*, vol. 150(870), pp. 322–337.

[42] Squire H.B. (1953) 'Investigation of the instability of a moving liquid film', *British Journal of Applied Physics*, vol. 4(6), p. 167.

[43] Sterling A.M. and Sleicher C.A. (1975) 'The instability of capillary jets', *Journal of Fluid Mechanics*, vol. 68(3), pp. 477–495.

[44] Goedde E.F. and Yuen M.C. (1970) 'Experiments on liquid jet instability', *Journal of Fluid Mechanics*, vol. 40(3), pp. 495–511.

[45] Richards J.R., Lenhoff A.M., and Beris A.N. (1994) 'Dynamic breakup of liquid-liquid jets', *Physics of Fluids*, vol. 6(8), pp. 2640–2655.

[46] Pan Y. and Suga K. (2006) 'A numerical study on the breakup process of laminar liquid jets into a gas', *Physics of Fluids*, vol. 18(5), p. 052101.

[47] Clanet C. and Lasheras J.C. (1999) 'Transition from dripping to jetting', *Journal of Fluid Mechanics*, vol. 383, pp. 307–326.

[48] Ambravaneswaran B., Subramani H.J., Phillips S.D., and Basaran O.A. (2004) 'Dripping-jetting transitions in a dripping faucet', *Physical Review Letters*, vol. 93, p. 034501.

[49] Utada A.S., Fernandez-Nieves A., Stone H.A., and Weitz D.A. (2007) 'Dripping to jetting transitions in coflowing liquid streams', *Physical Review Letters*, vol. 99, p. 094502.

[50] Chakraborty I., Rubio-Rubio M., Sevilla A., and Gordillo J. (2016) 'Numerical simulation of axisymmetric drop formation using a coupled level set and volume of fluid method', *International Journal of Multiphase Flow*, vol. 84, pp. 54 – 65.

[51] Borthakur M.P., Biswas G., and Bandyopadhyay D. (2017) 'Formation of liquid drops at an orifice and dynamics of pinch-off in liquid jets', *Physical Review E*, vol. 96, p. 013115.

[52] Wang A.B., Kuan C.C., and Tsai P.H. (2013) 'Do we understand the bubble formation by a single drop impacting upon liquid surface?', *Physics of Fluids*, vol. 25, p. 101702.

[53] Thoraval M.J., Li Y., and Thoroddsen S.T. (2016) 'Vortex-ring-induced large bubble entrainment during drop impact', *Physical Review E*, vol. 93, p. 033128.

[54] Taylor T.D. and Acrivos A. (1964) 'On the deformation and drag of a falling viscous drop at low Reynolds number', *Journal of Fluid Mechanics*, vol. 18(3), pp. 466–476.

[55] Kojima M., Hinch E.J., and Acrivos A. (1984) 'The formation and expansion of a toroidal drop moving in a viscous fluid', *The Physics of Fluids*, vol. 27(1), pp. 19–32.

[56] Koh C.J. and Leal L.G. (1989) 'The stability of drop shapes for translation at zero Reynolds number through a quiescent fluid', *Physics of Fluids A: Fluid Dynamics*, vol. 1(8), pp. 1309–1313.

[57] Gallino G., Zhu L., and Gallaire F. (2016) 'The stability of a rising droplet: an inertialess non-modal growth mechanism', *Journal of Fluid Mechanics*, vol. 786, p. R2.

[58] Koh C.J. and Leal L.G. (1990) 'An experimental investigation on the stability of viscous drops translating through a quiescent fluid', *Physics of Fluids A: Fluid Dynamics*, vol. 2(12), pp. 2103–2109.

[59] Becker E., Hiller W.J., and Kowalewski T. (1991) 'Experimental and theoretical investigation of large-amplitude oscillations of liquid droplets', *Journal of Fluid Mechanics*, vol. 231, pp. 189–210.

[60] Wellek R.M., Agrawal A.K., and Skelland A.H.P. (1966) 'Shape of liquid drops moving in liquid media', *AIChE Journal*, vol. 12, pp. 854–862.

[61] Loth E. (2008) 'Quasi-steady shape and drag of deformable bubbles and drops', *International Journal of Multiphase Flow*, vol. 34, pp. 523–546.

[62] Feng J.Q. and Beard K.V. (2011) 'Raindrop shape determined by computing steady axisymmetric solutions for Navier-Stokes equations', *Atmospheric Research*, vol. 101, pp. 480–491.

[63] Fakhari A. and Rahimian M.H. (2011) 'Investigation of deformation and breakup of a falling droplet using a multiple-relaxation-time lattice Boltzmann method', *Computers and Fluids*, vol. 40, pp. 156–171.

[64] Han J. and Tryggvason G. (1999) 'Secondary breakup of axisymmetric liquid drops. I. Acceleration by a constant body force', *Physics of Fluids*, vol. 11(12), pp. 3650–3667.

[65] Stone H.A. and Leal L.G. (1990) 'The effects of surfactants on drop deformation and breakup', *Journal of Fluid Mechanics*, vol. 220, pp. 161–186.

[66] Ramaswamy S. and Leal L. (1999) 'The deformation of a viscoelastic drop subjected to steady uniaxial extensional flow of a Newtonian fluid', *Journal of Non-Newtonian Fluid Mechanics*, vol. 85, pp. 127–163.

[67] Sostarecz M.C. and Belmonte A. (2003) 'Motion and shape of a viscoelastic drop falling through a viscous fluid', *Journal of Fluid Mechanics*, vol. 487, pp. 235–252.

[68] Wanchoo R., Sharma S.K., and Gupta R. (2003) 'Shape of a Newtonian liquid drop moving through an immiscible quiescent non-Newtonian liquid', *Chemical Engineering and Processing: Process Intensification*, vol. 42, pp. 387–393.

[69] Agrawal M., Premlata A.R., Tripathi M.K., Karri B., and Sahu K.C. (2017) 'Nonspherical liquid droplet falling in air', *Physical Review E*, vol. 95, p. 033111.

[70] Zou J., Ji C., Yuan B., Ren Y., Ruan X., and Fu X. (2012) 'Large bubble entrapment during drop impacts on a restricted liquid surface', *Physics of Fluids*, vol. 24(5), p. 057101.

[71] Michael D.H. (1981) 'Meniscus stability', *Annual Review of Fluid Mechanics*, vol. 13(1), pp. 189–216.

[72] Basaran O.A. (2002) 'Smallscale free surface flows with breakup: Drop formation and emerging applications', *AIChE Journal*, vol. 48(9), pp. 1842–1848.

[73] Tsai P.H. and Wang A.B. (Till date unpublished) 'Experiments on falling water drops', The experiments were carried out at the Institute of Applied Mechanics, National Taiwan University, Taipei 10617, Taiwan.

[74] Lord Rayleigh (1879) 'On the capillary phenomena of jets', *Proceedings of the Royal Society of London*, vol. 29, pp. 71–97.

[75] Pumphrey H.C. and Elmore P.A. (1990) 'The entrainment of bubbles by drop impacts', *Journal of Fluid Mechanics*, vol. 220, pp. 539–567.

[76] Oguz H.N. and Prosperetti A. (1990) 'Bubble entrainment by the impact of drops on liquid surfaces', *Journal of Fluid Mechanics*, vol. 219, pp. 143–179.

[77] Rein M. (1996) 'The transitional regime between coalescing and splashing drops', *Journal of Fluid Mechanics*, vol. 306, pp. 145–165.

[78] Leng L.J. (2001) 'Splash formation by spherical drops', *Journal of Fluid Mechanics*, vol. 427, pp. 73–105.

[79] Morton D., Rudman M., and Jong-Leng L. (2000) 'An investigation of the flow regimes resulting from splashing drops', *Physics of Fluids*, vol. 12, pp. 747–763.

[80] Zeff B.W., Kleber B., Fineberg J., and Lathrop D.P. (2000) 'Singularity dynamics in curvature collapse and jet eruption on a fluid surface', *Nature*, vol. 403, pp. 401–404.

[81] Bergmann R., van der Meer D., Stijnman M., Sandtke M., Prosperetti A., and Lohse D. (2006) 'Giant bubble pinch-off', *Physical Review Letters*, vol. 96, p. 154505.

[82] Gekle S., Gordillo J.M., van der Meer D., and Lohse D. (2009) 'High-speed jet formation after solid object impact', *Physical Review Letters*, vol. 102, p. 034502.

[83] Duchemin L., Popinet S., Josserand C., and Zaleski S. (2002) 'Jet formation in bubbles bursting at a free surface', *Physics of Fluids*, vol. 14(9), pp. 3000–3008.

[84] Deng Q., Anilkumar A.V., and Wang T.G. (2007) 'The role of viscosity and surface tension in bubble entrapment during drop impact onto a deep liquid pool', *Journal of Fluid Mechanics*, vol. 578, pp. 119–138.

[85] Chen S. and Guo L. (2014) 'Viscosity effect on regular bubble entrapment during drop impact into a deep pool', *Chemical Engineering Science*, vol. 109, pp. 1–16.

[86] Batchelor G., *An Introduction to Fluid Dynamics* (Cambridge University Press, Cambridge, UK, 1997).

[87] Thoraval M.J., Takehara K., Etoh T.G., Popinet S., Ray P., Josserand C., Zaleski S., and Thoroddsen S.T. (2012) 'von kármán vortex street within an impacting drop', *Physical Review Letters*, vol. 108, p. 264506.

[88] Castrejón-Pita A., Castrejón-Pita J., and Hutchings I. (2012) 'Experimental observation of von kármán vortices during drop impact', *Physical Review E*, vol. 86(4), p. 045301.

[89] Agbaglah G., Thoraval M.J., Thoroddsen S.T., Zhang L.V., Fezzaa K., and Deegan R.D. (2015) 'Drop impact into a deep pool: vortex shedding and jet formation', *Journal of Fluid Mechanics*, vol. 764, p. R1.

[90] Peck B. and Sigurdson L. (1994) 'The three-dimensional vortex structure of an impacting water drop', *Physics of Fluids*, vol. 6(2), pp. 564–576.

[91] Zhang L.V., Toole J., Fezzaa K., and Deegan R.D. (2012) 'Evolution of the ejecta sheet from the impact of a drop with a deep pool', *Journal of Fluid Mechanics*, vol. 690, pp. 5–15.

[92] Lee J.S., Park S.J., Lee J.H., , Weon B.M., Fezzaa K., and Je J.H. (2015) 'Origin and dynamics of vortex rings in drop splashing', *Nature Communications*, vol. 6, p. 8187.

[93] Chapman D.S. and Critchlow P.R. (1967) 'Formation of vortex rings from falling drops', *Journal of Fluid Mechanics*, vol. 29, pp. 177–185.

[94] Kutter V. (1916) 'Die anwendung on wirbelringen zur bestimmung von oberflächenspannungen', *Physikalische Zeitschrift*, vol. 23, pp. 573–579.

[95] Roudriguez F. and Mesler R. (1988) 'The penetration of drop-formed vortex rings into pools of liquid', *Journal of Colloid and Interface Science*, vol. 121, pp. 121–129.

[96] Shin J. and McMahon T.A. (1990) 'The tuning of a splash', *Physics of Fluids A: Fluid Dynamics*, vol. 2(8), pp. 1312–1317.

[97] Rein M. (1993) 'Phenomena of liquid drop impact on solid and liquid surfaces', *Fluid Dynamics Research*, vol. 12, pp. 61–93.

[98] Pumphrey H.C., Crum L.A., and Bjorno L. (1889) 'Underwater sound produced by individual drop impacts and rainfall', *The Journal of the Acoustical Society of America*, vol. 85, pp. 1518–1526.

[99] Kim H.Y., Park S.Y., and Min K. (2003) 'Imaging the high-speed impact of microdrop on solid surface', *Review of Scientific Instruments*, vol. 74(11), pp. 4930–4937.

[100] Visser C., Frommhold P., Wildeman S., Mettin R., Lohse D., and Sun C. (2015) 'Dynamics of high-speed micro-drop impact: numerical simulations and experiments at frame-to-frame times below 100 ns', *Soft Matter*, vol. 11, pp. 1708–1722.

[101] Chan C., Huang X., Frommhold P., Lippert A., and Ohl C.D. (2014) 'Water entry by a train of droplets', *67th Annual Meeting of APS Division of Fluid Dynamics (Gallery of Fluid Motion Video), November 23–November 25, 2014*, (V0096).

[102] Hurd R., Fanning T., Pan Z., Mabey C., Bodily K., Hacking K., Speirs N., and Truscott T. (2015) 'Matryoshka cavity', *Physics of Fluids*, vol. 27(9), p. 091104.

[103] Bouwhuis W., Huang X., Chan C.U., Frommhold P.E., Ohl C.D., Lohse D., Snoeijer J.H., and van der Meer D. (2016) 'Impact of a high-speed train of microdrops on a liquid pool', *Journal of Fluid Mechanics*, vol. 792, pp. 850–868.

[104] Bergmann R., Meer D.V.D., Gwkle S., Bos A.V.D., and Loshe D. (2009) 'Controlled impact of a disk on a water surface: cavity dynamics', *Journal of Fluid Mechanics*, vol. 633, pp. 381–409.

[105] Aristoff, J. M. and Bush, J. W. M. (2008) 'Water entry of small hydrophobic spheres', *Journal of Fluid Mechanics*, vol. 619, pp. 45–78.

[106] Thoroddsen S.T., Qian B., Etoh T.G., and Takehara K. (2007) 'The initial coalescence of miscible drops', *Physics of Fluids*, vol. 19(7), p. 072110.

[107] Ding H., Li E.Q., Zhang F.H., Sui Y., Spelt P.D.M., and Thoroddsen S.T. (2012) 'Propagation of capillary waves and ejection of small droplets in rapid droplet spreading', *Journal of Fluid Mechanics*, vol. 697, pp. 92–114.

[108] Ray B., Biswas G., and Sharma A. (2010) 'Generation of secondary droplets in coalescence of a drop at a liquidliquid interface', *Journal of Fluid Mechanics*, vol. 655, pp. 72–104.

[109] Kundu P.K. and Cohen I.M., *Fluid Mechanics* (Academic Press, 2008).

[110] Lee M., Longoria R.G., and Wilson D.E. (1997) 'Cavity dynamics in high-speed water entry', *Physics of Fluids*, vol. 9(3), pp. 540–550.

[111] Elmore P. A.and Chahine G.L. and Oguz H.N. (2001) 'Cavity and flow measurements of reproducible bubble entrainment following drop impacts', *Experiments in Fluids*, vol. 31(6), pp. 664–673.

[112] Zhu Y., Oguz H.N., and Prosperetti A. (2000) 'On the mechanism of air entrainment by liquid jets at a free surface', *Journal of Fluid Mechanics*, vol. 404, pp. 151–177.

[113] Oguz H.N., Prosperetti A., and Kolaini A.R. (1995) 'Air entrapment by a falling water mass', *Journal of Fluid Mechanics*, vol. 294, pp. 181–207.

[114] Burton J.C., Waldrep R., and Taborek P. (2005) 'Scaling and instabilities in bubble pinch-off', *Physical Review Letters*, vol. 94, p. 184502.

[115] Oguz H.N. and Prosperetti A. (1993) 'Dynamics of bubble growth and detachment from a needle', *Journal of Fluid Mechanics*, vol. 257, pp. 111–145.

[116] Thoroddsen S.T., Qian B., Etoh T.G., and Takehara K. (2007) 'The initial coalescence of miscible drops', *Physics of Fluids*, vol. 19(7), p. 072110.

[117] Leppinen D. and Lister J.R. (2003) 'Capillary pinch-off in inviscid fluids', *Physics of Fluids*, vol. 15(2), pp. 568–578.

[118] Day R.F., Hinch E.J., and Lister J.R. (1998) 'Self-similar capillary pinchoff of an inviscid fluid', *Physical Review Letters*, vol. 80, pp. 704–707.

[119] Gordillo J.M., Sevilla A., Rodríguez-Rodríguez J., and Martínez-Bazán C. (2005) 'Axisymmetric bubble pinch-off at high reynolds numbers', *Physical Review Letters*, vol. 95, p. 194501.

[120] Hogrefe J.E., Peffley N.L., Goodridge C.L., Shi W.T., Hentschel H.G.E., and Lathrop D.P. (1998) 'Power-law singularities in gravity-capillary waves', *Physica D: Nonlinear Phenomena*, vol. 123(1), pp. 183 – 205.

[121] Bick A.G., Ristenpart W.D., van Nierop E.A., and Stone H.A. (2010) 'Bubble formation via multidrop impacts', *Physics of Fluids*, vol. 22, p. 042105.

[122] Charles G.E. and Mason S.G. (1960) 'The coalescence of liquid drop with flat liquid-liquid interfaces', *Journal of Colloid Science*, vol. 15, pp. 236–267.

[123] Charles G.E. and Mason S.G. (1960) 'The mechanism of partial coalescences of liquid drop at liquid-liquid interfaces', *Journal of Colloid Science*, vol. 15, pp. 105–122.

[124] Schotland R.M. (1960) 'Experimental results relating to the coalescence of water drops with water surfaces', *Discussions of the Faraday Socity*, vol. 30, pp. 72–77.

[125] Thoroddsen S.T. and Takehara K. (2000) 'The coalescence cascade of a drop', *Physics of Fluids*, vol. 12, pp. 1265–1267.

[126] Chen X., Mandre S., and Feng J.J. (2006) 'An experimental study of the coalescence between a drop and an interface in newtonian and polymeric liquids', *Physics of Fluids*, vol. 18, p. 092103.

[127] Fedorchenko A.I. and Wang A.B. (2004) 'On some common features of drop impact on liquid surfaces', *Physics of Fluids*, vol. 16(5), pp. 1349–1365.

[128] Pan K.L. and Law C.K. (2007) 'Dynamics of droplet-film collision', *Journal of Fluid Mechanics*, vol. 587, pp. 1–22.

[129] Tang X., Saha A., Law C.K., and Sun C. (2016) 'Nonmonotonic response of drop impacting on liquid film: mechanism and scaling', *Soft Matter*, vol. 12, pp. 4521–4529.

[130] Tang X., Saha A., Law C.K., and Sun C. (2018) 'Bouncing-to-merging transition in drop impact on liquid film: Role of liquid viscosity', *Langmuir*, vol. 34(8), pp. 2654–2662.

[131] Berry E.X. and Reinhardt R.L. (1974) 'An analysis of cloud drop growth by collection: Part III. Accretion and Self-collection', *Journal of the Atmospheric Sciences*, vol. 31(8), pp. 2118–2126.

[132] Raes F., Dingenen R.V., Vignati E., Wilson J., Putaud J.P., Seinfeld J.H., and Adams P. (2000) 'Formation and cycling of aerosols in the global troposphere', *Atmospheric Environment*, vol. 34(25), pp. 4215–4240.

[133] Bhakta A. and Ruckenstein E. (1997) 'Decay of standing foams: drainage, coalescence and collapse', *Advances in Colloid and Interface Science*, vol. 70, pp. 1 – 124.

[134] Thomson J.J. and Newall H.F. (1885) 'On formation of vortex rings by drops falling into liquids, and some allied phenomena', *Proceedings of the Royal Society of London*, vol. 39, pp. 417–436.

[135] Sarpkaya T. (1996) 'Vorticity, free surface, and surfactants', *Annual Review of Fluid Mechanics*, vol. 28(1), pp. 83–128.

[136] Lord Rayleigh (1878) 'On the instability of jets', *Proceedings of the London Mathematical Society*, vol. s1-10(1), pp. 4–13.

[137] Pikhitsa P. and Tsargorodskaya A. (2000) 'Possible mechanism for multistage coalescence of a floating droplet on the air/liquid interface', *Colloids and Surfaces A: Physicochemical and Engineering Aspects*, vol. 167(3), pp. 287 – 291.

[138] Honey E.M. and Kavehpour H.P. (2006) 'Astonishing life of a coalescing drop on a free surface', *Physical Review E*, vol. 73, p. 027301.

[139] Chen X., Mandre S., and Feng J.J. (2006) 'Partial coalescence between a drop and a liquid-liquid interface', *Physics of Fluids*, vol. 18, p. 051705.

[140] Blanchette F. and Bigioni T.P. (2006) 'Partial coalescence of drops at liquid interfaces', *Nature Physics*, vol. 2(5), pp. 254–257.

[141] Kavehpour H.P. (2015) 'Coalescence of drops', *Annual Review of Fluid Mechanics*, vol. 47(1), pp. 245–268.

[142] Jiang Y.J., Umemura A., and Law C.K. (1992) 'An experimental investigation on the collision behaviour of hydrocarbon droplets', *Journal of Fluid Mechanics*, vol. 234, pp. 171–190.

[143] Qian J. and Law C.K. (1997) 'Regimes of coalescence and separation in droplet collision', *Journal of Fluid Mechanics*, vol. 331, pp. 59–80.

[144] Leal L.G. (2004) 'Flow induced coalescence of drops in a viscous fluid', *Physics of Fluids*, vol. 16(6), pp. 1833–1851.

[145] Tang C., Zhang P., and Law C.K. (2012) 'Bouncing, coalescence, and separation in head-on collision of unequal-size droplets', *Physics of Fluids*, vol. 24(2), p. 022101.

[146] Mackay G.D.M. and Mason S.G. (1963) 'The gravity approach and coalescence of fluid drops at liquid interfaces', *The Canadian Journal of Chemical Engineering*, vol. 41(5), pp. 203–212.

[147] Yang H., Park C.C., Hu Y.T., and Leal L.G. (2001) 'The coalescence of two equal-sized drops in a two-dimensional linear flow', *Physics of Fluids*, vol. 13(5), pp. 1087–1106.

[148] Baldessari F., Homsy G., and Leal L.G. (2007) 'Linear stability of a draining film squeezed between two approaching droplets', *Journal of Colloid and Interface Science*, vol. 307(1), pp. 188–202.

[149] Yoon Y., Baldessari F., Ceniceros H.D., and Leal L.G. (2007) 'Coalescence of two equal-sized deformable drops in an axisymmetric flow', *Physics of Fluids*, vol. 19(10), p. 102102.

[150] Hsu A.S., Roy A., and Leal L.G. (2008) 'Drop-size effects on coalescence of two equal-sized drops in a head-on collision', *Journal of Rheology*, vol. 52(6), pp. 1291–1310.

[151] Ramachandran A. and Leal L.G. (2016) 'Effect of interfacial slip on the thin film drainage time for two equal-sized, surfactant-free drops undergoing a head-on collision: A scaling analysis', *Physical Review Fluids*, vol. 1, p. 064204.

[152] Anilkumar A.V., Lee C.P., and Wang T.G. (1991) 'Surface-tension-induced mixing following coalescence of initially stationary drops', *Physics of Fluids A: Fluid Dynamics*, vol. 3(11), pp. 2587–2591.

[153] Eggers J., Lister J.R., and Stone H.A. (1999) 'Coalescence of liquid drops', *Journal of Fluid Mechanics*, vol. 401, pp. 293–310.

[154] Duchemin L., Eggers J., and Josserand C. (2003) 'Inviscid coalescence of drops', *Journal of Fluid Mechanics*, vol. 487, pp. 167–178.

[155] Liu D., Zhang P., Law C.K., and Guo Y. (2013) 'Collision dynamics and mixing of unequal-size droplets', *International Journal of Heat and Mass Transfer*, vol. 57(1), pp. 421–428.

[156] Burton J.C. and Taborek P. (2007) 'Role of dimensionality and axisymmetry in fluid pinch-off and coalescence', *Physical Review Letters*, vol. 98, p. 224502.

[157] Paulsen J.D., Burton J.C., and Nagel S.R. (2011) 'Viscous to inertial crossover in liquid drop coalescence', *Physical Review Letters*, vol. 106, p. 114501.

[158] Aarts D.G.A.L., Lekkerkerker H.N.W., Guo H., Wegdam G.H., and Bonn D. (2005) 'Hydrodynamics of droplet coalescence', *Physical Review Letters*, vol. 95, p. 164503.

[159] Thoroddsen S.T., Takehara K., and Etoh T.G. (2005) 'The coalescence speed of a pendent and a sessile drop', *Journal of Fluid Mechanics*, vol. 527, pp. 85–114.

[160] Wu M., Cubaud T., and Ho C.M. (2004) 'Scaling law in liquid drop coalescence driven by surface tension', *Physics of Fluids*, vol. 16(7), pp. L51–L54.

[161] Menchaca-Rocha A., Martínez-Dávalos A., Núñez R., Popinet S., and Zaleski S. (2001) 'Coalescence of liquid drops by surface tension', *Physical Review E*, vol. 63, p. 046309.

[162] Paulsen J.D., Carmigniani R., Kannan A., Burton J.D., and Nagel S.R. (2014) 'Coalescence of bubbles and drops in an outer fluid', *Nature Communications*, vol. 5, p. 3182.

[163] Blanchette F. and Bigioni T.P. (2009) 'Dynamics of drop coalescence at fluid interfaces', *Journal of Fluid Mechanics*, vol. 620, pp. 333–352.

[164] Zhang F.H., Li E.Q., and Thoroddsen S.T. (2009) 'Satellite formation during coalescence of unequal size drops', *Physical Review Letters*, vol. 102, p. 104502.

[165] Gilet T., Mulleners K., Lecomte J.P., Vandewalle N., and Dorbolo S. (2007) 'Critical parameters for the partial coalescence of a droplet', *Physical Review E*, vol. 75, p. 036303.

[166] Keller J.B. and Miksis M.J. (1983) 'Surface tension driven flows', *SIAM Journal on Applied Mathematics*, vol. 43(2), pp. 268–277.

[167] Keller J.B., Milewski P.A., and Vanden-Broeck J.M. (2000) 'Merging and wetting driven by surface tension', *European Journal of Mechanics - B/Fluids*, vol. 19(4), pp. 491 – 502.

[168] Zhang F.H. and Thoroddsen S.T. (2008) 'Satellite generation during bubble coalescence', *Physics of Fluids*, vol. 20(2), p. 022104.

[169] Zhang F.H., Thoraval M.J., Thoroddsen S.T., and Taborek P. (2015) 'Partial coalescence from bubbles to drops', *Journal of Fluid Mechanics*, vol. 782, pp. 209–239.

[170] Dong T., Weheliye W.H., Chausset P., and Angeli P. (2017) 'An experimental study on the drop/interface partial coalescence with surfactants', *Physics of Fluids*, vol. 29(10), p. 102101.

Appendix

Axisymmetric form of the governing equations in cylindrical coordinate (r, z) for incompressible fluid are given below. Here, r and z represent the radial and axial coordinates having velocity components u and v along the respective directions.

Continuity equation:

$$\rho(\phi)\left[\frac{1}{r}\frac{\partial(ru)}{\partial r}+\frac{\partial v}{\partial z}\right]=0 \tag{A.1}$$

Momentum equations in r and z direction:

$$\begin{aligned}\rho(\phi)\left(\frac{\partial u}{\partial t}+u\frac{\partial u}{\partial r}+v\frac{\partial u}{\partial z}\right)&=-\frac{\partial p}{\partial r}+\frac{\partial}{\partial r}\left(2\mu(\phi)\frac{\partial u}{\partial r}\right)\\&+\frac{\partial}{\partial z}\left(\mu(\phi)\left(\frac{\partial u}{\partial z}+\frac{\partial v}{\partial r}\right)\right)+\frac{2\mu(\phi)}{r}\left(\frac{\partial u}{\partial r}-\frac{u}{r}\right)+f_{sv}\end{aligned} \tag{A.2}$$

$$\begin{aligned}\rho(\phi)\left(\frac{\partial v}{\partial t}+u\frac{\partial v}{\partial r}+v\frac{\partial v}{\partial z}\right)&=-\frac{\partial p}{\partial z}+\rho(\phi)g+\frac{\partial}{\partial z}\left(2\mu(\phi)\frac{\partial v}{\partial z}\right)\\&+\frac{\partial}{\partial z}\left(\mu(\phi)\left(\frac{\partial v}{\partial r}+\frac{\partial u}{\partial z}\right)\right)+\frac{\mu(\phi)}{r}\left(\frac{\partial v}{\partial r}+\frac{\partial u}{\partial z}\right)+f_{sv}\end{aligned} \tag{A.3}$$

Here, f_{sv} is the surface tension force.

Volume fraction advection equation:

$$\frac{\partial F}{\partial t}+\frac{1}{r}\frac{\partial(rFu)}{\partial r}+\frac{\partial(Fv)}{\partial z}=0 \tag{A.4}$$

Level set advection equation:

$$\frac{\partial \phi}{\partial t}+\frac{1}{r}\frac{\partial(r\phi u)}{\partial r}+\frac{\partial(\phi v)}{\partial z}=0 \tag{A.5}$$

List of publications

Journals

1. **Deka H.**, Ray B., Biswas G., Dalal A., Tsai P.-H., and Wang A.-B. (2017) 'The regime of large bubble entrapment during a single drop impact on a liquid pool', *Physics of Fluids*, vol. 29(9), pp.092101(1-13).

   (Online available : https://doi.org/10.1063/1.4992124)

2. **Deka H.**, Ray B., Biswas G., and Dalal A. (2018) 'Dynamics of tongue shaped cavity generated during the impact of high-speed microdrops', *Physics of Fluids*, vol. 30(4), pp. 042103(1-14).

   (Online available : https://doi.org/10.1063/1.5022374)

3. **Deka H.**, Tsai P.-H., Biswas G., Dalal A., Ray B., and Wang A.-B. (2018) 'Dynamics of formation and oscillation of non-spherical drops', *Physical Review E* (Under Review).

4. **Deka H.**, Biswas G., Chakraborty S., and Dalal A. (2018) 'Coalescence dynamics of unequal sized drops', *Journal of Fluid Mechanics* (Under Review).

Conferences

1. **Deka H.**, Biswas G., and Dalal A. (2016) 'Formation and penetration of vortex ring on drop coalescence', *ASME International Mechanical Engineering Congress and Exposition, November 11–November 17, 2016, Phoenix, AZ, USA*, Paper No. IMECE2016-66786.

2. **Deka H.**, Biswas G., and Dalal A. (2017) 'Partial coalescence of unequal sized drops', *5th International Conference on Complex Dynamical Systems and Applications, December 4–December 6, 2017, IIT Guwahati, India* (Oral Presentation).